

Investigation of the electronic band structure of 2D transition metal dichalcogenides via angle-resolved photoemission spectroscopy

Bharti Parashar

Schlüsseltechnologien / Key Technologies

Band / Volume 275

ISBN 978-3-95806-725-7

Forschungszentrum Jülich GmbH
Peter Grünberg Institut (PGI)
Elektronische Eigenschaften (PGI-6)

Investigation of the electronic band structure of 2D transition metal dichalcogenides via angle-resolved photoemission spectroscopy

Bharti Parashar

Schriften des Forschungszentrums Jülich
Reihe Schlüsseltechnologien / Key Technologies

Band / Volume 275

ISSN 1866-1807

ISBN 978-3-95806-725-7

Bibliografische Information der Deutschen Nationalbibliothek.
Die Deutsche Nationalbibliothek verzeichnet diese Publikation in der
Deutschen Nationalbibliografie; detaillierte Bibliografische Daten
sind im Internet über <http://dnb.d-nb.de> abrufbar.

Herausgeber und Vertrieb: Forschungszentrum Jülich GmbH
Zentralbibliothek, Verlag
52425 Jülich
Tel.: +49 2461 61-5368
Fax: +49 2461 61-6103
zb-publikation@fz-juelich.de
www.fz-juelich.de/zb

Umschlaggestaltung: Grafische Medien, Forschungszentrum Jülich GmbH

Druck: Grafische Medien, Forschungszentrum Jülich GmbH

Copyright: Forschungszentrum Jülich 2023

Schriften des Forschungszentrums Jülich
Reihe Schlüsseltechnologien / Key Technologies, Band / Volume 275

D 464 (Diss. Duisburg, Univ., 2023)

ISSN 1866-1807
ISBN 978-3-95806-725-7

Vollständig frei verfügbar über das Publikationsportal des Forschungszentrums Jülich (JuSER)
unter www.fz-juelich.de/zb/openaccess.



This is an Open Access publication distributed under the terms of the [Creative Commons Attribution License 4.0](https://creativecommons.org/licenses/by/4.0/), which permits unrestricted use, distribution, and reproduction in any medium, provided the original work is properly cited.

Zusammenfassung

Zweidimensionale (2D) Übergangsmetall-Dichalcogenide (TMDCs) sind eine Klasse von geschichteten Van-der-Waals-Halbleitern, die bemerkenswerte Eigenschaften aufweisen. Darunter fallen zum Beispiel eine optische Bandlücke, eine hohe Ladungsträgerbeweglichkeit, sowie abstimmbare elektronische Eigenschaften. Diese Eigenschaften, insbesondere in TMDC-Heterostrukturen, machen sie attraktiv für künftige optoelektronische Technologien wie Tunnelioden, Tunneltransistoren, Leuchtdioden und photovoltaische Zellen. TMDC-Bauelemente auf der Grundlage von Homo- oder Heterostrukturen können aus mehrschichtigen Stapeln bestehen, wobei jede Schicht eine andere elementare Zusammensetzung aufweist. Dies führt zu Bauelementen mit unterschiedlichen Eigenschaften, welche auf die spezifische Anwendung abgestimmt werden können. Angesichts des zunehmenden Interesses an diesem Bereich und der Möglichkeit, TMDC-Bauelemente mit verschiedenen Eigenschaften und Zusammensetzungen herzustellen, besteht ein enormes Forschungspotenzial, welches interessante Phänomene hervorbringen könnte. In diesem Sinne zielt diese Arbeit darauf ab, die elektronische Bandstruktur von WSe_2 , einem wichtigen TMDC-Halbleiter, mit Hilfe einer Kombination aus winkelaufgelöster Photoemissionsspektroskopie (ARPES) und Dichtefunktionaltheorie (DFT) zu untersuchen und ein umfassendes Verständnis für diese zu entwickeln.

Die Untersuchungen in dieser Arbeit erfolgten mit Hilfe von Mikro-ARPES (μ -ARPES), welches eine Strahlgröße im Mikrometerbereich nutzt, um Mikrostrukturen zu untersuchen. Diese Mikrostrukturen beinhalten Bereiche von einschichtigem (SL) und zweischichtigem (BL) WSe_2 auf Graphitsubstraten mit unterschiedlichen Verdrehungswinkeln zwischen dem SL WSe_2 und Graphit sowie BL WSe_2 . In den verdrillten SL WSe_2 /Graphit-Strukturen werden die von den Graphit π -Bändern emittierten Elektronen in die SL WSe_2 gestreut, was zum Auftreten von Mehrfachkopien führt, die die trigonale Symmetrie einer SL WSe_2 widerspiegeln. Wir haben zwei verdrillte BL WSe_2 mit Verdrillungswinkeln von $\sim 28^\circ$ und $\sim 10^\circ$ untersucht und konnten keine Anzeichen für Hybridisierungslücken an den Kreuzungspunkten der Zwischenschichtbänder finden, die Vorläufer der flachen Energiebänder bei kleineren Verdrillungswinkeln sein könnten. Auch für SL WSe_2 /Graphit wurden keine solchen Lücken gefunden. In beiden Fällen befindet sich das globale Valenzband-Maximum (VBM) am K_{WSe_2} -Punkt der Brillouin-Zone (BZ). Wir präsentieren auch die ARPES-Studien für den parallelen Impuls k_{\parallel} jenseits der ersten BZ. Unsere Ergebnisse zeigen die Visualisierung der charakteristischen Merkmale der einzelnen WSe_2 -Schichten separat in den Homo-Zweischicht-Strukturen, die wir weiter nutzen, um den Verdrehungswinkel zwischen diesen SLs abzuschätzen. Theoretische Dichtefunktionaltheorieberechnungen unterstützen die experimentellen Ergebnisse und zeigen, dass die Bildung von Hybridisierungslücken in WSe_2 /Graphen, einem System, das dem experimentellen WSe_2 /Graphit-System sehr ähnlich ist, besonders vom WSe_2 -Bandcharakter am Graphen-Dirac-Punkt abhängt. Zusätzlich zeigen wir Zirkulardichroismus mit Hilfe von winkelaufgelöster Photoemissionsspektroskopie (CD-ARPES) einer WSe_2 Volumenprobe, verdrilltem SL WSe_2 /Graphit und BL WSe_2 /Graphit Strukturen mit verschiedenen Verdrillungswinkeln. Unsere Ergebnisse zeigen signifikante CD-Signale im K -Tal sowohl in der Bulkprobe WSe_2 als auch in verdrilltem SL WSe_2 /Graphit, während in verdrilltem BL WSe_2 die integrierte CD-ARPES im K -Tal zusätzlich zur dichroitischen Signalasymmetrie bei Γ noch sichtbar ist. Die integrierten CD-ARPES in den K - und Γ -Tälern in allen drei Probenstrukturen lassen sich auf den Bahndrehimpuls (OAM) bzw. geometriebedingte Effekte zurückführen. Das dichroitische SL-Signal wird durch die theoretischen Einstufen-Modellsimulationen gut beschrieben. Erste Tests zur Simulation dichroitischer Signale aus verdrehten Doppelschichten durch eine inkommensurate Summe separater SLs sind vielversprechend.

Durch die Vertiefung der elektronischen Bandstruktur von TMDC mittels μ -ARPES, DFT und CD-ARPES entschlüsselt unsere Studie die komplizierten Eigenschaften von WSe_2 , was unser Verständnis von TMDC-Halbleitern verbessert und innovative Anwendungen in Tunnelbauelementen, Transistoren, LEDs und Photovoltaik fördert.

Abstract

Two-dimensional (2D) transition metal dichalcogenides (TMDCs) are a class of layered van der Waals (vdW) semiconductors that exhibit remarkable properties, including an optical bandgap, high carrier mobility, and tunable electronic properties. These properties, particularly in TMDC heterostructures, make them attractive for future optoelectronic technologies such as tunneling diodes, tunneling transistors, light-emitting diodes, and photovoltaic cells. TMDC devices based on homo- or heterostructures may consist of multi-layered stacks, each layer with a different elemental composition, resulting in devices with diverse properties. With increasing interest in this field and the potential to fabricate TMDC-based devices with multiple configurations, there is enormous potential for exploration, which could uncover interesting phenomena. In this direction, this thesis aims to investigate and provide a thorough understanding of the electronic band structure of WSe₂, an important TMDC semiconductor, using a combination of angle-resolved photoemission spectroscopy (ARPES) and density functional theory (DFT) techniques.

In this work, we employed ARPES with a micrometer focused beam spot size, commonly known as micro-ARPES (μ -ARPES), to investigate microstructures containing areas of single-layer (SL) and bilayer (BL) WSe₂ on graphite substrates at different twist angles between the SL WSe₂ and graphite and within the BL WSe₂. In the twisted SL WSe₂/graphite structures the electrons emitted from the graphite π bands scatter in the SL WSe₂ leading to the appearance of multiple copies, which reflect the trigonal symmetry of a SL WSe₂. We investigated two twisted BL WSe₂ at twist angles of $\sim 28^\circ$ and $\sim 10^\circ$ and found no evidence of hybridization gaps at the inter-layer band crossing points, that could be precursors of the flat bands at smaller twist angles. Similarly, no such gaps were found for SL WSe₂/graphite. For both cases, the global valence band maximum (VBM) is at the K_{WSe_2} point of the Brillouin zone (BZ). We also present the ARPES studies for the parallel momentum k_{\parallel} beyond the first BZ. Our findings demonstrate the visualization of characteristic features of the individual WSe₂ layers separately in the homo-bilayer structures, which we further use to estimate the twist angle between these SLs. Theoretical density functional theory calculations support the experimental findings by indicating that the formation of hybridization gaps in WSe₂/graphene, a system that closely resembles the experimental WSe₂/graphite system, is sensitively dependent on the WSe₂ band character at the graphene Dirac band crossing point.

Additionally, we present the circular dichroism in an angle-resolved photoemission spectroscopy (CD-ARPES) study of WSe₂ bulk, twisted SL WSe₂/graphite and BL WSe₂/graphite structures with different twist angles. Our results show significant CD signals at the K valley in both bulk WSe₂ and twisted SL WSe₂/graphite, while in twisted BL WSe₂, the K valley integrated CD-ARPES is still visible in addition to the dichroic signal asymmetry at Γ . The integrated CD-ARPES at K and Γ valleys in all three sample structures can be attributed to orbital angular momentum (OAM) and geometry-induced effects, respectively. The SL dichroic signal is well described by theoretical one-step model simulations. Initial tests to simulate dichroic signals from twisted bilayers by an incommensurate sum of separate SLs are promising.

By delving deeper into TMDC electronic band structure via μ -ARPES, DFT and CD-ARPES, our study unravels the intricate characteristics of WSe₂, advancing our understanding of TMDC semiconductors and fostering innovative applications in tunneling devices, transistors, LEDs and photovoltaics.

Contents

Zusammenfassung	iii
Abstract	v
1 Introduction	1
2 Background and Literature Review	5
2.1 Electrons in solids	5
2.2 Photoemission spectroscopy	7
2.2.1 Photoemission process	8
2.2.2 Angle-resolved photoemission process	11
2.3 The three-step model	13
2.4 Spin-orbit coupling in solids	18
2.5 Density functional theory	20
2.5.1 The Kohn-Sham equations	21
2.5.2 Approximation for the exchange-correlation energy functional	22
2.6 An introduction to layered materials	25
2.7 Transition metal dichalcogenides	26
2.8 Atomically thin materials/ 2D TMDC	28
2.8.1 Crystal structure of a 2D monolayer	28
2.9 An introduction to vdW hetero-structures	29
2.10 Electronic bandstructure of 2D materials	32
3 Sample Preparation and Characterization	37
3.1 Sample fabrication methods	37
3.1.1 Mechanical exfoliation	37
3.1.2 Dry transfer technique	39
3.2 Fabrication of 2D hetero-structures	41
3.3 Strain induced bubbles	43
4 Experimental Setup	47
4.1 Nano-ARPES beamlines	47
4.2 ANTARES beamline at SOLEIL	50
4.3 MAESTRO beamline at ALS	54
4.4 NanoESCA beamline at Elettra	57
5 The Electronic Bandstructure of Twisted Monolayers and Bilayers of WSe_2	61
5.1 μ -ARPES experiments at NanoESCA beamline	63
5.1.1 h-BN as a substrate	63
5.1.2 SiO_2 as a substrate	64
5.2 μ -ARPES experiments at MAESTRO and ANTARES beamlines	67
5.2.1 Identification of SL and BL micro-regions	68
5.2.2 Photon energy dependence	71
5.2.3 ARPES 3D data sets	74
5.2.4 Copies of graphite K -point Dirac cones	77
5.2.5 Visualization of the SL features in twisted BL WSe_2	82

5.2.6	Orbital character and VBM estimation	85
5.2.7	Theoretical calculations	89
5.3	Conclusion	95
6	Circular Dichroism in the Bandstructure of Twisted SL, BL, and Bulk WSe₂	97
6.1	Circular dichroism in the angular distribution of photoelectrons	97
6.2	Circular dichroism in WSe ₂	99
6.2.1	Bulk-WSe ₂	101
6.2.2	Twisted SL and BL WSe ₂	105
6.2.3	Conclusions	112
7	Summary and Outlook	113
	List of Abbreviations	117
	Bibliography	119
	Publications and conference contributions	151
	Curriculum vitae	153
	Acknowledgments	155

List of Figures

2.1	Electronic band structure of electrons in a periodic potential. Left panel represents periodic zone scheme of the band structure in a solid, with the dashed line representing the region of the first BZ while right panel shows the the opening of gaps at the BZ edge and in the center due to the lattice potential.	6
2.2	Panel (a) shows the schematic of a typical ARPES experiment. Panel (b) depicts the energy diagram for the photoemission process where an electron (orange sphere) in a solid is excited by photon energy ($h\nu$). The kinetic energy (E_k) of the electron is given as a function of the excitation energy ($h\nu$), binding energy (E_B), and the work function of the material (ϕ). Panel (c) illustrates the initial and final momentum vector inside and outside the solid with the parallel components conserved while the perpendicular component is not conserved. Reproduced from.	13
2.3	Plot depicting the universal curve of inelastic mean free path of photoelectrons as a function of their kinetic energy inside the material. A solid line represents the empirically calculated universal curve and experimental data points of the IMFP of diverse materials. The mean free path for the relevant energy is about few Å.	15
2.4	Panel (a) shows an electron moving around a nucleus as observed from the nucleus's reference frame. Panel (b) illustrates, in the reference frame of the electron, that the nucleus seems to be revolving about it. As a result, an upward-directed magnetic field is experienced by the electron.	18
2.5	Total number of W atoms in Moiré superlattice for (a) twisted WSe ₂ bilayers and (b) WSe ₂ on graphene as a function of twist angle θ (in $^\circ$). The lattice structure of twisted bilayer system is not periodic in general as a function of twist angles as the periods of top and bottom layers are generally incommensurate with each layer. Hence, we restrict some special angles that two periods to be coincide resulting in a finite unit cell after rotation.	23
2.6	Crystal structure of 2H-WSe ₂ . Panel (a) shows the two monolayers of WSe ₂ including the primitive unit cells. Panels (b & c) demonstrate side and top view of 2H-crystal symmetry showing out-of-plane and in-plane lattice constants. W atoms are depicted in green, while Se atoms are depicted in yellow.	26
2.7	Crystal structure of TMDCs (WSe ₂) monolayer. Panel (a) shows transition metal M atom (W) is trigonally prismatic coordinated with X atoms (Se). Panel (b,c) show the side and top views of crystal structure demonstrating the hexagonal structure with metal (green) and chalcogen (yellow) atoms. The gray shaded region is the primitive unit cell constructed using the two primitive lattice vectors a_1 , a_2 of magnitude a , which correspond to the lattice constant.	27

2.8	Comparison of graphene and monolayer WSe ₂ like lattices and Brillouin zones. In (a) all 6 K -points are equivalent due to the presence of the inversion symmetry, represented by green-colored C-atoms. Within the BZ, the ΓM and $\Gamma K'$ lines (depicted by dashed black lines) act as mirror planes. In (b) WSe ₂ lattice has a two-atom basis, with green and yellow balls representing the atoms. In the BZ, the mirror symmetry along $\Gamma K'$ (dashed gray line) is broken and the SOC divides the BZ corners into non equivalent K/K' points allowing for spin-polarized bands.	28
2.9	Panel (a) shows schematic illustration of the vertical vdW hetero-structures. Different types of atomic layers are stacked on the top of each other. Panel (b) shows that one atomic lattice is rotated with angle θ with respect to the other.	30
2.10	Schematic depiction of the fabrication of the lateral and vertical hetero-structures. Panel (a) shows the first TMDC layer on the substrate. Panel (b) represents the assembly of the second TMDCs layer with the first one. Panel (c) and Panel (d) represent lateral- and vertical- vdW hetero-structures, respectively.	30
2.11	DFT calculated electronic band structures of MoS ₂ in (a) bulk, (b) bilayer and (c) monolayer form at high symmetry points. The direct and indirect band gaps are indicated by the black arrows in each figure. The valence band maximum (VBM) is set to 0 eV. (d) Sketch of the band structure of 2H-MoS ₂ , showing the spin-orbit splitting of the valence bands edges at the K and K' points at the corners of the Brillouin zone. Blue and black cones represent spin-up and spin-down, while red and blue arrow indicate valley optical selection rules respectively. Adapted from	32
3.1	Schematics of micromechanical exfoliation of a layered material: (a) Adhesive tape is pressed onto the specified crystal. (b) Peel off the sticky tape, allowing the top layers of the crystal to adhere to the tape. (c) The tape was then placed onto the desired substrate, such as Si, TiO ₂ , and so on. (d) Keep on repeating the same process in order to get the single layers of the layered materials. Reproduced from	36
3.2	(a) and (b) show the optical micrographs of the mechanically exfoliated WSe ₂ flakes surrounded by thicker bulky flakes. Different thickness of the flakes is shown by the varying optical contrast.	37
3.3	Deterministic dry transfer setup and process: (a)The experimental setup for the all-dry transfer technique is depicted schematically. The procedure involved in the preparation of the visco-elastic stamp and the deterministic transfer of an atomically thin flake to a user-defined location are depicted in (b-g). Reproduced from	38
3.4	Sequential transfer of homo-bilayer of WSe ₂ flakes: (a) Optical image of a mechanically exfoliated graphite flake on an n-Si substrate. (b) Optical image of the same flake following the transfer of a single layer of WSe ₂ flake that is referred to as the bottom layer. (c) Another single layer of WSe ₂ is transferred onto the stack by employing another transfer step. The top and bottom monolayers of WSe ₂ are shown by the red and green dotted lines. (d) Optical image of the twisted SL and BL WSe ₂ /graphite/n-Si. This structure exhibits two type of twist angles: between the graphite and SL WSe ₂ and between the top and bottom SLs of WSe ₂ , which are represented by the yellow and gray dashed circles, respectively. (e) Schematic model of the sample configuration. Different nanosheets are denoted by green, red, and black colors.	40

3.5	2D TMDCs flake on different substrates: AFM images of WSe ₂ monolayer on silicon (a), and graphite (b) substrate. The contamination aggregates in form of bubbles due to self-cleaning effect between graphite and TMDCs interface. Bubbles and cracks are depicted by white and yellow arrows.	41
3.6	Bubbles trapped between 2D TMDCs (WSe ₂) flake and graphite: (a) Optical micrograph of the SL WSe ₂ and BL WSe ₂ flake lying on the thick graphite flake (fig. 3.4). (b,c) show the AFM image and height profile measured on the edge of the monolayer flake of WSe ₂ /graphite as indicated by black square in (a). The AFM images measured at the SL WSe ₂ and BL WSe ₂ parts of the sample structure are shown in (d,g). (e,h) are AFM images of the bubbles created by WSe ₂ flake, which are shown by black squares in (d,g), and (f,i) show the bubble's cross sectional profile. Black line in (e,h) indicates where the profiles in (f,i) were measured.	42
4.1	Schematic depiction of the ANTARES beamline. The first pre-focusing mirrors collimate the undulator beam to a plane-grating monochromator with two gratings that can be exchanged by remote control. The PGM is positioned to suppress higher orders of light with high resolving power. The second set of mirrors is used to refocus the beam on the sample or the pinhole, depending on whether a micro- or nanometer spot size is required. Reprinted with permission from J. Avila, from	48
4.2	Illustration of the experimental geometry of the ARPES setup at the ANTARES beamline. The angular distribution along the horizontal entrance slit is imaged by the analyzer. 2D k-space mapping is achieved by rotating the sample around the vertical manipulator axis. The incidence direction of the X-ray radiation is indicated by green color.	49
4.3	Fresnel zone plate	51
4.4	Schematic depiction of the MAESTRO beamline at ALS. It consists of various experimental end-stations including low-energy electron microscopy (LEEM), photoemission electron microscopy (PEEM), μ -ARPES and nano-ARPES techniques	52
4.5	Illustration of the experimental geometry of the ARPES setup at MAESTRO beamline	54
4.6	Beam layout used to test the capillary optics at MAESTRO beamline. Reproduced from	54
4.7	Illustration of the dual undulator beamline with micro-focusing at Elettra synchrotron facility	55
4.8	Panel (a): Photograph of the NanoESCA end station at the Elettra synchrotron in Trieste, Italy. The preparation chamber is employed with in-situ surface preparation and characterization techniques. The NanoESCA microscope can be operated in a variety of modes, as shown in panel (b). Panel (c) shows the scheme of the NanoESCA. Adapted from	57
5.1	Left: Optical micrograph of a WSe ₂ monolayer (yellow) partly placed on 30 nm h-BN (red) and partly placed on a Si(001) substrate. A multi-layer WSe ₂ flake (blue) creates an electrical contact between the monolayer WSe ₂ flake and the silicon substrate. The scale bar is 20 μ m. Center: Spatial map of the integrated photoluminescence signal of the WSe ₂ monolayer excited at 660 nm. Right: Representative photoluminescence spectrum of the WSe ₂ monolayer.	62

- 5.2 (a) Optical micrograph of a WSe₂ monolayer flake (yellow) and multi-layer WSe₂ flake (blue dashed line) placed on a Si(001) substrate. The scale bar is 10 μm . (b) PEEM image taken by a Hg lamp at the NanoESCA beamline with a field of view of 60 μm . (c) LEEM image of the optical micrograph taken at an electron energy of 70 eV. (d,e) μ -LEED images were acquired on monolayer and multi-layer region on the WSe₂ sample, respectively. It shows sharp features at multi-layer part indicating the 6-fold crystal symmetry. LEEM and μ -LEED experiments were performed at Jerzy Haber Institute of Catalysis and Surface Chemistry, Polish Academy of Sciences, Kraków, in collaboration with Prof. Nika Spiridis's group. (f) Constant energy map (CEM) at $E - E_{\text{VBM}} = 0.4$ eV and (g) is the $E(k)$ cut along $K-\Gamma-K'$ on the monolayer part of WSe₂. 63
- 5.3 Characterization of sample A: (a) Schematic model of the sample configuration. Different nanosheets are denoted by blue, red, and gray colors. (b) Optical image of the twisted SL and BL WSe₂/graphite/n-Si, and (c) the spatial photoemission intensity map of the integrated intensity of the valence band near the Γ_0 point of WSe₂. (d) Set of normal emission ARPES maps at $h\nu = 147$ eV at white boxes indicated in (c). (e) Normal emission EDCs at boxes 6 and 7. 67
- 5.4 Characterization of sample B: (a) Optical image of the twisted SL and BL WSe₂/graphite/n-Si, and (b) the spatial photoemission intensity map of the integrated intensity of the valence band near the Γ_0 point of WSe₂. (c) Set of normal emission ARPES maps at $h\nu = 147$ eV at black boxes indicated in (b). (d) Normal emission EDCs at boxes 7 and 10. 68
- 5.5 Band structure of different regions of WSe₂ flake by nano-ARPES. Panel (a) shows the nano-ARPES image obtained by integrating intensity from 0.5 eV to 0.9 eV. Panels (b,c) show the band dispersion taken at $h\nu = 100$ eV along the $\Gamma-K$ direction of the Brillouin zone from the two regions labeled in panel (a) by green and orange dots. 70
- 5.6 Sample A: (a) $E_B(k_{\perp})$ map made from set of normal emission EDCs for $h\nu$ between 80 and 150 eV. (b) EDC profiles taken at non-dispersive features of (a) at different photon energies. EDC profiles at $h\nu = 180$ eV and 90 eV are shown in (c), indicating a ~ 60 meV energy shift. . . 71
- 5.7 Sample B: (a) $E_B(k_{\perp})$ map made from set of normal emission EDCs for $h\nu$ between 80 and 150 eV. (b) EDC profiles taken at non-dispersive features of (a) at different photon energies. EDC profiles at $h\nu = 88$ eV and 146 eV are shown in (c), indicating a ~ 30 meV energy shift. . . . 71
- 5.8 ARPES spectra from WSe₂ SL and BL of sample B. (a) and (b) show maps from top and bottom SLs, and (c) from the BL. (d-f) show details of the maps for top SL, bottom SL, and BL, respectively, at $E_B = 1.2$ eV. Red and green dashed circles in (f) represent the positions of the Γ_1 from top and bottom layer, and black arrows depict the twist angle. . . 73
- 5.9 ARPES spectra from WSe₂ SL and BL of sample A. (a) shows the maps from the bottom SL and (b) from the BL. (c,d) show details of the maps from bottom SL, and BL, respectively, at $E_B = 1.2$ eV. Red and green dashed circles in (d) represent the positions of the Γ_1 from top and bottom layer, and black arrows depict the twist angle. 74
- 5.10 (a) Details of the spectra from sample A near the Γ_1 at $E_B = 1.14$ eV. (b) Same map as in (a) but with red and green circles indicating the positions of Γ_1 from top and bottom layers, respectively. (c,d) $E_B(k)$ cuts along the red and green dashed lines indicated in (b), respectively. (e) Same as (d) but with the guide line indicating the dispersion of the bottom layer Γ_1 band. 74

- 5.11 (a,b) Fermi level CEMs ($E_B = 30$ meV) for the bottom SL WSe₂/graphite in sample *B*. (c,d) Same for the top SL WSe₂/graphite. (e) CEM for the top SL WSe₂/graphite at $E_B = 1$ eV. (f) and (g) show $E_B(k_x)$ maps of zero order graphite *K* point and one of the copies along the trajectories indicated respectively by yellow and red dashed lines in (c). Red arrows in (c) and (e) identify selected copies of graphite *K* points, confirming conical shapes of their dispersions. (h) Arrangement of copies related to (d) with indicated \mathbf{G}_W vectors of SL WSe₂. Different color of the arrows reflect the trigonal symmetry of SL WSe₂. 76
- 5.12 Analysis of main graphite Dirac cone and its copies on SL WSe₂ and graphite lattice:(a-x) show the possible orientations between these 2D lattices from 2° to 25° twist angle. The black dots indicate the graphite Dirac cones, and the red dots are their replicas. 77
- 5.13 Overview of sample *C*. (a) Optical micrograph of twisted SL WSe₂ placed on graphite with the entire sample structure lying on the top of *n*-Si. (b) PEEM image of the sample taken with a Hg lamp at NanoESCA beamline at Elettra, where twisted SL and bulk WSe₂ flakes are represented by the dotted green lines and shaded green color regions, respectively. (c) $E(k_x)$ map at Γ_0 indicating single band at normal emission. 78
- 5.14 Maps measured on sample *C* at the NanoESCA beamline with *p*-polarized light at $h\nu = 40$ eV at 80K. (a) CEM of SL WSe₂/graphite at $E_B = 0.12$ eV. (b) same as (a) but overlaid with Dirac copies calculated for 17.2° twist angle between WSe₂ and graphite. (c) CEM at $E_B = 0.93$ eV, indicating the *K* points of graphite and WSe₂. The measurement was performed by using linearly *p*-polarized light at 40 eV and at $T \sim 80$ K 79
- 5.15 Constant energy cuts at $E_B \simeq 0.11$ eV: (a,b) Fermi surface of the top and bottom monolayer of WSe₂ of sample *B*. The color scale is saturated to highlight copies of the main graphite Dirac cone. The k_x and k_y scaling of each constant energy map are in \AA^{-1} 80
- 5.16 Panel (a) and panel (b) present the (k_x, k_y) -dependent constant energy maps taken at $E_B \simeq 0.9$ eV with the determined twist angles of sample *A* and *B*. The red and green arrows connect Γ_0 and Γ_{1top} , Γ_0 and $\Gamma_{1bottom}$ high symmetry points of WSe₂ bilayer structures indicating the twist angle between BL WSe₂. 81
- 5.17 Sample *B*: (a,d,g) Constant energy contours at $E_B \simeq 0.9$ eV taken around Γ_0 , Γ_{1top} and $\Gamma_{1bottom}$ respectively. (b,c,e,f,h,i) Extracted $E(k_x)$, $E(k_y)$ dispersions at different k_x and k_y cuts performed on all gammas, as indicated by dashed red and blue lines in (a,d,g). A white circle marking in the (a,d,g) indicates the center of for Γ_0 , Γ_{1top} , and $\Gamma_{1bottom}$ retrieved from 3D dataset. 82
- 5.18 Same as fig. 5.17 but for sample *A*. 83
- 5.19 Calculated orbital characters for the (a) freestanding SL, (b) AA' (2H)-BL, and (c) AA-BL WSe₂. 84
- 5.20 Selected maps from the BL of sample *B*. Top row (a-c): CEM at $E_B = 1$ eV for *p*-polarized light. Bottom row (d-f): CEM at $E_B = 1$ eV for *s* polarized light. Green dashed line in (a) shows the momentum trajectory for maps (b) and (e). Blue dashed line (d) shows the momentum trajectory for (c) and (f). Black dashed lines in (b) and (f) indicate the local VBM at Γ_0 and *K* points respectively. (g,h) EDCs of twisted BL WSe₂ of sample *B* taken at Γ_0 (b) and *K* (f). 85

- 5.21 Crossing between Γ_1 and graphite bands in sample *B*. (a) CEM at $E_B = 1.2$ eV; yellow dashed line shows the BZ trajectory for maps (b-c). (b) $E(k_y)$ showing the region where graphite and Γ_1 band cross; yellow dashed line depicts the graphite Dirac cone dispersion. (c) Magnified region of the crossing. Orange dashed line presents cut at graphite Dirac cone along k_x (d). 86
- 5.22 Atomic model and theoretical calculations for aligned (a,c) and 21.79° twisted (b,d) SL WSe₂ on graphene. The theoretical band structure is deconvoluted onto the Brillouin zone of the freestanding SL WSe₂. (e) and (f) show magnified areas of the green boxes in (c) and (d), respectively. Green lines (in all panels) show the band structure of a freestanding SL WSe₂, for comparison. 88
- 5.23 Theoretical calculations for twisted BL WSe₂ at two twist angle $60^\circ - 13.17^\circ(21.79^\circ) = 46.83^\circ(a-c)(38.21^\circ)(d-f)$. (a,d) Black and blue lines depict BZs of the two SLs and the network red lines the moiré BZs of the twisted layers. (b,e) Band structure unfolded onto the BZ one of the SL WSe₂. (c,f) Magnified region depicted by the green rectangle in (b). For comparison, green solid lines show the bands for the 2H BL WSe₂. 91
- 6.1 (a,c) are the optical micrographs of twisted SL and twisted BL of WSe₂ placed on graphite, and the entire sample structure is lying on the top of n-Si. (b,d) are the PEEM images of the samples taken with a Hg lamp, where, twisted SL, twisted BL and bulk WSe₂ flake are represented by the dotted green and gray lines and shaded green color region, respectively. 98
- 6.2 Scheme of the experimental setup: a circularly polarized light (40 eV) is focused onto the bulk WSe₂ crystal at an angle of incidence of 65° with respect to the surface normal, ejected photoelectrons are detected by the momentum microscope. The dashed contour represents the two-dimensional SBZ of 2H-WSe₂ with the high symmetry points (\bar{K} , $\bar{\Gamma}$, \bar{K}' , \bar{M}). 99
- 6.3 Bulk WSe₂: Panels (a,b) show ARPES maps at $E_B - E_{VBM} = 0.3$ eV taken by RCP and LCP incident light respectively. The CD signal is depicted in panel (c), with the hexagonal BZ represented by a black dotted hexagon and the high symmetry spots are marked. The energy-momentum cut along vertical ($\bar{K}' - \bar{K}'$, $\bar{K} - \bar{K}$) and horizontal cuts ($\bar{K}' - \bar{M} - \bar{K}$, $\bar{K} - \bar{\Gamma} - \bar{K}'$) are measured by RCP and LCP incident light utilizing 40 eV photons is shown in panels (d,g,j,m,p) and (e,h,k,n,q). Panels (f,i,l,o,r) correspond to CD-ARPES signals along the $\bar{K}' - \bar{K}'$, $\bar{K} - \bar{K}$, $\bar{K}' - \bar{M} - \bar{K}$, and $\bar{K} - \bar{\Gamma} - \bar{K}'$ cuts, respectively. Vertical and horizontal cuts are indicated by dotted green and blue lines, respectively. 100
- 6.4 Circular dichroism in momentum space at various energies $E_B - E_{VBM}$ measured for the bulk WSe₂. The radius of each constant dichroism map corresponds to 1.9 \AA^{-1} . The SBZ of WSe₂ is represented in $E_B - E_{VBM} = 0.3$ eV, with the high symmetry points designated by \bar{K} and \bar{K}' 102
- 6.5 Panel (a) and panel (b) show the scheme of the experimental setup of SL and BL WSe₂/graphite/n-Si. A circularly polarized light (40 eV) is focused at a 65° angle of incidence with respect to the surface normal onto the graphite \bar{K} bands. The dashed contour represents the SBZ of graphite with the high symmetry \bar{K} points. 103

-
- 6.6 Comparison between experimentally measured and theoretically calculated CD-ARPES: Panel (a, c) show experimental observation on twisted SL, twisted BL WSe₂/graphite structures, circular dichroism in momentum space was measured at various energies. On constant energy maps at $E_B - E_{VBM} = 0.3$ eV, the BZ for SL, BL WSe₂ is represented by green and dotted black hexagons with high symmetry points (Γ , K), whereas brown dotted lines represent the BZ for graphite. All the corners of the BZs represent the K points. Panel (b, d) shows the theoretical calculations on non-twisted SL WSe₂ and twisted BL WSe₂ layers. The radius of each constant dichroism map corresponds to 1.9 \AA^{-1} . Black arrows and ellipses indicate similarities between theory and experiments. 105
- 6.7 SL WSe₂/graphite: Panel (a,b) show ARPES maps at $E_B - E_{VBM} = 0.3$ eV taken by RCP and LCP incident light respectively. The CD signal is depicted in panel (c), with the hexagonal BZ represented by a black dotted hexagon and the high symmetry spots are marked. The energy-momentum cut along vertical ($K'-K'$, $K-K$) and horizontal cut ($K'-M-K$) are measured by RCP and LCP incident light utilizing 40 eV photons is shown in panels (d,g,j,m) and (e,h,k,n). Panels (f,i,l,o) correspond to CD-ARPES signals along the $K'-K'$, $K-K$ and $K'-M-K$ cuts, respectively. Vertical and horizontal cuts are indicated by dotted green and blue lines, respectively. 107
- 6.8 BL WSe₂/graphite/n-Si: Panel (a,b) show momentum maps taken by RCP and LCP incident light at $E_B - E_{VBM} = 0.3$ eV. Panel (c) depicts the CD-ARPES signals, with green and black hexagons denoting the BZ from both WSe₂ monolayers, and blue dotted lines along high symmetry points of WSe₂. Panel (d-i) show the $E(k)$ maps. 108
-

List of Tables

4.1	Spectroscopic features of the ANTARES beamline at SOLEIL.	50
4.2	Spectroscopic features of the MAESTRO beamline at ALS	53
4.3	NanoESCA Beamline specification.	56
4.4	Performance parameters of the NanoESCA microscope.	56
5.1	The calculated total energies and interlayer distances of twisted BL WSe ₂ for the stacking sequence where twisting is around the center of in-plane WSe ₂ hexagons. In these calculations SOC was not included. N_W is the number of W atoms per moiré unit cell. ΔE is the energy difference between the AA stacking rotated around the center of the hexagon, as compared to the aligned AA ($\theta = 0$) stacking; $\Delta E = E(AA) - E_{t,hex}(AA)$. $\Delta E_{t,hex} = E_{t,hex}(AA') - E_{t,hex}(AA)$ is the energy difference, between the twisted AA' and AA stackings with the rotation axis at the center of the hexagon. The energies are given in meV per W atom. The structural parameters (in Å) are given for AA' stacking twisted around the center of the W -Se hexagon: \bar{d}_{W-W} is the average interlayer out-of-plane distance (along z -axis) between W atoms, while Δd is the maximum out-of-plane difference of W atom positions within the layer, it represents the corrugation due to formation of the moiré pattern.	90

Chapter 1

Introduction

Transistors have revolutionized the electronic industry since 1947, when the first demonstrated version of a transistor as a speech amplifier was reported from Bell labs [1–4]. Following Gordon E. Moore [5], who predicted that the number of transistors on the computing chip would double every two years, the manufacturing of transistors has seen exponential growth. Successive decades acted as a playground to design and develop compact, cost-effective, and efficient transistors for commercial use. The refinement in high-quality silicon manufacturing has further propelled this development, with some limitations. This includes the size of transistors, which has seen a steady drop over few decades with added integration of multiple electronic components on the same chip for generating powerful electronic systems. After 52 years of the first commercially available microprocessor [6], silicon finally ran out the room at the bottom and reached a physical limit dictated by the quantum tunneling effect [7]. Hence, significant measures are required to fulfill the overgrowing demand and development.

The field of materials science is emerging, wherein efforts are devoted to probing already known materials while discovering new phases and related properties for advanced electronics. From the broadly classified group of materials, the layered systems have risen significantly to attention with intriguing properties. Specifically, the layered van der Waals (vdW) materials are promising and reliable contenders as the weak interlayer forces and strong intralayer covalent bonds allow easy exfoliation, while keeping intact the layer morphology. An example of this was first reported in 2004 by A.K. Geim and K.S. Novoselov [8], who successfully exfoliated atomically thin graphene using a scotch tape and were later awarded the Nobel Prize in Physics. Following this, numerous reports were published on single layer graphene possessing novel properties with further development of its use in commercial applications [9, 10]. Despite showcasing exceptional physical properties and electro-elastic capabilities, its bandgap and semi-metallic characteristics have limited its use in functional electronics [11–19].

The exciting graphene discovery sparked a surge of research activity, which swiftly expanded to other layered materials. Scientists described two-dimensional (2D) semiconductors such as MoS₂, WSe₂, and the wide band gap insulator BN, to mention a few, in addition to graphene [20–23]. As a result, all basic building blocks of classical electronics have 2D analogues. These layered materials can be held together vertically or laterally to form hetero-structures (HSs) by weak vdW forces to make so-called vdW HSs, also known as “atomic-scale Legos” [24, 25]. Furthermore, twisting the two stacked atomic layers or mixing materials with different lattice constants results in the emergence of novel physical features due to confinement at lower dimensionality, providing an unprecedented platform for the development of novel quantum materials and device design [26–31].

At the moment, we are in the midst of the electronic age’s transition stage. Future electronic technology will necessitate small size, high-speed, low-power transistors beyond the silicon-based electronics. After understanding the manipulation of the electronic charge, global attempts are being made to include and utilize the spin degree of freedom of the electron in order to create efficient devices. Spintronics (which employs electron spins) [32–35], valleytronics (which uses electron orbital moment as an extra degree of freedom) [36, 37], or a combination of the two approaches can be used by vdW materials to create electronic devices [38–40]. We are still in the early stages of 2D material research and development, and many basic and engineering problems must be overcome, before these materials can be used in industrial applications. Aside from significant gains in processing power and efficiency, plans for using vdW materials to construct a new generation of solar cells [41], light-emitting diodes (LEDs), displays, and sensors have been presented [42–44]. All critical components of a working device or circuit can be potentially integrated in a single membrane, allowing for highly flexible, foldable, adaptive, and wearable electronics.

The thesis is organized as follows:

- **Chapter 2** discusses the basic conceptual framework used in this thesis. It includes the explanation of the formation of the electronic band structure, photoemission spectroscopy that supports the main experimental method used, density functional theory (DFT), and characteristics of vdW materials, as well as the effect of spin-orbit coupling (SOC) on valley-based physics.
- **Chapter 3** gives a description of the fabrication process of the 2D mate-

rials and their vdW HSs using mechanical exfoliation and the dry transfer technique.

- **Chapter 4** gives an overview of the selected micro- angle-resolved photoemission electron spectroscopy (μ -ARPES) beamlines based at synchrotron facilities worldwide.
- **Chapter 5** presents the μ -ARPES studies on vdW HSs based on a twisted single layer (SL) and twisted bilayer (BL) configuration of WSe₂ lying on a graphite flake. Our primary objectives were to determine the position of the valence band maximum and investigate bonding and antibonding hybridization between WSe₂ bilayers at the Γ bands, as reported previously [45, 46]. We integrated experimental photoemission results with band structure calculations to address these aspects. Notably, we observe band replicas in experimental Fermi surface maps from twisted SL WSe₂/graphite. We also experimentally demonstrate photon energy-dependent intensity modulation of hybridized bands in twisted WSe₂ bilayers. Furthermore, we determine the twist angle between the WSe₂ monolayer and graphite flake using the position of the main π band replica of graphite. We visualize the characteristic features of individual monolayers in homo-bilayers beyond the first Brillouin zone (BZ) to determine the twist angles of homo-bilayer structures.
- **Chapter 6** presents the circular dichroism investigation in angle-resolved photoemission spectroscopy (CD-ARPES) on a twisted SL, BL, and bulk WSe₂ crystals. CD-ARPES measurements were performed with a momentum microscope at the NanoESCA, Elettra. This chapter focuses on K valley induced dichroic signals. We reported the combination of CD-ARPES experiments and DFT calculations, demonstrating that circular dichroism at K valleys of WSe₂ is due to pronounced valley orbital polarization.
- **Chapter 7** provides the summary and outlook of the presented results.

Chapter 2

Background and Literature Review

This chapter provides an outline of the fundamental theoretical notions that underpin this thesis. The study of crystals and their characteristics is the primary focus of solid-state physics. In addition to the crystal structure, the electronic characteristics of a solid are of particular importance. Therefore, the electronic band theory, its relevance in solid-state physics, and the experimental and computational methods used are discussed in detail.

2.1 Electrons in solids

One of the most significant achievements in condensed matter physics was Felix Bloch's formulation of band theory, which allowed a quantum mechanical explanation of delocalized electrons in crystals [47]. According to the Bloch theorem, the wave function for an electron in a periodic potential has a form of Bloch waves [48]

$$\psi(\mathbf{r}) = e^{i\mathbf{k}\cdot\mathbf{r}} \cdot u(\mathbf{r}) \quad (2.1)$$

where \mathbf{k} is the electron wave vector in the reciprocal space, \mathbf{r} is a position vector, and $u(\mathbf{r})$ is a function with the translational periodicity of the lattice with $u(\mathbf{r}) = u(\mathbf{r} + \mathbf{R})$, for all vectors \mathbf{R} of the Bravais lattice of the crystal. The Bloch waves are solutions of the single-electron Schrödinger wave equation

$$\mathcal{H}|\psi(\mathbf{r})\rangle = \left[-\frac{\hbar^2}{2m}\nabla^2 + V(\mathbf{r}) \right] |\psi(\mathbf{r})\rangle = E_n(\mathbf{k})|\psi(\mathbf{r})\rangle \quad (2.2)$$

where, n is a band index identifying the discrete energy eigenvalues $E_n(\mathbf{k})$

$$E_n(\mathbf{k}) = E_n(\mathbf{k} + \mathbf{G}) \quad (2.3)$$

$E_n(\mathbf{k})$ are themselves periodic with the reciprocal lattice vector \mathbf{G} . For a given value of \mathbf{k} , a set of discrete energy eigenvalues can be obtained. This continuum of quantum mechanical states with the same n forms an energy band, and $E_n(\mathbf{k})$ shows the dispersion relationship between the energy and momentum within the band. Since the band structure is periodic in \mathbf{G} , drawing the bands simply in the first Brillouin zone (BZ), which is the unit cell in the reciprocal space associated with the given crystal lattice, is sufficient. Within the first BZ, there is an equivalent solution for every \mathbf{k} vector. The ranges of allowed electron energies in a material are referred to as **allowed bands**. Besides that, certain energy ranges between two allowed bands may also exist that are completely devoid of any electronic states, and these regions are known as **forbidden bands** or **band gaps** [48] as shown in fig. 2.1(b). The band theory explains many of the electrical, optical and thermal characteristics of solid and has become an essential foundation for the study of modern solid-state physics.

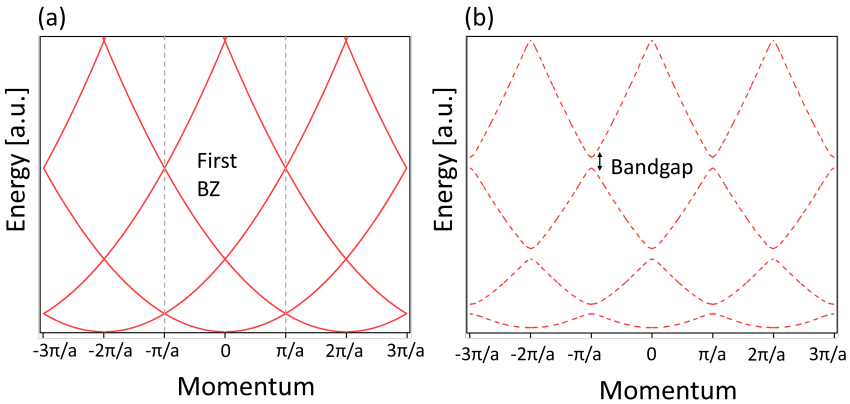


Figure 2.1: Electronic band structure of electrons in a periodic potential. Left panel represents periodic zone scheme of the band structure in a solid, with the dashed line representing the region of the first BZ while right panel shows the the opening of gaps at the BZ edge and in the center due to the lattice potential.

Since electrons are Fermions, the electronic ground state of the system shall fulfill the Pauli exclusion principle, meaning each electronic state can only be occupied by one electron or two with opposite spins. For metals at $T=0\text{K}$, the highest occupied state is referred to as the Fermi level E_F or the Fermi energy; in equilibrium at finite temperature electrons are distributed according to the

Fermi function, which determines the probability that an available energy state E will be filled with an electron at a particular temperature. The Fermi function is derived from Fermi-Dirac statistics and has the following form

$$f(E) = \frac{1}{\left(e^{\frac{E-E_f}{k_B T}} + 1\right)} \quad . \quad (2.4)$$

The electronic band theory can be used to categorize materials into metals, insulators, or semiconductors. In case of metals, the Fermi level, which distinguishes between the occupied and unoccupied states, cuts through the allowed electronic states, leaving them only partially filled. An arbitrarily small amount of energy is required to excite an electron at the Fermi level into an unoccupied state, resulting in a gain of non-zero total momentum in the form of an electric current flow. In case of an insulator, the Fermi level is located within the bandgap, which separates the filled electronic states called the “valence band” from the entirely unoccupied ones called the “conduction band”. The bandgap can only be bridged with a substantial amount of energy (if at all feasible), resulting in limited conductivity. When a significant number of electrons overcomes the band gap as a result of thermal excitation, the material is classified as a semiconductor. Small amounts of impurities can be added to pure semiconductors to alter their conductivity. This is referred to as doping. Even materials with relatively large band gaps can be classified as semiconductors, if acceptor or donor states can be created near the valence band (p-type) and conduction band (n-type) via doping.

2.2 Photoemission spectroscopy

The electronic band structure of a crystalline solid can be related to its physical properties such as electrical conductivity, optical behavior, magnetism, and chemical properties. The photoemission electron spectroscopy (PES) has become one of the most important methods in solid-state physics during the last several decades, allowing experimental imaging of the electronic states. It is often used to investigate the surface and bulk electronic structure of solid-state systems, including ferromagnets, superconductors, semiconductors, and two-dimensional systems such as graphene and transition metal dichalcogenides (TMDCs). In the following, a brief overview of the recognized standards of pho-

toemission theory will be given. A more in-depth treatment can be found in available dedicated textbooks [49–52] and review articles [53–56].

2.2.1 Photoemission process

The photoelectron spectroscopy approach is based on Heinrich Hertz (Karlsruhe) and Wilhelm Ludwig Franz Hallwachs's (Dresden) [57, 58] discovery of the photoelectric effect in the late 19th century, in which ultraviolet (UV) light causes a current flow through a solid. For many reasons, the observations appeared to be inconsistent at the time. First, the number of photoelectrons might be increased by increasing the light intensity, but the kinetic energy of the emitted electrons is not. Second, light with a frequency lower than a certain threshold cannot excite photoelectrons, regardless of how bright the light is. Third, the kinetic energy of the photoelectrons increased with the light frequency, but was independent of light intensity. Fourth, electrons are emitted instantaneously after illuminating light on the sample surface, as opposed to the classical treatment, in which atoms require some time to absorb enough energy before emitting electrons.

The conventional electromagnetic theory of light cannot explain all these findings. Albert Einstein [59] was able to address these issues in 1905 by postulating the quantum nature of light as an explanation. He proposed that the light is emitted, travels, and is eventually absorbed in discrete packets called photons with energy $h\nu$, for which he was awarded the Nobel prize in Physics in 1921. Einstein postulated a formula for the kinetic energy of the photoelectrons from a bound state in a solid:

$$E_{kin} = h\nu - E_{bin} - \phi \quad (2.5)$$

where E_{kin} is the kinetic energy of the emitted photoelectrons, $h\nu$ is the energy of the incoming light, where ν is the photon frequency, and h is the Planck's constant ($\sim 4.135 \times 10^{-15}$ eV·s), ϕ is the work function of the material (typically 4–5 eV for most materials), i.e., the minimum energy required to excite an electron out into a vacuum, and E_{bin} is the binding energy of the electron inside the solid relative to the Fermi energy E_F that needs to be provided to release the electron from the nucleus [49].

When an electron is excited by a photon of the energy $h\nu$, the binding energy E_{bin} and material work function ϕ must be overcome in order for the electron

to exit the solid. Although the binding energy cannot be directly measured, the information is stored in the kinetic energy distribution of the emitted photoelectrons for monochromatic excitation, according to eq. 2.5. In practice, the sample and the analyzer are electrically connected to the same potential so that their chemical potentials are identical. Hence, in most of the cases determining the work function of the material is unnecessary; only the work function of the analyzer must be known. Depending on the energy of the incoming photons, there are two types of photoemission spectroscopy investigations. In X-ray photoemission spectroscopy (XPS), photons in the X-ray spectrum (few 100 eV- few keV) are used to excite core levels at higher binding energies. The core level spectrum appears as a distinct line due to the discrete energy levels at which the atoms are bound, reflecting the unique chemical state of the material. Photons in the UV range, on the other hand, are used to excite valence electrons (ultraviolet photoemission spectroscopy (UPS)), which employ energies ranging from 5 to ~ 200 eV. This approach is used to investigate electrons that are more delocalized and loosely bound, hence forming the electronic band structure of the material. Nowadays, X-ray photons can also be used to measure the electronic bands [60] and there are other types of photoemission spectroscopies such as ambient pressure photoemission [61], hard X-ray photoelectron spectroscopy (HAXPES) [62], time-resolved ARPES [63] and spin-polarized ARPES [64] available, too.

The sudden approximation

In general, the photoemission process is a complex phenomenon, because when an electron is removed from the system, the rest of the system will respond to the photoelectron's behavior. Thus, we need to consider the interacting electron picture and employ a many-body approach. A commonly used approach to theoretically describe such a many-body process is to assume that the excitation and the escape of the photoelectron from the exciting area are considerably faster than the relaxation of the system. This approximation is known as **sudden approximation**, and it simplifies the problem to a single-particle problem in a stationary environment [49]. One of the sudden approximation's drawbacks is in the low kinetic energy range, which is related to the low electron speed, since their escape time is closer to the relaxation time and the fact that local potential fluctuations caused by the electron-hole become increasingly significant [53, 65].

The photoexcitation of the electron is estimated as an instantaneous process using the sudden approximation method. In this limit, the system is considered in a one-electron-problem that is excited by the photon with the energy $h\nu$ from its occupied initial state $|i\rangle$ to an unoccupied final state $|f\rangle$ with binding energies E_i and E_f , respectively. The transition probability from the $|i\rangle$ to $|f\rangle$ electronic states is given by the *Fermi's Golden Rule* [66]

$$P_{i \rightarrow f} = \frac{2\pi}{\hbar} |\langle f | \mathcal{H}_p | i \rangle|^2 \delta(E_f - E_i - h\nu) \quad (2.6)$$

Here, \mathcal{H}_p is the photoexcitation perturbation Hamiltonian, and the δ function incorporates energy conservation.

It is evident from equation 2.6 that the probability of the photoemission process is always dependent on a pair of $|i\rangle$ and $|f\rangle$ states, with the associated *transition matrix element*, $M_{f \rightarrow i}$ being essentially determined by the symmetries of the electronic wave functions and the perturbation Hamiltonian \mathcal{H}_p

$$M_{f \rightarrow i} = \langle f | \mathcal{H}_p | i \rangle \quad (2.7)$$

For low photon flux densities, \mathcal{H}_p can be estimated within the *linear response theory* and takes the form

$$M_{f \rightarrow i} = -\frac{e}{mc} \langle f | \hat{A} \cdot \hat{p} | i \rangle \quad (2.8)$$

\hat{A} is the vector potential, and \hat{p} is the electron momentum operator. For the photon energies within the UV and soft X-ray ranges, the wavelength of the electromagnetic field is typically assumed to be large compared to interatomic distances. It implies that the vector potential \hat{A} can be assumed to be locally constant, which leads to the so-called *dipole approximation* and the matrix element becomes

$$M_{f \rightarrow i} \approx -\frac{ie}{\hbar c} A_0 (E_f - E_i) \langle \psi_i | \hat{P} \cdot \hat{r} | \psi_f \rangle \quad (2.9)$$

Here, A_0 is the amplitude of the vector potential, \hat{P} is the electric polarization vector of the photon and the wave functions of the initial and final states are ψ_i and ψ_f , respectively. From equation 2.9, $M_{f \rightarrow i}$ can be analyzed with respect to

the symmetries of initial and final states as well as the polarization of the light to define dipole selection rules [54]. They may be used to qualitatively evaluate photoemission spectra in terms of allowed/forbidden electronic transitions.

However, the photoemission model given above is just a single-electron model. Real electronic systems are made up of many electrons that interact with one another. To approximate the many-particle case, a *single-particle spectral function* $A(\mathbf{k}, E)$ can be introduced. The probability of removing and adding a single-electron with energy E and wave vector \mathbf{k} to the N -electron system is given by $A(\mathbf{k}, E)$. Both of these concepts may be represented in terms of the *complex self-energy* $\Sigma(\mathbf{k}, E)$ term, which accounts for the renormalization of the electron energy ($\text{Re}\Sigma$) [67] and the finite life time ($\text{Im}\Sigma$).

$$A(\mathbf{k}, E) = -\frac{1}{\pi} \frac{\text{Im}\Sigma(\mathbf{k}, E)}{[E - \epsilon - \text{Re}\Sigma(\mathbf{k}, E)]^2 + [\text{Im}\Sigma(\mathbf{k}, E)]^2} \quad (2.10)$$

Here, ϵ represents the energy of the non-interacting electrons.

2.2.2 Angle-resolved photoemission process

To fully understand the electronic band structure of the material, the binding energy of photoelectrons must be evaluated as a function of their momentum. In the 1960s, it was realized that a momentum-dependent band structure could be mapped from the emission angles distribution of the photoelectrons and the energy dependence of the photoemission spectra [68]. Nowadays, the polar (ϑ) and azimuthal (φ) emission angles of the emitted photoelectrons can be precisely measured. For this purpose, the key technique used is angle-resolved photoemission spectroscopy (ARPES). As the name implies, ARPES directly measures the kinetic energy of the photoelectrons as a function of the emission angles. ARPES has become a powerful tool for revealing crucial information on the electronic band structure and many-body interactions in many materials due to significant advancements in recent decades [69, 70].

It is critical to distinguish between three separate electron wave vectors for all the following considerations:

- \mathbf{k}_i : Before excitation, the initial state wave vector of the electron in the solid
- \mathbf{k}_f : After excitation, the final state wave vector of the electron in the solid

- $\mathbf{K}=\mathbf{p}/\hbar$: the momentum vector of the electron emitted into vacuum¹

Figure 2.2(a) depicts a schematic design of the experimental apparatus utilized in the ARPES experiment. It consists of a photon source, a hemispherical analyzer, and a 2D multi channel plate (MCP) detector. A gas discharge lamp, laser, or synchrotron radiation can all be used as photon sources. The typical beam spot for gas discharge sources is in order of 1 mm²; at synchrotron nowadays, there is a possibility to reduce the beam spot to few hundred nanometers by using special focusing optics. Concerning the analyzer, it acts as an angle-resolving energy filter. With the availability of the 2D detector, the dispersion along the hemisphere projects an energy window on one dimension and the angular distribution of photoelectrons images via electron lenses orthogonally onto the second dimension of the electron detector. As illustrated in fig. 2.2(a), the in-plane momentum may be changed by rotating the sample around ϑ and φ , respectively. This setup allows one to analyze the kinetic energy of the photoelectrons as a function of the angular distribution along the analyzer slit direction.

It is sufficient to measure E_{kin} and emission angles ϑ and φ to determine the momentum vector for the individual components in spherical coordinates in vacuum are as follows:

$$K_x = \frac{1}{\hbar} \sqrt{2mE_{kin}} \sin\vartheta \cos\varphi \quad (2.11)$$

$$K_y = \frac{1}{\hbar} \sqrt{2mE_{kin}} \sin\vartheta \sin\varphi \quad (2.12)$$

$$K_z = \frac{1}{\hbar} \sqrt{2mE_{kin}} \cos\vartheta \quad (2.13)$$

Where $\hbar = \frac{h}{2\pi}$ is the reduced Planck's constant, ϑ and φ are the emission angles of the photoelectrons, and m is the electron rest mass.

One can assume the momentum component K_x is parallel to the sample surface and the slit entrance direction. Then the second component, K_y , is orthogonal to the K_x and parallel to the sample surface, while the third momentum component, K_z , is the sample normal. The goal is to reconstruct the electronic dispersion

¹Within this thesis, the terms “wave vector” and “momentum” will be used interchangeably for simplicity. $\mathbf{K} = \frac{\mathbf{p}}{\hbar}$ connects the wave vector \mathbf{K} and the mechanical momentum \mathbf{p} . All momentum/wave vector values will be presented in wave number units: $k[\text{\AA}^{-1}]$.

relation $E(\mathbf{k})$ inside the material using momentum conservation and eq. 2.5 from the measured quantities.

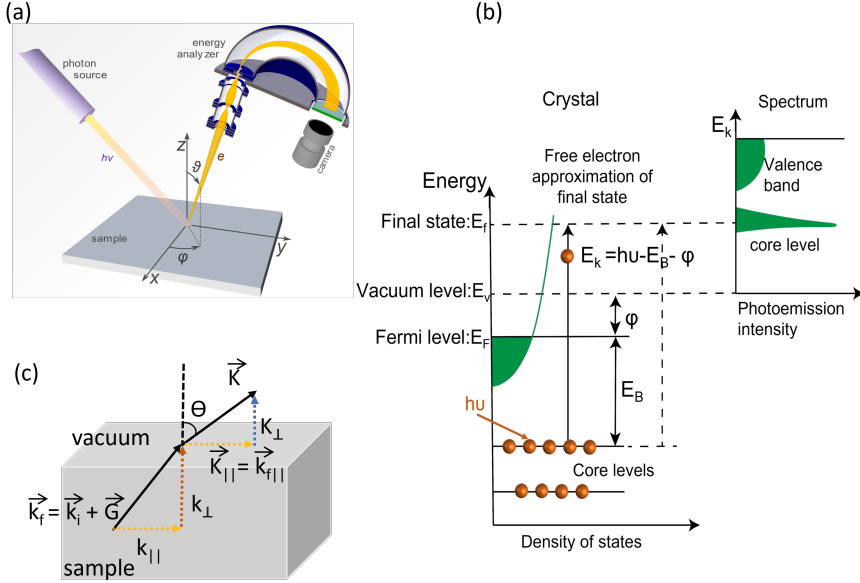


Figure 2.2: Panel (a) shows the schematic of a typical ARPES experiment [71]. Panel (b) depicts the energy diagram for the photoemission process where an electron (orange sphere) in a solid is excited by photon energy ($h\nu$). The kinetic energy (E_k) of the electron is given as a function of the excitation energy ($h\nu$), binding energy (E_B), and the work function of the material (ϕ). Panel (c) illustrates the initial and final momentum vector inside and outside the solid with the parallel components conserved while the perpendicular component is not conserved. Reproduced from [49, 69].

2.3 The three-step model

Several theoretical models have been proposed to describe the photoemission process in experiments. In 1964, Berglund and Spicer proposed a phenomenological description in which the photoemission process is subdivided into three steps. Within this model, *optical excitation* between two Bloch states (i.e. initial and final) in sample bulk, *propagation of the photoelectron* towards the sample surface and *escape of the photoelectron* into the vacuum are all addressed separately. The three-step model is the simplest theoretical way to qualitatively

characterize photoemission in a single-electron picture. Photoemission has been refined, resulting in a one-step process that is less transparent [72]. In one-step model one considers excitation between the initial single-electron Bloch state and the so-called “time-reversed low-energy electron diffraction (LEED) state”, which is free-electron-like in a vacuum while decaying into the crystal.

The individual steps of the three-step model will be reviewed further in the following sections:

1st step: Optical excitation

The first step occurs within the solid and its band structure. In the initial stage of the three-step model, electrons are excited from their stationary ground Bloch state $|i\rangle = |E_i, \mathbf{k}_i\rangle$ of a valence band to a final Bloch state $|f\rangle = |E_f, \mathbf{k}_f\rangle$ of a conduction band. Given that energy and momentum must be conserved, the following relationships hold:

$$E_f = E_i + h\nu \quad (2.14)$$

$$\vec{k}_f = \vec{k}_i + \vec{k}_{ph} + \vec{G} \quad (2.15)$$

Experiments are often carried out with photon energy of less than 100 eV, which corresponds to a photon momentum, $k_{ph} = h\nu/c \approx 0.051 \text{ \AA}^{-1}$. For many materials, the typical size of the BZ is approximately π/a , corresponding to a length scale of 1 \AA^{-1} . Thus, the momentum carried by the photon is in the UV or soft X-ray regime is small compared to the typical BZ size. Neglecting k_{ph} , this leads to the momentum conservation within the reduced zone scheme, i.e. $\vec{k}_f = \vec{k}_i + \vec{G}$, with the direct (vertical) transitions. By adding the reciprocal lattice vector \mathbf{G} , the momentum conservation is preserved. Various \mathbf{G} provide a variety of propagation directions and, as a result, various emission angles for the same initial state $|i\rangle$.

2nd step: Propagation of photoelectron inside the crystal

The second stage of the photoemission process describes how the excited photoelectron in the final state $|f\rangle$ propagates through the crystal towards the surface. The transmitted photoelectrons are subjected to elastic and inelastic scattering interactions, including electrons, phonons, and defects, resulting in a substantial reduction in their undisturbed propagation range. The average distance

between two inelastic scattering processes is described by the inelastic mean free path (IMFP) of the electrons. This scattering is commonly characterized as an exponential damping law with an inelastic mean free path (λ):

$$I(d) = I_0 \exp\left(-\frac{d}{\lambda}\right) \quad (2.16)$$

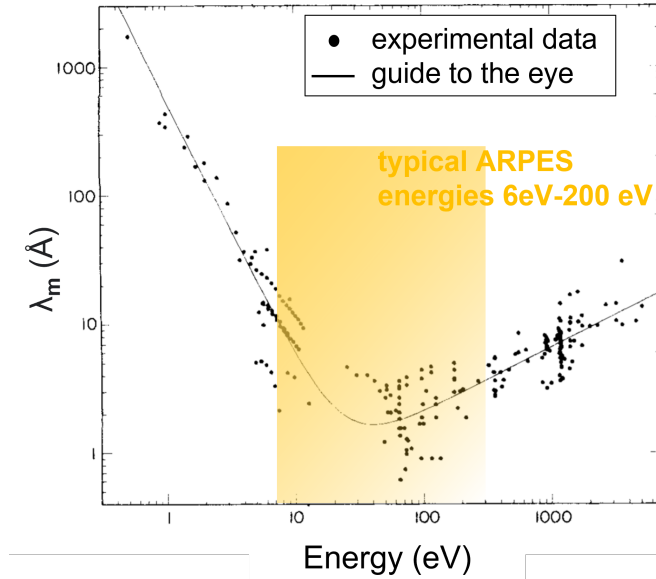


Figure 2.3: Plot depicting the universal curve of inelastic mean free path of photoelectrons as a function of their kinetic energy inside the material. A solid line represents the empirically calculated universal curve and experimental data points of the IMFP of diverse materials. The mean free path for the relevant energy is about few Å [73].

$I(d)$ is the photoemission current attenuation as a function of path length d . The experimentally determined IMFP of several materials and the phenomenological universal curve are shown in fig. 2.3. According to equation 2.16, 95% of the probed photoemitted electrons comes from a $\approx 3 \cdot \lambda$ depth due to the exponential $I(d)$ decay. This is also known as the PES probing depth or maximum escape depth. This significantly influences PES as an experimental approach, making it very sensitive to surface conditions. Because of the limited escape depth, ARPES is always performed in an ultra-high vacuum as even surface contaminations in the atomic monolayer domain substantially influence the experiments.

The general shape of the IMFP curve as a function of the kinetic energy of the excited electrons is universal for all materials. For ARPES experiments, a typical incident photon beam has an energy range of $\approx 6 \text{ eV} - 200 \text{ eV}$ with a mean free path of a few angstroms ($\approx 1 \text{ \AA} - 20 \text{ \AA}$). Therefore, even if the X-ray beam penetrates further into the crystal, the elastic photoelectrons are emitted mostly from the first layers of the sample surface. The inelastically scattered electrons contribute to the photocurrent with a broad and featureless background (referred to as secondary-electron background), whereas elastically scattered electrons can produce sharp peaks that can be related to the initial state electronic structure of a material.

At low kinetic energies ($\sim 5 \text{ eV}$) in the universal curve, electrons cannot exceed the work function and exit the sample; the energy scale is linked to the Fermi level, implying that the extremely low energy range cannot be detected in photoemission. Furthermore, the IMFP curve exhibits a steep rise here; it also predicts a probing depth of 1 - 10 nm; thus, the actual escape depth in ARPES experiments is often unknown, and the steep increase at lower energies is still debatable.

3rd step: Escape of photoelectron into vacuum

The last step in this model describes the escape of photo excited electrons from the surface to the vacuum, where the transition of the photoelectron from the final state $|f\rangle$ within the crystal to the free-electron plane wave state $|v\rangle$ in vacuum takes place. This step relates the measured emission angles and electron momentum in vacuum $|\mathbf{K}\rangle$ to the initial crystal momenta $|\mathbf{k}\rangle$.

The major difficulty in defining this step is that the surface is in the normal direction, and the potential barrier by the work function of the crystal violates translation symmetry. These issues can be handled by assuming that the momentum component parallel to the surface is conserved within a reciprocal lattice vector \mathbf{G}_{\parallel} in the surface Brillouin zone (SBZ). This is a reasonable assumption, because the surface does not disrupt the crystal symmetry of the parallel components. However, more than one value of k_{\perp} might contribute to the photoemission signal at the same emission angle. In addition, it is reasonable to assume that the surface potential barrier has the same symmetry as the surface lattice and that its gradient is predominantly perpendicular.

As a result, the parallel components of the wave vector, i.e., k_x and k_y , remain

good quantum numbers during the surface transition, while the electron wave vector component normal to k_{\perp} does not. Thus, the parallel initial electron momentum may be easily calculated from the observable values E_{kin} and ϑ (emission angle of the photoelectrons).

$$k_{fx,\parallel} + k_{fy,\parallel} = \mathbf{k}_{\parallel} = \mathbf{K}_{\parallel} = \sqrt{\frac{2m}{\hbar^2} E_{kin}} \sin \theta \quad (2.17)$$

Going to larger ϑ angles, it is possible to probe the electrons with \mathbf{k}_{\parallel} lying in higher-order Brillouin zones. However, to investigate the entire three-dimensional (3D) electronic band structure ($E(\mathbf{k})$), the perpendicular component of k must also be identified, which is not at all straightforward. A common method for determining k_{\perp} is to utilize the *free-electron final-state* (FEFS) model where the final state is approximated as a free-electron state. Since the photoemission process occurs in the presence of a crystal field, this is merely a rough estimate. At high photon energies, this model becomes more realistic, because the electron is subjected to less impact from the crystal field. Although the free-electron model is a rough approximation, it has shown to be a useful tool for determining band information along the k_z axis.

For the final state, it is assumed that the potential may be approximated as constant. By introducing the phenomenological inner potential V_0 , it is possible to map the final state directly to the state of the emitted electron. Within the formalism of the FEFS model, and making use of $E_f = E_{kin} + \phi$ and $E_f(\mathbf{k}) = \frac{\hbar^2(k_{\parallel}^2 + k_{\perp}^2)}{2m} - E_0$, and equation 2.17, the perpendicular component is approximated as follows

$$k_{\perp} = \sqrt{\frac{2m}{\hbar^2} (E_k \cos^2(\theta) + V_0)} \quad (2.18)$$

The inner potential $V_0 = E_0 + \phi$ corresponds to the energy distance between the lowest energy level of the valence band E_0 and the vacuum level. The inner potential complicates the 3D band structure mapping, because it can only be empirically determined using a tunable light source, such as a synchrotron. There are several schemes for determining V_0 , including optimizing the agreement between experimental data and calculations, searching for symmetries and periodicity in observed data points via experimental band mapping, and purely theoretical band structure calculations of all electronic states. It should be em-

phasized that the nearly-free electron approximation for final states is predicted to work well for materials with a simple spherical (free-electron-like) Fermi surface, such as alkali metals, as well as at high-energies, where the crystal potential is a negligible perturbation.

This thesis will mainly focus on the electronic band structure of twisted monolayers and bilayers of transition metal dichalcogenides, notably WSe_2 . Monolayers and bilayers of WSe_2 are two-dimensional system; thus, there is no dispersion along k_{\perp} .

2.4 Spin-orbit coupling in solids

The term spin-orbit coupling (SOC) describes the interaction between the spin \mathbf{S} of a particle and its orbital momentum \mathbf{L} around the nucleus, which leads to many interesting phenomena in the electronic structure of solids, such as the emergence of spin-polarized states in non-magnetic materials [74]. This effect exists in atoms and solids, including 2D materials. In the study of spintronics, the SOC is an important effect that plays a crucial role from a technical standpoint [75].

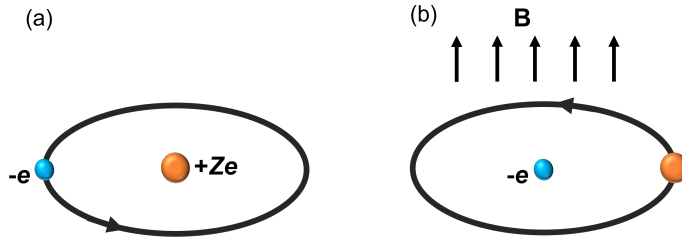


Figure 2.4: Panel (a) shows an electron moving around a nucleus as observed from the nucleus's reference frame. Panel (b) illustrates, in the reference frame of the electron, that the nucleus seems to be revolving about it. As a result, an upward-directed magnetic field is experienced by the electron.

Briefly, we first explain SOC in atoms as shown in fig. 2.4. Within the classical picture, in the rest frame of the electron, the nucleus orbits around it. Since the nucleus is a charged particle, its orbiting motion generates an effective magnetic field that interacts with the electron. The energy of the electron varies depending on the direction of the spin with respect to the effective magnetic moment. This results in the lifting of the energy degeneracy as a consequence of the SOC.

In solids, one should differentiate between core levels and dispersing energy levels while discussing the SOC effect. At the core level, the electronic states have no dispersion and are isolated by significant potential barriers, implying that they contribute insignificantly to the neighboring atoms. Thus, core states can be considered similar to atomic orbitals. In the framework of a non-relativistic approximation to the Dirac equation, SOC can be expressed by the Hamiltonian \hat{H}_{SOC} of an isolated atom:

$$\hat{H}_{SOC} = \xi(\hat{\mathbf{L}} \cdot \hat{\mathbf{S}}); \xi = \frac{e^2}{2\pi\epsilon_0 m^2 c^2} \cdot \frac{Z}{r^3} \quad (2.19)$$

where ξ is the SOC strength linearly related to atomic number Z and inversely proportional to the atomic radii r . This helps to explain the strong SOC in core levels (several eV) and a considerably smaller influence on weakly bound, dispersive electronic bands (few hundred meV). The \hat{H}_{SOC} implicitly includes the relationship between spin $\mathbf{S} = \frac{\hbar}{2}\boldsymbol{\sigma}$ and orbital momentum $\mathbf{L} = \mathbf{r} \times \mathbf{p}$. Equation. 2.19 assumes a spherically symmetric potential, whereas, for delocalized states, the symmetry is defined by the crystal structure.

In general, the symmetries of the system are crucial for the electronic band structure. An infinite crystalline solid can be time-reversal symmetric as well as spatial inversion symmetric where the electron spin can be defined as (\downarrow , \uparrow). These symmetries can lead to following constraints on band energies:

$$\left. \begin{array}{l} \text{time-reversal: } E(\uparrow, \vec{\mathbf{k}}) = E(\downarrow, -\vec{\mathbf{k}}) \\ \text{inversion: } E(\uparrow, \vec{\mathbf{k}}) = E(\uparrow, -\vec{\mathbf{k}}) \end{array} \right\} \Rightarrow E(\uparrow, \vec{\mathbf{k}}) = E(\downarrow, \vec{\mathbf{k}}) \quad (2.20)$$

The presence of inversion symmetry in combination with time-reversal symmetry leads to *Kramers degeneracy*. Within a centrosymmetric crystal, *Kramers degeneracy* governs that each Bloch state $E(\uparrow, \vec{\mathbf{k}})$ is degenerate with a corresponding state $E(\downarrow, \vec{\mathbf{k}})$ in the absence of a magnetic field, with the two states having the same energy. This is because time-reversal symmetry implies that the Hamiltonian describing the system is invariant under a reversal of time, which means that the energy levels must be symmetric with respect to spin. Moreover, SOC is capable of lifting this degeneracy between spin-up and spin-down states, making it a promising source of spin-polarized electronic states. The emergence of spin-polarized electronic states via SOC necessitates the breaking of inversion symmetry. The inversion symmetry can be violated by either the bulk crystal

structure itself or a structural asymmetry such as a surface or an interface. In non-magnetic crystals, such as WSe₂, MoS₂, in the presence of the time-reversal symmetry, spin-polarized electronic states can be achieved by violating inversion symmetry through SOC. This violation of inversion symmetry generates a difference in energy between spin-up and spin-down states, leading to spin polarization. The combination of Kramers degeneracy and SOC is critical for understanding the electronic properties of materials, and can give rise to topologically non-trivial electronic states.

The role of the crystal symmetry in the context of SOC is one of the key characteristics of WSe₂, which are central topics of this study. In reciprocal space, however, one finds the *time-reversal invariant momenta* (TRIM), which are the points that can be connected to themselves via both a time-reversal operation and a reciprocal lattice vector. In general, TRIM (Γ_i) points in the bulk are characterized by $-\Gamma_i = \Gamma_i + \mathbf{G}$ where \mathbf{G} is a bulk reciprocal lattice vector. The periodicity of the reciprocal lattice forbids breaking of time reversal symmetry at TRIM points. In the bulk BZ, the Γ point is always a TRIM point of any crystal structure, since $\mathbf{k} = 0$ cannot be reversed under time-reversal symmetry. The crystal structure determines the specific TRIMs. To illustrate this situation, let's consider the M and K points of the hexagonal BZ of WSe₂. The M point is a high-symmetry point that lies on the edge of the hexagonal BZ. It is a TRIM point because it is connected to itself under time-reversal symmetry via the reciprocal lattice vector \mathbf{G} , which is the shortest vector that connects equivalent points in the BZ. In contrast, the K point in the hexagonal BZ of WSe₂ is not a TRIM point because it is not connected to its time-reversed partner, K' , via a reciprocal lattice vector. The time-reversal operation changes the sign of the wavevector, so the wavevector at K is opposite in sign to the wavevector at K' . Therefore, K and K' are not connected under time-reversal symmetry. These TRIM points have important implications for the electronic properties of materials.

2.5 Density functional theory

The main technique used in this study is ARPES, which allows a relatively direct, experimental access to the electronic band structure of the material. Comparing the experiment to a detailed theoretical description of the electronic

structure, on the other hand, may frequently widen the knowledge acquired from the experiments. All of the ARPES data reported in this study are compared to ab-initio calculations based on density functional theory (DFT), which are performed at Peter Grünberg Institut-1 (PGI-1) Forschungszentrum Jülich by Dr. Hyun-Jung Kim and Dr. Gustav Bihlmayer. This section will cover the fundamental ideas of DFT.

2.5.1 The Kohn-Sham equations

To characterize the state of a many-body system with N number of interacting particles, one must compute the many-body wave function. The main problem associated with this task is the complexity of the quantum mechanical treatment of many-body wave functions, which becomes numerically demanding and is not manageable even by high-power computers. Thus, the first approximation which is always employed is the *Born-Oppenheimer approximation* [76], where the kinetic energy of the nuclei can be neglected, considering the nuclei to be frozen due to the large mass difference between electrons and nuclei. This is the first step towards an effective description of a system of interacting particles, before the electronic band structure can be calculated.

Density functional theory is a popular and commonly used many-body approach for calculating electronic structures. To simplify the problem, DFT uses the Hohenberg-Kohn-Sham theorem, which states that (i) the N particle ground state wave function $\psi(\mathbf{r}_1, \mathbf{r}_2, \dots, \mathbf{r}_N)$ and the potential $V(\mathbf{r})$ are uniquely determined by the particle density distribution $n(\mathbf{r})$ and (ii) the total energy can be expressed as a functional of the electron density $E_{tot} = E[n(\mathbf{r})]$, which is stationary under first order density and energy variations [77, 78]. This leads to the Schrödinger-like equation for the eigenstates $\phi_i(\mathbf{r})$ of the auxiliary system:

$$\left[-\frac{\hbar^2}{2m} \nabla^2 + V(\mathbf{r}) + e^2 \int \frac{n(\mathbf{r}')}{|\mathbf{r} - \mathbf{r}'|} d\mathbf{r}' + \frac{\delta E_{xc}[n(\mathbf{r})]}{\delta n(\mathbf{r})} \right] \phi_i(\mathbf{r}) = \epsilon_i \phi_i(\mathbf{r}) \quad (2.21)$$

where, $\frac{\hbar^2}{2m} \nabla^2$, $V(\mathbf{r})$, and $e^2 \int \frac{n(\mathbf{r}')}{|\mathbf{r} - \mathbf{r}'|} d\mathbf{r}'$ are the kinetic energy and Coloumb interactions (e-e, n-e) terms. The last term $\frac{\delta E_{xc}[n(\mathbf{r})]}{\delta n(\mathbf{r})}$ is called the exchange-correlation potential and includes all the electron-electron interactions and correlations. In equation 2.21 ϵ_i is the Lagrange multiplier for the minimization problem and

$\phi_i(\mathbf{r})$ for the quasiparticle wavefunctions.

Provided that the $E_{xc}[n(\mathbf{r})]$ functional is known, one can identify the density that zeroes the functional derivative of the energy with respect to $n(\mathbf{r})$ by minimizing the energy. The reality is, we don't know what the $E_{xc}[n(\mathbf{r})]$ functional is [79]. Therefore, establishing good yet efficient approximations of the energy functional is the main quest in DFT.

2.5.2 Approximation for the exchange-correlation energy functional

The exchange-correlation (XC) functional does not have an accurate analytical form. A rather simple and remarkably good approximation is the so-called *local density approximation* (LDA) [80, 81], which replaces the exact functional $[E_{xc}]$ by

$$E_{xc}^{LDA}(n) = \int n(\mathbf{r})\epsilon_{xc}^{LDA}(n(\mathbf{r}))d\mathbf{r} \quad (2.22)$$

Where $\epsilon_{xc}^{LDA}(n)$ is a function, but not a functional of the density. This function is employed locally at each position \mathbf{r} in eq. 2.22, with the value approximated by $n = n(\mathbf{r})$ of the density at this point as a homogeneous electron gas. Although LDA is a reasonable approach for the system with slowly varying densities throughout the space, it has been demonstrated that adding a local density gradient improves the computation in general. By accounting for density gradient dependences, the integrand in eq. 2.22 may be generalized to systems with higher inhomogeneous densities [82, 83]. This approach is known as the *generalized gradient approximation* (GGA):

$$E_{xc}^{GGA}(n) = \int n(\mathbf{r})\epsilon_{xc}^{GGA}(n(\mathbf{r}), \nabla n(\mathbf{r}))d\mathbf{r} \quad (2.23)$$

VASP

All the DFT calculations in this thesis were done using the *Vienna Ab initio Simulation Package* (VASP) code package [84, 85], which is based on projector augmented wave potentials [86]. VASP is a pseudopotential program, it provides a less accurate description of the solid electronic structure, including exchange

interaction and SOC, but it is significantly faster than the linearized augmented plane wave (LAPW) methods such as e.g. FLEUR [87] or WIEN2K [88].

Despite all of DFT's advantages and accomplishments, it is important to remember that it can only describe the undisturbed ground state of the system, which leads to an inaccurate description of effects such as self-interaction, excitation, and true many-body effects [89]. By definition, DFT is unable to accurately simulate excited states, leading to a continuous underestimating of band gaps in semiconductors and insulators. DFT, on the other hand, is very good for describing the band structure of selected layered TMDCs. The only issue with twisted TMDCs sample systems, such as WSe₂/graphene and bilayer WSe₂ studied in this thesis, is that they require large moiré unit cells, which necessitate a large number of atoms, as illustrated in fig. 2.5, and makes a computation expensive.

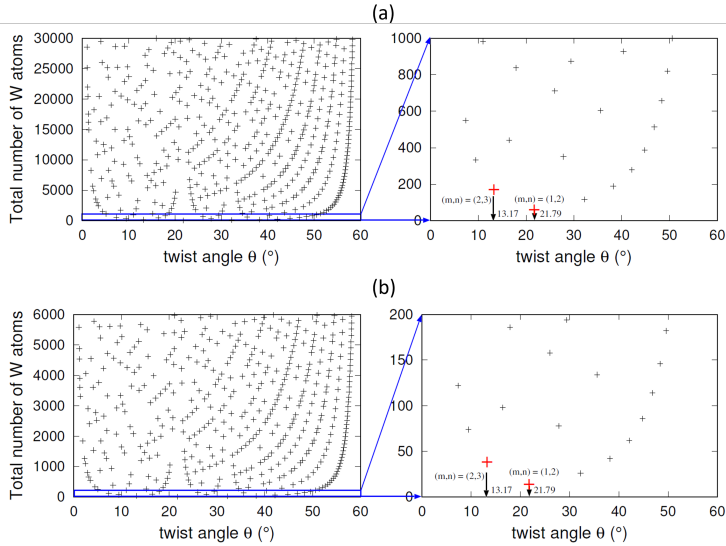


Figure 2.5: Total number of W atoms in Moiré superlattice for (a) twisted WSe₂ bilayers and (b) WSe₂ on graphene as a function of twist angle θ (in $^\circ$). The lattice structure of twisted bilayer system is not periodic in general as a function of twist angles as the periods of top and bottom layers are generally incommensurate with each layer. Hence, we restrict some special angles that two periods to be coincide resulting in a finite unit cell after rotation.

In this work, we are using the VASP code package, because it is a popular DFT tool for comparing and analyzing photoemission and ARPES data, as well as

investigating the initial band structure of the twisted TMDCs.

2.6 An introduction to layered materials

Layered materials have extended crystalline planar structures held together by strong covalently bonded atoms in-plane and weak out-of-plane Van der Waal's (vdW) interaction. Due to the weak vdW interaction, it is relatively easy to obtain the single layer of the vdW material with minimal damage to the remaining structure or the extracted layer. In 2004, A.K. Geim and K.S. Novoselov employed a simple scotch tape technique to produce an atomically thin layer of graphene [8].

Graphene exhibited intriguing properties with significant potential for future technologies [9, 10, 25]. It has received widespread attention in the scientific community during the last decades. However, its semi-metallic nature and zero bandgap characteristics limit its applicability in modern electronic applications. Although various attempts have been proposed to open the bandgap in graphene, such as chemical doping, nanoribbons, and double gating, they typically suffer from inadequate bandgap size or reduced carrier mobility [11–19, 90–92]. This has prompted the scientific community to pursue the discovery of technologically more relevant 2D layered semiconductor materials with potential applications in solid-state physics, materials science, and engineering [20, 21].

With their non-zero bandgaps, transition metal dichalcogenides that belong to the MX_2 family (where $\text{M} = \text{W}, \text{Mo}$ and $\text{X} = \text{S}, \text{Se}$) which has emerged as an important class of 2D materials that can overcome the bandgap challenge observed in graphene [22]. Despite the discovery of a single layer of MoS_2 in 1986 [93], little progress has been done in the field of low dimensional systems until the successful exfoliation of free-standing graphene in 2004. At that point the worldwide research efforts shifted to 2D materials [23] and additional materials, such as h-BN, black phosphorous (BP), and many others, have been discovered with a promise of a wide range of electrical properties.

Researchers investigate fascinating new physics and design new ultra-thin electronics by isolating 2D vdW materials or mixing and matching them to develop novel structures. Exfoliated samples are still used in most of the research on 2D layered materials. One disadvantage that limits potential applications of the exfoliated materials is the lack of scalability and reliability. Chemical vapor deposition (CVD) appears to be a viable alternative to mechanical exfoliation that enabled large scale production of monolayer thin films. CVD has

been widely accepted as a method to produce both vdW homo-structures and hetero-structures [27], which can be used in a variety of prototype devices such as transistors [94, 95] and solar cells [41, 96], thus expanding the usage of 2D materials in potential applications.

The study of low-dimensional TMDCs may have a dual benefit of addressing potential device applications, while also offering a platform for discovering new physical phenomena. For this reason, we have been encouraged to exfoliate and investigate one of the most popular TMDC materials, WSe₂, and its twisted homostructures on graphite that serves the purpose of the flat substrate. This section of the chapter will provide a brief overview of the fundamental properties of vdW materials, their homostructures, and motivation to select WSe₂ as a material of interest in this thesis work.

2.7 Transition metal dichalcogenides

TMDCs are vdW materials with the chemical formula, MX₂, where M denotes a transition metal and X stands for chalcogen elements [97]. Different TMDCs compounds constitute different stoichiometries and crystal structures. Therefore, depending on the combination of M and X, the resultant material can have a wide range of electronic characteristics, including semiconductivity, insulating qualities, and even superconductivity [20, 22, 98–100].

Monolayer TMDCs (X-M-X) are layered structures, which constitute of one M layer, sandwiched between two layers of X atoms as a unit layer. Transition metals and chalcogen atoms are bonded by strong covalent bonds within the triple layer. The bulk TMDCs are formed by vertically stacking these triple layers, with the chalcogen layer forming a weak vdW bond with the chalcogen layer of the subsequent triple layer. Furthermore, the coordination of transition metal atoms inside the TMDCs can be either trigonal prismatic or octahedral, resulting in various structural phases.

Polymorphism is a key characteristic of TMDCs as they are available in different polytypes. In their bulk counterparts TMDCs are generally available in three polytypes that are 1-trigonal (1T), 2-hexagonal (2H), and 3-rhombohedral (3R) in which the numbers represents the number of layers in the unit cell and the letter identifies the type of symmetry. These polytypes are common to MoS₂, WS₂, MoS₂, and WSe₂, sharing similar crystal symmetry, with WTe₂ being

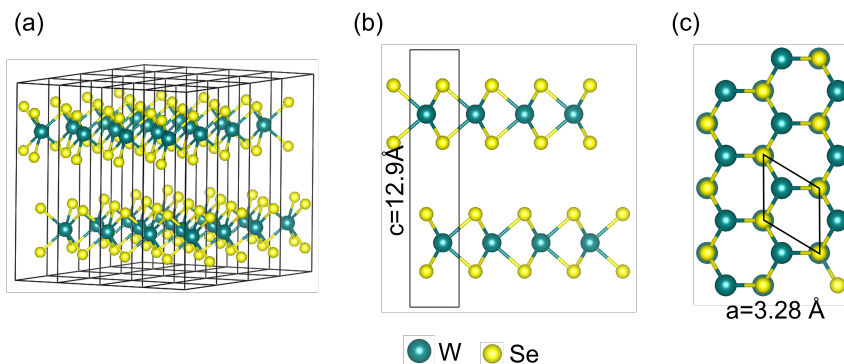


Figure 2.6: Crystal structure of 2H-WSe₂. Panel (a) shows the two monolayers of WSe₂ including the primitive unit cells. Panels (b & c) demonstrate side and top view of 2H-crystal symmetry showing out-of-plane and in-plane lattice constants. W atoms are depicted in green, while Se atoms are depicted in yellow.

an exception, as it is also recognised in a distorted 1T (Td) structure; also labelled as 1T' phase. The 2H and 3R phases are the characteristics of WSe₂ in which the 2H phase is thermodynamically stable. Typically, in such 2H-MX₂ polymorphs, the two layers of trigonal prismatic MX₂ unit cells are arranged in ABA stacking. In this scenario, the chalcogen atoms are situated at specific position referred to as “position A”. This position represents where the chalcogen atoms are located within distinct atomic planes and are aligned on top of each other in a direction perpendicular to the layer. Another frequently observed common phase is the 3R polymorph, which comprises three layers arranged in ABC stacking. Both, the 2H and 3R have a centre of inversion, which exhibit identical crystal symmetries; the only difference is the stacking order. As the property of the material depends on the crystal structure, each polytype of MX₂ exhibits varying electrical characteristics. For instance, while MoS₂, WSe₂ made up of the most stable 2H phase are semiconducting in nature [101], the WTe₂, MoTe₂ systems exhibit semimetallic characteristics [102,103]. Figure 2.6 illustrates the crystal structure of the 2H-WSe₂, which is the main focus of this study.

2.8 Atomically thin materials/ 2D TMDC

In the class of layered crystals, the weak vdW interaction between subsequent layers, as opposed to the strong covalent bonding within the layer, indicates that layers are not strongly coupled to one another in these crystals. This is important as minimum external forces are sufficient to separate these layers. Graphite is a well-known example of such vdW crystal structures. Upon exfoliation into a single atom layer of graphene, its electronic band structure shows a linear dispersion at K point, and the charge carriers can be described as massless Dirac fermions [104]. Similarly, TMDCs at atomically thin regime demonstrate new physical phenomena.

2.8.1 Crystal structure of a 2D monolayer

The monolayer limit of 3D TMDCs consists of a single unit layer described by MX_2 , in which a transition metal M is bonded to six nearest neighbor chalcogen X atoms in a trigonal prismatic coordination. Figure 2.7 shows the crystal structure of the monolayer: MX_2 (WSe_2).

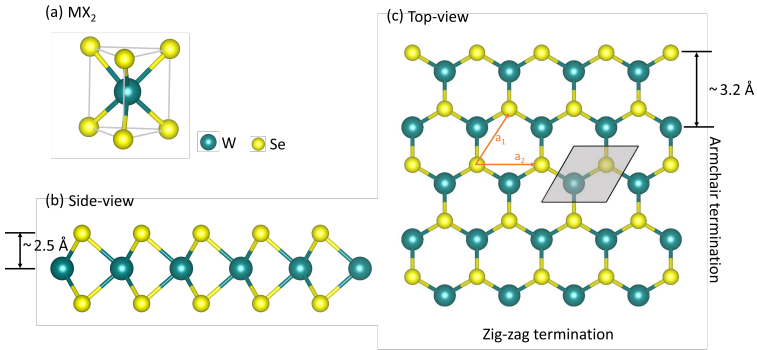


Figure 2.7: Crystal structure of TMDCs (WSe_2) monolayer. Panel (a) shows transition metal M atom (W) is trigonally prismatic coordinated with X atoms (Se). Panel (b,c) show the side and top views of crystal structure demonstrating the hexagonal structure with metal (green) and chalcogen (yellow) atoms. The gray shaded region is the primitive unit cell constructed using the two primitive lattice vectors a_1 , a_2 of magnitude a , which correspond to the lattice constant.

The real and reciprocal spaces of monolayer MX_2 are defined below. The real space lattice vectors, denoted by orange arrows in fig. 2.7(c), can be represented

as follows:

$$\mathbf{a}_1 = ax; \mathbf{a}_2 = a \left(\frac{1}{2}x + \frac{\sqrt{3}}{2}y \right) \quad (2.24)$$

The respective reciprocal lattice vectors have the form:

$$\mathbf{b}_1 = \frac{2\pi}{a} \left(x - \frac{1}{\sqrt{3}}y \right); \mathbf{b}_2 = \frac{2\pi}{a} \frac{2}{\sqrt{3}}y \quad (2.25)$$

In the case of 2H polymorphs, with a transition from bulk to monolayer, the symmetry reduces from $D_{6h} \rightarrow D_{3h}$ and the space group changes from $P6_3/mmc \rightarrow P\bar{6}m2$ [105]. Both bulk and monolayer have mirror plane symmetry inside the layer. More crucially, the inversion symmetry present in bulk is lost in the monolayer limit, resulting in a non-centrosymmetric material.

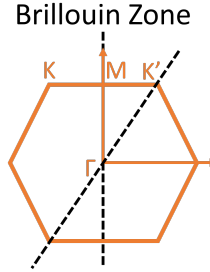
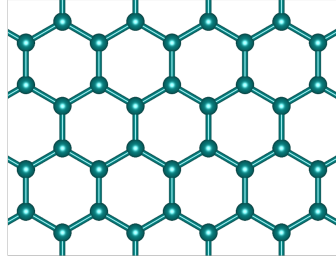
In the 2D monolayer lattice of WSe_2 , the two Se-atoms are equivalent since the center of the monolayer is a mirror plane. Graphene has 6-fold rotational symmetry. However, in WSe_2 , the rotational symmetry is reduced from 6-fold to 3-fold due to the different atomic basis. Figure 2.8 represents the comparison of the 2D lattice of graphene and monolayer WSe_2 in real and reciprocal space. In this case, the orange hexagon represents the first BZ in both lattices. The high symmetry point Γ lies at the center of the BZ, M labels the mid-points of sides, and K identifies vertices.

2.9 An introduction to vdW hetero-structures

As previously mentioned in section 2.8, one of the most notable characteristics of TMDCs and other vdW materials is their weak interlayer bonding. In comparison to non-vdW crystals [107], the saturation of all the covalent bonds renders the surface of vdW materials highly inert [108]. Therefore, graphite/graphene, TMDCs, and various other layered materials have no covalent interactions with the other materials at the interface. This makes vdW materials a potential alternative for manufacturing hetero-structures with minimal impact on the structural and chemical properties of individual component materials [109]. In comparison to traditional semiconductor hetero-structures, they have several benefits, including being lightweight, compatible with flexible substrates, while potentially exhibiting competitive performance [110].

Additionally, vdW hetero-structures are intriguing, because of their potential to combine distinct properties of various materials in a device that retains its 2D nature. They are built by stacking 2D materials on top of one another, and the vdW forces acting between the atomically thin films are strong enough to keep the stacks together. The strength of the interface interaction is influenced by the alignment (or misalignment) of the crystallographic axes of one layer with another. The possibility of forming various stackings of 2D atomic lattices with different orientations and interface interaction strength provides tunable physical properties. Combining different crystal lattices also means merging the properties and formation of new artificial materials by a sequential transfer.

(a) Graphene-lattice



(b) Monolayer-WSe₂-lattice

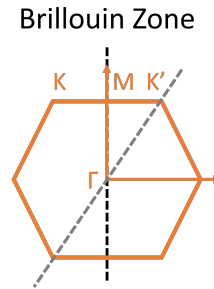
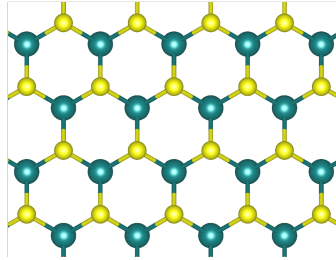


Figure 2.8: Comparison of graphene and monolayer WSe₂ like lattices and Brillouin zones. In (a) all 6 K -points are equivalent due to the presence of the inversion symmetry, represented by green-colored C-atoms. Within the BZ, the ΓM and $\Gamma K'$ lines (depicted by dashed black lines) act as mirror planes. In (b) WSe₂ lattice has a two-atom basis, with green and yellow balls representing the atoms. In the BZ, the mirror symmetry along $\Gamma K'$ (dashed gray line) is broken and the SOC divides the BZ corners into non equivalent K/K' points allowing for spin-polarized bands [106].

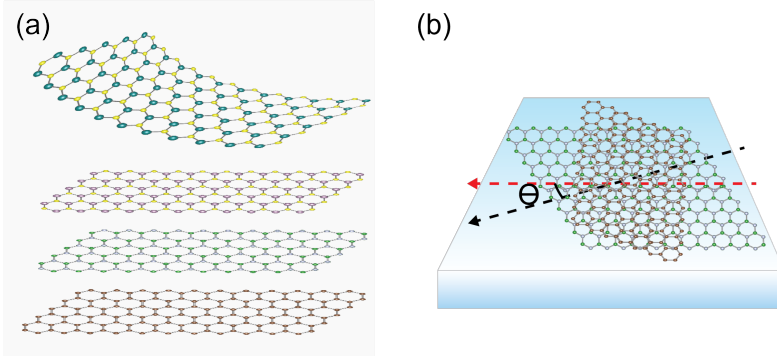


Figure 2.9: Panel (a) shows schematic illustration of the vertical vdW heterostructures. Different types of atomic layers are stacked on the top of each other. Panel (b) shows that one atomic lattice is rotated with angle θ with respect to the other.

The basis of such a hetero-structure creation is comparable to a “Lego” construction, in which each atomic layer serves as a Lego block shown in fig. 2.9(a). Figure 2.9(b) shows the 2D lattices of vdW materials having a relative rotation (θ) between them, which induces the moiré pattern. The moiré potential together with interlayer coupling leads to the band modulation and yields rich novel phenomena, e.g., superconductivity at magic twist angles in graphene [111].

One of two ways can be used to create vdW hetero-structures. The first involves constructing different layers in a plane to create lateral hetero-structures, whereas the second involves layer-by-layer vertical stacking of different layered materials. The preparation of hetero-structures is shown schematically in fig. 2.10, with TMDC lattices as an example. In a standard synthesis procedure, one layer of a 2D material is typically applied to the substrates first (see fig. 2.10(a)). The most critical stage is adding/transferring another layered material on top of the first layer, either by traditional epitaxial methods [112, 113] or through a dry transfer approach (see fig. 2.10(b)). When the two layers are linked in-plane, lateral hetero-structures form (see fig. 2.10(c)), and when one layer is stacked on top of another, vertical hetero-structures are formed (see fig. 2.10(d)).

Hetero-structures made by combining different 2D materials have gained widespread attention due to their unique properties. Some examples of such 2D material based hetero-structure realized devices are $\text{WS}_2/\text{MoSe}_2$ hetero-structures for

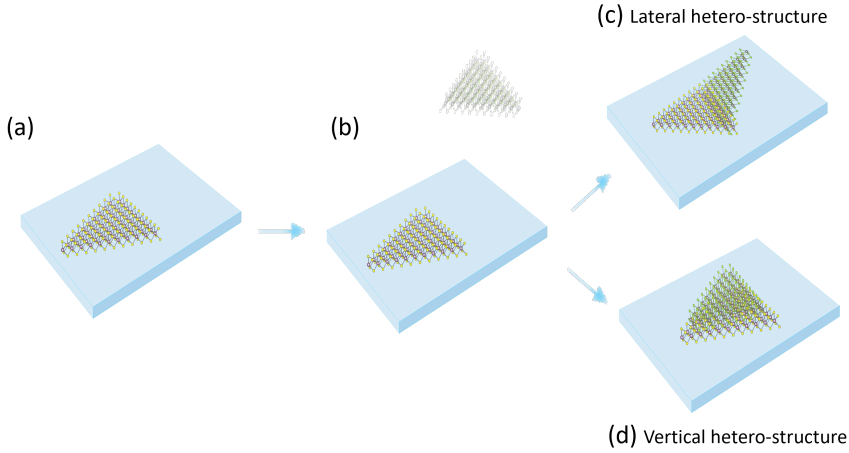


Figure 2.10: Schematic depiction of the fabrication of the lateral and vertical hetero-structures. Panel (a) shows the first TMDC layer on the substrate. Panel (b) represents the assembly of the second TMDCs layer with the first one. Panel (c) and Panel (d) represent lateral- and vertical- vdW hetero-structures, respectively.

multi-functional optoelectronic device [114, 115], MoS₂/WS₂/Graphene hetero-structures for ultra-fast and high-performance photodetectors [116, 117], MoS₂/-WS₂ hetero-structures for spintronic devices, such as spin valves and magnetic tunnel junctions [118, 119] and so on. Moreover, the researchers also demonstrated the fabrication of a vertical p-n junction thin field effect transistor based on n-MoS₂/p-WSe₂ [120] and photodetectors based on PtS₂/PtSe₂ [121, 122]. These examples highlight the diverse potential applications of 2D material-based hetero-structures and the growing interest in their development.

2.10 Electronic bandstructure of 2D materials

The electronic bandstructure of TMDCs can significantly change when the material is thinned down to a monolayer. Several research groups have established the indirect-to-direct bandgap transition in TMDCs theoretically [123–127] and experimentally [128, 129]. As an example, fig. 2.11 shows the calculated band structures of MoS₂ of various thicknesses using density functional theory. As can be observed in fig. 2.11(a,b), for bulk and bilayer, the VBM is positioned at the Γ point of the SBZ and the conduction band minimum (CBM) is in between the Γ and K points due to the interaction of S p_z and Mo d_z^2 atomic orbitals

[97,123,128,129,131], which results in an indirect bandgap. By contrast, in the case of monolayer MoS₂, CBM and VBM are present at the K points of the SBZ (see fig. 2.11(c)) resulting in a direct bandgap. This is owing to the fact that reducing the number of layers results in a decrease of quantum well states, which is seen at the Γ point. In a bilayer or multi-layer cases, it can be interpreted in terms of bonding and antibonding interaction between out-of-plane orbitals, but it is absent in monolayers. The emergence of the direct bandgap at the K point has an impact on the physical characteristics of monolayer TMDCs. Other TMDCs such as MoSe₂, WS₂ and WSe₂ show similar bandstructure characteristics. The analysis of the electronic band structure of twisted SL and

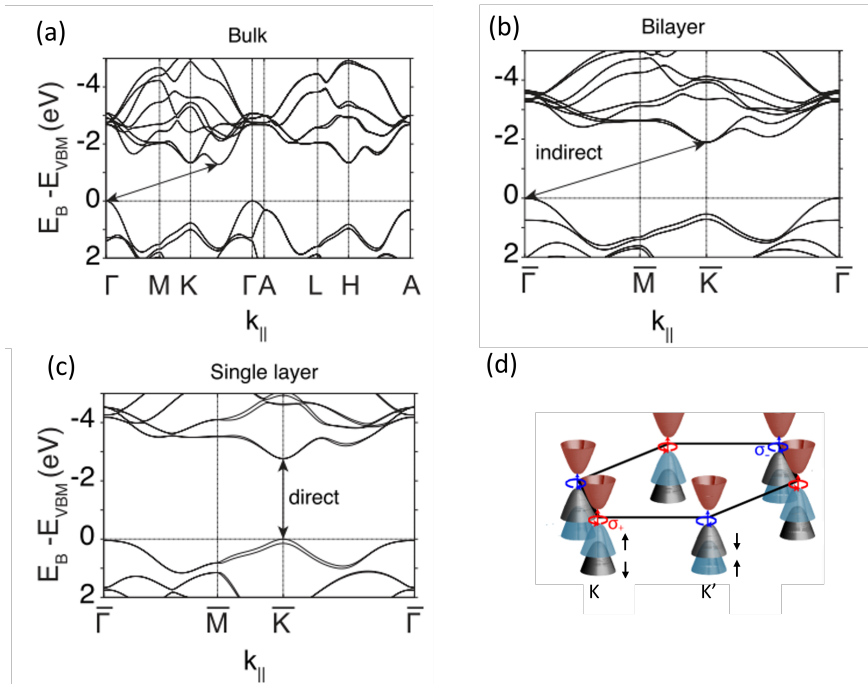


Figure 2.11: DFT calculated electronic band structures of MoS₂ in (a) bulk, (b) bilayer and (c) monolayer form at high symmetry points. The direct and indirect band gaps are indicated by the black arrows in each figure. The valence band maximum (VBM) is set to 0 eV. (d) Sketch of the band structure of 2H-MoS₂, showing the spin-orbit splitting of the valence bands edges at the K and K' points at the corners of the Brillouin zone. Blue and black cones represent spin-up and spin-down, while red and blue arrow indicate valley optical selection rules respectively. Adapted from [39, 123, 130].

twisted BL WSe₂ with graphite lattice is the central focus of chapter 5. These sample structures contain different twist between the SL WSe₂ and graphite as well as between the top and bottom layer of WSe₂. In all the different cases shown in fig. 2.11, the spin-orbit splitting in the vicinity of the K/K' points in the valence band is nearly the same. Spin splitting occurs in monolayers of TMDCs materials due to lack of inversion symmetry and SOC. It also remains in the bulk, because the in-plane orbitals of K -points in subsequent layers do not interact substantially.

Figure 2.11(d) demonstrates the electronic band structure of monolayer MoS₂. It shows the spin splitting of the valence bands at K and K' points at the corners of the Brillouin zone driven by spin-orbit interaction. Since MoS₂ is non-magnetic, time-reversal symmetry applies and the energy for K and K' must be degenerate through $E(\uparrow, \mathbf{k})=E(\downarrow, -\mathbf{k})$. Time-reversal symmetry is also acting on the orbital angular momentum (OAM), therefore, K and K' have opposite OAM. For this reason, it is possible to excite electrons into a certain valley (either the K or K' locations) with a specific spin using opposite helicities of circularly polarised light [132]. The spin splitting of bands at K and K' is opposite due to time-reversal symmetry. The schematic of the valley dependent excitation of electrons with spin-up and spin-down polarization by left (σ_-) and, right (σ_+) circularly polarized light is shown in fig. 2.11(d).

It is important to note that the underlying physics of WSe₂, both in its bulk and monolayer form, is similar to other transition metal dichalcogenides (TMDCs) such as MoS₂, WS₂ and MoSe₂. The key difference between these compounds is the magnitude of their SOC, which causes the splitting of the energy levels between the spin-up and spin-down states. For instance, the spin-split energy difference of the VBM at the K point in WSe₂ is about 500 meV [133], whereas it is ~ 148 meV, ~ 180 meV, and ~ 425 meV in MoSe₂ [134], MoS₂ [135], and WS₂ [136], respectively, owing to the larger SOC in WSe₂. This has significant consequences for transport and optoelectronic properties, such as the generation and manipulation of spin-polarized carriers. Since the dispersion of electrons at the VBM has a significant impact on transport properties, it is intriguing to study the band dispersion around the VBM. This makes WSe₂ a promising candidate for spintronics applications in the future, due to its larger spin splitting [105]. In addition to their unique electronic properties, these materials also exhibit

excellent mechanical properties including high stiffness, strength, and flexibility [137, 138]. This makes them ideal for applications in flexible electronics, sensors, and nanoelectromechanical systems [129, 139–141]. Furthermore, their high optical absorption and emission properties, combined with their thinness, make them promising candidates for optoelectronic applications, such as photodetectors, solar cells, and light-emitting diodes [43, 44, 116, 142–144]. The bandgaps of these materials fall in the visible range, making them suitable for these applications. Overall, the unique properties of these semiconducting 2D materials make them promising candidates for a wide range of applications [145–147]. The large SOC, combined with their other desirable properties, make them attractive for exploring novel electronic and photonic phenomena, and for the development of next-generation electronic devices [148].

Chapter 3

Sample Preparation and Characterization

3.1 Sample fabrication methods

Following the discovery of graphene in 2004, there has been a significant increase in interest in the fundamental science and applications of two-dimensional materials, as well as their homo/hetero structural configurations [8]. Layered 2D materials exhibit intriguing characteristics when thinned down to a single or few layers, as discussed in previous chapters.

Rapid development of devices based on two-dimensional materials has depended largely on mechanical exfoliation of bulk crystals using scotch tape and subsequent transfer to substrates. Over the last decade, this basic method has been improved to increase the production and lateral size of exfoliated flakes. The main techniques employed in this study are mechanical exfoliation and peel/lift transfer. A comprehensive explanation of these techniques is presented in the following sections.

3.1.1 Mechanical exfoliation

The development of the micromechanical exfoliation (the so-called scotch tape method) technique was a crucial advantage in the success of graphene research. Due to its simplicity and the fact that it avails high quality 2D materials, the micromechanical exfoliation is continued to be primary choice of technique among researchers to procure 2D materials of known thicknesses. This process is quite straightforward, as illustrated in fig. 3.1 [149]. The first step is to press the adhesive tape on the desired crystal surface (a), then peel it off; during this process, some of the top layers of the crystal are attached to the tape (b), and then

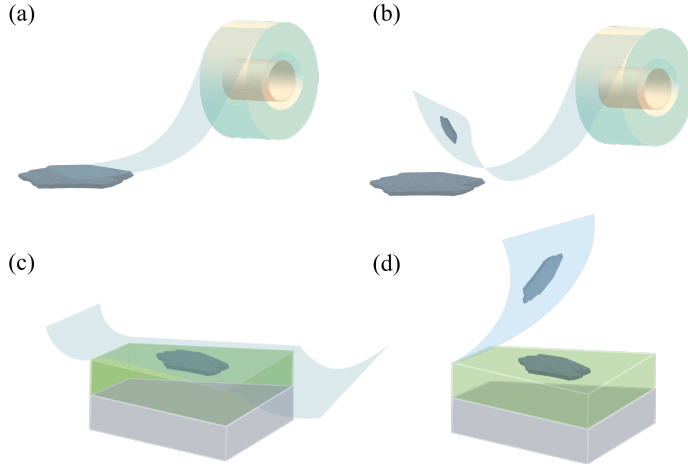


Figure 3.1: Schematics of micromechanical exfoliation of a layered material: (a) Adhesive tape is pressed onto the specified crystal. (b) Peel off the sticky tape, allowing the top layers of the crystal to adhere to the tape. (c) The tape was then placed onto the desired substrate, such as Si, TiO_2 , and so on. (d) Keep on repeating the same process in order to get the single layers of the layered materials. Reproduced from [149].

press it on the targeted substrate (c). Typically, this technique must be done multiple times to yield monolayers (d). The exfoliation method produces flakes of varying sizes and thicknesses that are randomly scattered on the substrate surface. Only a small percentage of all these flakes are atomically thin.

This technique produces the cleanest and finest quality samples as compared to polyvinyl alcohol (PVA), wedge, and eulcrite transfer methods, making it an excellent choice for investigating new physics and novel device designs [150–152]. A subsequent issue following the exfoliation process of the atomically thin flake is to locate them, which usually is accomplished using optical identification [153–155]. This is a quick, non-destructive and reliable technique to locate 2D flakes of interest.

Due to the low thickness, 2D material flakes, particularly TMDC flakes, are sometimes invisible under the optical microscope; however, this issue can be handled by utilizing a suitable thickness of SiO_2 on Si [156–158]. For example, MoS_2 monolayers can be detected more easily if the thickness of SiO_2 is 55 or 220 nm, providing an optical contrast of 60% for 500 nm wavelength illumination [159]. Previous studies showed that the contrast of the atomically thin films

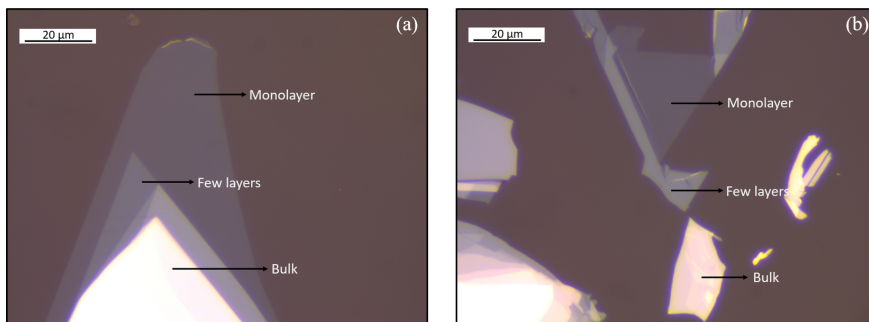


Figure 3.2: (a) and (b) show the optical micrographs of the mechanically exfoliated WSe₂ flakes surrounded by thicker bulky flakes. Different thickness of the flakes is shown by the varying optical contrast.

depends on the TMDC's layer thickness. Figure 3.2 shows optical images of a WSe₂ single layer surrounded by thicker flakes on Si substrate. The varying optical contrast from flake to flake is clearly visible which is helpful to differentiate flakes with different layer thickness.

3.1.2 Dry transfer technique

Fabrication of sterile homo/hetero 2D layered structures is a critical step in the device fabrication as unclean or non-uniform 2D structures tends to impact device performances. Over the years, many conventional techniques have been used, such as wedging, PVA, and evalcite transfer methods [150–152]. All of these methods rely on the presence of an organic entity, most commonly a polymer component. At the end of the transfer process, such polymer components act as sacrificial materials in different solvents. As the wet chemical steps are used throughout the fabrication process, eventually leaving behind an unwanted organic entity such as long-chain molecules on 2D material surfaces even after the exhaustive rinsing with different solvents. The presence of such undesired products likely interfere with device functioning, therefore affecting its overall performance. A dry transfer technique can be employed as an alternative that can overcome the issue of contamination. These transfer techniques rely on a visco-elastic stamp [161]. The stamp is made of commercially available visco-elastic material (Gelfilm from Gelpak). It is a thin layer that is attached to a glass slide to make it easier to handle [160].

Figure 3.3 shows the schematics of the dry transfer setup and steps required

to prepare the stack of atomically thin layers [160]. Panel (a) depicts the experimental setup for transferring two-dimensional crystals, including an optical microscope equipped with long working distance optical objectives and a three-axis micrometer stage for precisely positioning the stamp. Panels (b-g) show the steps to prepare the visco-elastic stamp and assembly of the atomically thin layers on the top of each other. First, a bulk crystal is thinned down by using blue/scotch tape. The flakes are then transferred on the stamp using the micromechanical exfoliation process (b). Next, the surface of the stamp is examined under an optical microscope to determine the atomically thin layer and then turned upside down (c). Once the thin layer is identified, the targeted substrate is positioned on the sample XYZ stage using double-sided tape, and the transparent polymer stamp is attached upside down on the top of the targeted substrate (d). After aligning the flake and the desired position on the substrate,

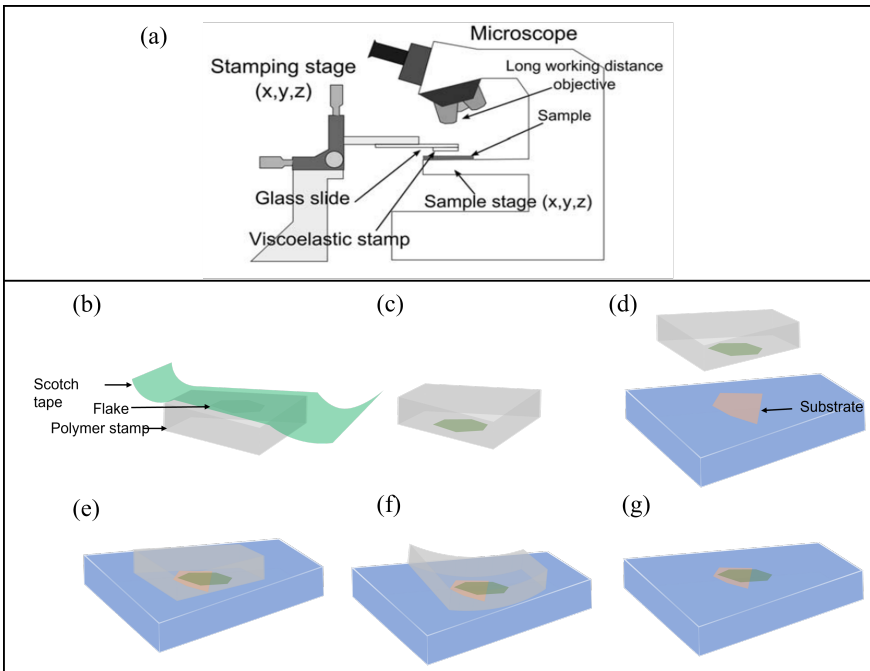


Figure 3.3: Deterministic dry transfer setup and process: (a) The experimental setup for the all-dry transfer technique is depicted schematically. The procedure involved in the preparation of the visco-elastic stamp and the deterministic transfer of an atomically thin flake to a user-defined location are depicted in (b-g). Reproduced from [160].

the stamp is pressed against it (e). Afterward, it is very slowly peeled off (f). The atomically thin layer is now transferred on the surface of the targeted substrate at a predetermined position (g).

3.2 Fabrication of 2D hetero-structures

In this thesis, multiple 2D hetero-structures with different twist angles between the monolayers of TMDCs were fabricated and studied, for example: MoS₂/WSe₂/n-Si, MoS₂/MoS₂/graphite/n-Si, WSe₂/WSe₂/graphite/n-Si, MoSe₂/MoSe₂/graphite/n-Si etc. In this section, I'll show one example of the fabrication process for 2D vertical van der Waals structures. Figure 3.4 shows the sequential transfer process used for the fabrication of multiple hetero-structures.

Firstly, highly-oriented pyrolytic graphite (HOPG) was carefully exfoliated on a n-doped Si substrate by the scotch tape method to obtain flakes with a thickness ranging from 10-40 nm, as shown in fig. 3.4(a). The graphite flakes serve the purpose of a flat substrate for the bilayer sample structures. Before the transfer, the substrate (n-Si) must also be properly prepared in order to ease the transfer of crystals from the tape. Typically O₂ plasma and heat treatment are applied to improve the adhesion between the atomically thin layer and the targeted substrate. In addition, n-doped Si substrates are ultrasonically cleaned in specific solvents such as isopropanol, acetone, and ionized water for 15 minutes intervals in each solvent and then dried with a nitrogen gun.

The bulk layered WSe₂ crystal was exfoliated with scotch tape to obtain atomically thin flakes. Exfoliation of TMDCs onto poly-methylmethacrylate (PMMA), polydimethylsiloxane (PDMS), or polypropylene carbonate (PPC) has a higher success rate than exfoliation onto SiO₂. Therefore, 2D WSe₂ flakes were transferred onto the PDMS stamp, which was adhered to the glass slide to ease its handling for further processing. The transparent stamp helps us to identify the optimal thickness of WSe₂ flakes using a transmission mode under the optical microscope.

Once we identified the single layer of WSe₂ on the PDMS stamp positioned on the surface of the glass slide, we attached the glass slide on the three-axis manipulator facing upside down and heated the desired substrate (n-doped silicon) up to 75-100°C, facilitating the transfer process. Next, the exfoliated thick graphite

flake on the n-doped Si substrate is mounted on the XYZ stage using double-sided tape. By carefully aligning the transparent PDMS stamp, the WSe_2 flakes are then transferred with a sub-micrometer resolution to a desired location on the thick graphite flake fig. 3.4(b). We repeated the same process for transferring the second monolayer of WSe_2 on the top of the WSe_2 /graphite/Si single layer system. This way we obtained a bilayer structure: WSe_2 / WSe_2 /graphite/n-Si fig. 3.4(c). With this process, we prepared bilayer samples with different twist angles between the monolayers of WSe_2 . In our 2D sample preparation, we used two methods: mechanical exfoliation and dry transfer technique. When employing the dry transfer methodology, one can reach a yield of 100% when

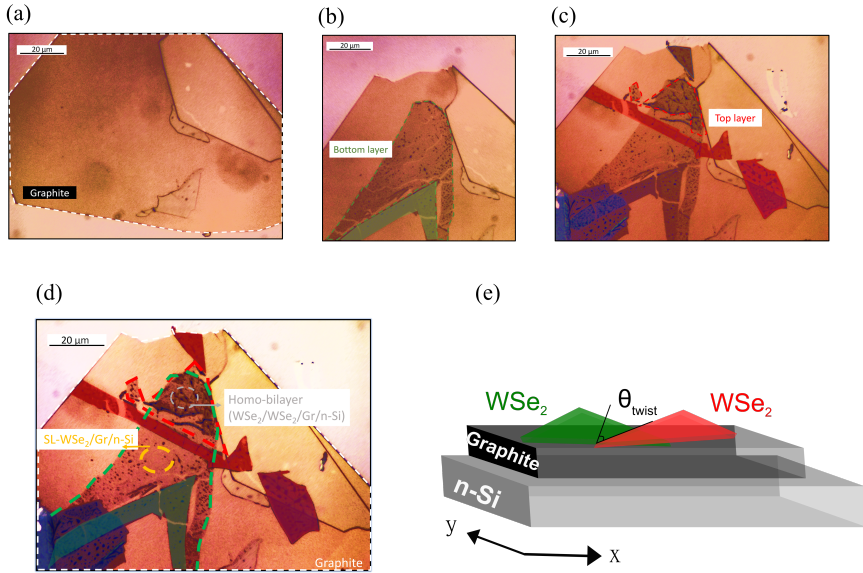


Figure 3.4: Sequential transfer of homo-bilayer of WSe_2 flakes: (a) Optical image of a mechanically exfoliated graphite flake on an n-Si substrate. (b) Optical image of the same flake following the transfer of a single layer of WSe_2 flake that is referred to as the bottom layer. (c) Another single layer of WSe_2 is transferred onto the stack by employing another transfer step. The top and bottom monolayers of WSe_2 are shown by the red and green dotted lines. (d) Optical image of the twisted SL and BL WSe_2 /graphite/n-Si. This structure exhibits two type of twist angles: between the graphite and SL WSe_2 , which are represented by the yellow and gray dashed circles, respectively. (e) Schematic model of the sample configuration. Different nanosheets are denoted by green, red, and black colors.

transferring the sample on an atomically flat material, but the yield is reduced on rougher substrates due to less adhesion between the 2D material and the targeted substrate. Moreover, it significantly reduces contamination during the sample preparation.

3.3 Strain induced bubbles

The topography of the transferred flake is characterized with the help of the atomic force microscopy (AFM) technique. Prior to the AFM measurements, the 2D vertical heterostructure is annealed at 300°C in ultra-high vacuum (UHV) for 30 minutes. The annealing temperature and time are optimized to achieve the self-cleaning effect; a partially understood diffusion process takes place in the interfaces where contaminations segregate and form large pockets, leaving seemingly clean areas of a few micrometers in between. These pockets are also called “bubbles” and they can be easily detected in AFM measurements [162,163].

Figure 3.5 shows the AFM image of a WSe_2 flake transferred onto the Si substrate (panel (a)) and thick graphite flake (panel (b)). As seen in fig. 3.5(a), a number of bubbles is uniformly scattered throughout the silicon substrate surface. This might be owing to the roughness of the SiO_2 underneath or to the localized accumulation of a previously dispersed surface contamination, such

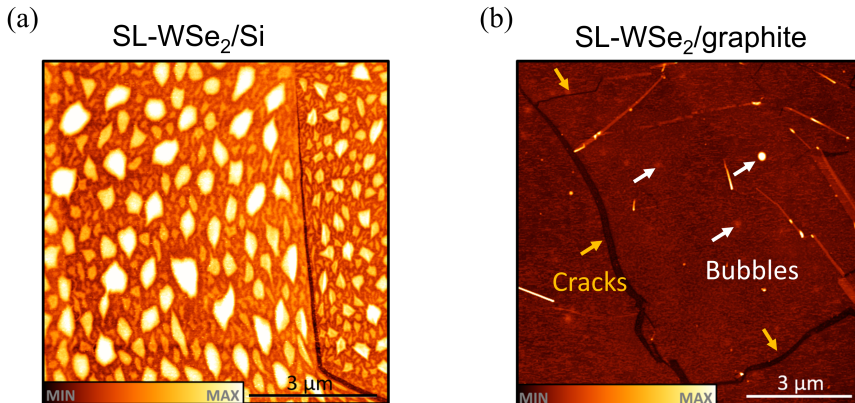


Figure 3.5: 2D TMDCs flake on different substrates: AFM images of WSe_2 monolayer on silicon (a), and graphite (b) substrate. The contamination are aggregates in form of bubbles due to self-cleaning effect between graphite and TMDCs interface. Bubbles and cracks are depicted by white and yellow arrows.

as tape residues. Figure 3.5(b) shows that the surface area of the WSe_2 flake placed on graphite flake is also covered with bubbles and wrinkles. However, we observed that the density of bubbles is reduced as compared to Si substrate.

The bubbles are seen as white spots in the AFM images, which are measured on SL WSe_2 /graphite, and BL WSe_2 /graphite, and the corresponding dark areas on the optical image (see figs. 3.6(a,d,g)). We observed that approximately 30–40% of the produced hetero-structures have substantial areas free of bubbles and wrinkles. This is the result of the self-cleaning effect between the graphite and TMDCs interface [162, 163]. Additionally, AFM measurements on the SL WSe_2 and the graphite flake are also shown in panel 3.6(b,c), with the step height matching the thickness of one monolayer of WSe_2 .

In the homo/hetero-structures, the vdW forces operating between the 2D material and substrate seal the interface and aggregate interfacial contamination

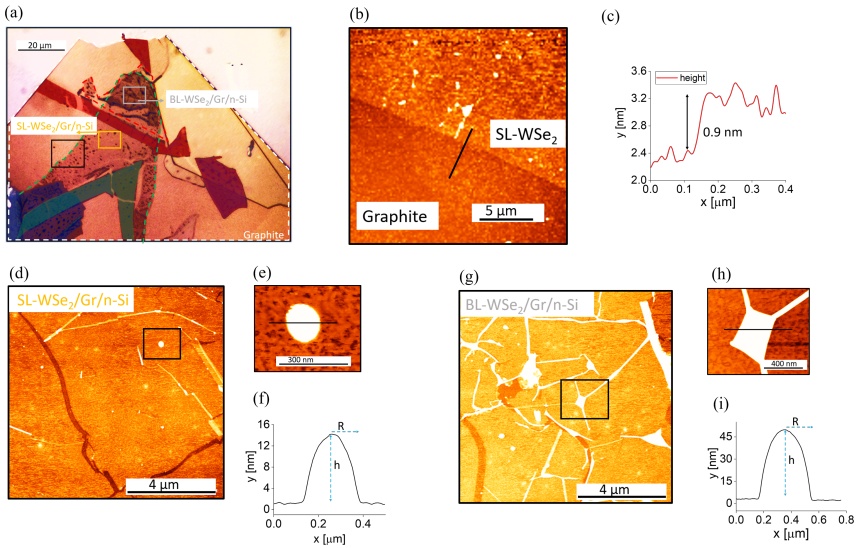


Figure 3.6: Bubbles trapped between 2D TMDCs (WSe_2) flake and graphite: (a) Optical micrograph of the SL WSe_2 and BL WSe_2 flake lying on the thick graphite flake (fig. 3.4). (b,c) show the AFM image and height profile measured on the edge of the monolayer flake of WSe_2 /graphite as indicated by black square in (a). The AFM images measured at the SL WSe_2 and BL WSe_2 parts of the sample structure are shown in (d,g). (e,h) are AFM images of the bubbles created by WSe_2 flake, which are shown by black squares in (d,g), and (f,i) show the bubble's cross sectional profile. Black line in (e,h) indicates where the profiles in (f,i) were measured.

into the bubbles. The interface acts as an entrapment site to foreign aggregates or contaminants, which are observed in the form of bubbles [164]. The contents of these bubbles are likely to be water and hydrocarbons [165]. A thermal annealing step further aggravates the diffusion of these contaminants to collate into bigger air pockets leaving the surrounding region bubble-free, as shown in figs. 3.5 and 3.6. The sterility of this bubble-free region at the interface remains largely debated. For instance, while few studies have reported the formation of larger bubble leaves the rest of interface clean and contaminant free [166], others have demonstrated a possible coexistence of a thin fluid layer along with bubbles at the interface [167–170]. For both cases presented in fig. 3.5 (SL WSe₂/n-Si and SL WSe₂/graphite), the flat areas have a root mean square (RMS) surface roughness of < 0.1 nm, which is limited by the accuracy of our AFM.

We notice only few bubbles at the interface between the monolayer of WSe₂ and graphite (fig. 3.6(d)), although there is a big crack present. In contrast, the surface of the bilayer of WSe₂ (fig. 3.6(g)) contains numerous cracks, bubbles, and wrinkles. Panels 3.6(e,h) are the zoomed-in AFM images of typical bubbles and 3.6(f,i) are the cross-sectional height profiles.

Bubbles and irregularities come in various shapes such as round, elongated, triangular, pyramidal, etc. The radius of well-defined round and elongated bubbles varies from $0.15 \mu\text{m}$ to $1 \mu\text{m}$, and the height profile changes from 5 nm to 250 nm on the different surface regions of the WSe₂ flakes.

Chapter 4

Experimental Setup

4.1 Nano-ARPES beamlines

During the last few decades, the conventional ARPES experiments at synchrotron facilities and homelab-based light sources have utilized beam spot sizes of $\sim 15\text{-}500\ \mu\text{m}$. As a result, ARPES experiments were unable to probe a large number of engineered materials fabricated at smaller length scales ($<10\ \mu\text{m}$) [158, 171]. Recently, several technologically important materials have been fabricated at micron to nanoscale dimensions, such as the twisted bilayer graphene [16, 31]. It is quite challenging to realize these materials at larger length scales without fractures or contaminants trapped between the layers. Further, many single-crystal materials require surface cleaving prior to the ARPES experiments. Cleaving does not necessarily result in large flat areas; the flat cleaved surfaces might have varying crystal orientations. Therefore, an ARPES set up with a smaller beam spot in the range of $\sim 1\text{-}5\ \mu\text{m}$ is required.

In general, there are two approaches available for probing the interplay between geometrical and electronic structure in various sample geometries: “Momentum microscopy”, and “nano-ARPES” techniques. For example, the NanoESCA beamline at Elettra, Italy [172, 173] is equipped with a commercially available momentum microscope capable of obtaining spatially-resolved information about the band structure. However, the availability of the beam spot size is in the range of $10\text{-}20\ \mu\text{m}$, and by using field aperture, it can be further improve to $8\text{-}10\ \mu\text{m}$. Despite this improvement, it is still challenging to measure small-scale samples, which are typically less than $8\ \mu\text{m}$ in size.

To address this challenge, μ -ARPES and nano-ARPES techniques with $\sim 1\text{-}5\ \mu\text{m}$ or smaller beam spot integrated with scanning microscopy have been developed to identify and measure small-scale samples. However, there are some issues when creating a photon beam spot of $1\ \mu\text{m}$ or smaller. For instance, the

focusing optics requirement may limit the available photon angle of incidence onto the sample and affect the extraction of the excited photoelectrons. The focusing optics must be in close proximity to the sample surface to focus the vacuum ultraviolet (VUV) or X-ray beam from the beamline within hundreds of nanometers. On top, a larger focusing optics is required to obtain a larger numerical aperture. These criteria can be in conflict with the ARPES detector requirement, which needs a wide solid angle to sample a large momentum space. Advanced setups of the ANTARES beamline at SOLEIL synchrotron and the MAESTRO beamline at the Advanced Light Source (ALS) synchrotron offer the advantages of combining a small beam spot, in the range down to hundreds of nm, with spectroscopic imaging. Another feature of these beamlines is their ability to excite electrons from the valence band or core levels using a wide photon energy range. This provides the opportunity to determine precisely different elemental compositions on the sample surface. Further, they also offer controlled polarization of the light.

In this thesis, the majority of the experiments were carried out at μ -ARPES and nano-ARPES beamlines. This chapter will provide an overview of different experimental setups used in our ARPES studies. Such ARPES experiments are complex setups that require an UHV environment with pressure preferably of the order of 10^{-10} mbar or better. UHV systems need significant maintenance, which comprises constantly running pumps such as turbomolecular pumps, ion getter pumps, and titanium sublimation pumps. Sometimes, whenever the vacuum chamber was vented or polluted, the entire system requires baking at least at 120°C . At synchrotron facilities, the storage ring, entire beamline, and the experimental end-station have a transfer path that connects all the chambers by a UHV system. In events of leaks, venting has to be avoided, which is guaranteed by multiple safety interlock systems. The UHV system complicates an access to any manipulation within the chamber; therefore, bellows and magnetic couplings or piezo-actuators can be used, allowing external manipulation and precise sample movements. This implies that every component and approach used in the ARPES experiment is crucial for precise sample measurements, which is elaborated further in this chapter.

Since ARPES is a surface-sensitive technique, the quality of the sample surface is critical for the experiments. In order to produce a clean surface for ARPES experiments, the majority of samples are prepared in-situ. Therefore, all ARPES

setups utilized in this study feature customized preparation chambers that are directly connected to the photoemission experiments. These preparation chambers are capable of performing typical UHV surface preparation procedures such as heating for sample degassing, argon sputtering, and in-situ growth of thin films. An alternative method for producing a clean sample surface is cleaving a single crystal. To characterize the sample surface, the preparation chambers also include the equipment to perform LEED and Auger electron spectroscopy (AES).

4.2 ANTARES beamline at SOLEIL

The beamline

The ANTARES (Analysis Nano-spoT Angle Resolved photo Emission Spectroscopy) beamline is located at the SOLEIL synchrotron in France [174]. The storage ring operates in “Top-up” mode, which means a small amount of current is injected periodically to maintain a constant beam current in the ring; here, it’s 500 mA at 2.75 GeV electron energy. The beamline employs a tandem configuration of two undulators to produce a soft X-ray beam with controlled linear and circular polarization in the energy range from ~ 12 eV up to 1000 eV. The nano-ARPES setup at the ANTARES beamline shares the classical design of the ARPES experiments. The schematic of the beamline is represented in fig. 4.1.

The beamline consists of the following main components to provide a collimated and homogeneous beam spot: pre-focusing mirrors, a plane-grating monochromator (PGM), and post-focusing optics. The nano-ARPES end-station is equipped

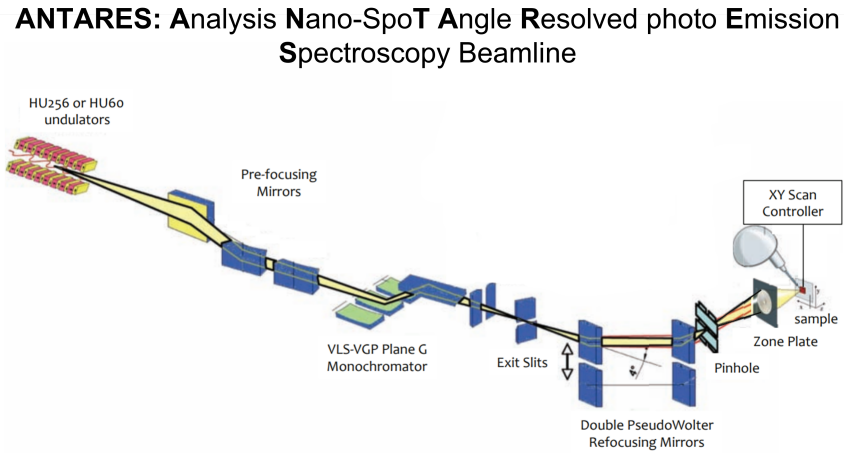


Figure 4.1: Schematic depiction of the ANTARES beamline. The first pre-focusing mirrors collimate the undulator beam to a plane-grating monochromator with two gratings that can be exchanged by remote control. The PGM is positioned to suppress higher orders of light with high resolving power. The second set of mirrors is used to refocus the beam on the sample or the pinhole, depending on whether a micro- or nanometer spot size is required. Reprinted with permission from J. Avila, from [175].

with a Fresnel zone plates (FZPs) focusing scheme together with an order sorting aperture (OSA) mounted between the FZP and the sample in order to suppress unwanted diffraction orders. The details of calibration of the beamline can be found in [174].

The ANTARES end-station includes a scanning microscope that produces an image one pixel at a time by raster scanning the X-ray beam across the sample surface and at each point a spectrum has been taken with the MBS A-1 spectrometer with high angular and energy resolution, and with the deflector lens and by selecting certain electrons from each point one can generate an image.

The experimental end-station

The experimental end-station of the ANTARES beamline is designed with a fast entry chamber for transferring samples quickly from ambient to UHV environments, a preparation chamber, and an analysis chamber equipped with a microscope, electron analyzer, and nano-spot focusing optics. In comparison to

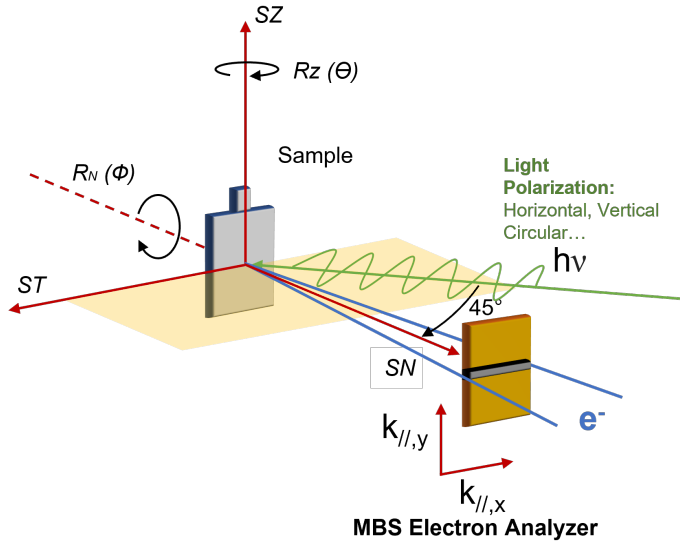


Figure 4.2: Illustration of the experimental geometry of the ARPES setup at the ANTARES beamline. The angular distribution along the horizontal entrance slit is imaged by the analyzer. 2D k-space mapping is achieved by rotating the sample around the vertical manipulator axis. The incidence direction of the X-ray radiation is indicated by green color.

the conventional ARPES setups, the specimens at this beamline are mounted on a high-precision sample plate, which will ensure their nanoscale alignment in the x, y, and z directions. The ANTARES beamline is equipped with two sets of motors: mechanical motors with a larger movement range with a resolution of $\sim 5 \mu\text{m}$ and piezoelectric motors with a smaller movement range with a resolution of $\sim 5 \text{ nm}$. An interferometric control can be used to reduce both thermal drift and mechanical movements in order to ensure accurate nanometer scanning of the sample [176]. Furthermore, the azimuthal (Ψ) and polar (Θ) angles can be automatically scanned over a total range of 210° and $55\text{-}60^\circ$, respectively. The beamline parameters are summarized in table 4.1.

	With zone plates	Without zone plates
Energy Range	45-1000 eV	12-1000 eV
Beamspace on the sample	400 nm @ 100eV	80 μm @ 100 eV
Polarization	Linear horizontal and vertical, elliptical	Linear horizontal and vertical, elliptical
Energy resolution	25-30 meV @ 100eV	15 meV @ 100eV
Min. temperature at the sample	60 K	60 K

Table 4.1: Spectroscopic features of the ANTARES beamline at SOLEIL.

The end-station features nano-focusing optics, also known as FZPs. With zone plates, the energy resolution is in the range of $\approx 25\text{-}30 \text{ meV}$ with the beam spot focused down to 400 nm at 100 eV photon energy, while without them, the energy resolution is $\approx 15 \text{ meV}$, and the beam spot is extended to 80 microns. The ARPES chamber uses a multi-axis manipulator, which enables cooling down to 60K with or without the insertion of the FZPs.

The ANTARES setup can be used in two operating modes: spectroscopic imaging and spectroscopy with nano-spot, both of which make use of X-ray radiation. In the imaging mode, angle-resolved or angle-integrated photoelectron spectra are obtained when the sample position is changed, resulting in mapping 2D images of the electronic state of interest. In the spectroscopy mode, a detailed electronic band structure is probed at a fixed sample position.

The Fresnel zone plates

ANTARES is the world's first commissioned nano-ARPES beamline, employing FZPs focusing technology. FZPs can produce the smallest beam spot over a certain photon energy range. In practical applications, FZPs are typically optimized at a particular photon energy, and the ANTARES end-station typically uses 100 eV or 60 eV.

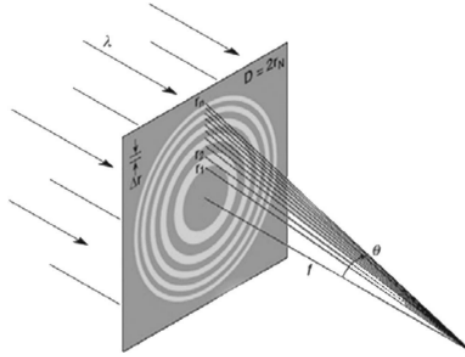


Figure 4.3: Fresnel zone plate [177].

As previously discussed, in order to achieve a small beam spot, the focusing optics and the sample must be very close to each other, which causes difficulties in collecting the emitted electrons. To prevent this, the working distance between the FZP and the sample can be extended by increasing the size of the FZP.

FZP lenses are made up of a set of equally spaced concentric rings, which alternate between opaque and transparent zones. The light that strikes the zone plate will diffract and constructively interfere at the focal point. The focal length (f) of FZP is directly proportional to the photon energy, $f = D \Delta r_N / \lambda$, where λ is the wavelength of the incident X-ray, D is the diameter of FZP and Δr_N is the size of the outermost zone width.

In this thesis, we performed certain ARPES experiments at the ANTARES beamline using zone plate optics which allowed us to selectively probe the micrometer sized 2D flakes. The details are provided in chapter 5.

4.3 MAESTRO beamline at ALS

The beamline

The second-generation nano-ARPES instrument is installed at the MAESTRO (Microscopic And Electronic STRucture Observatory) beamline in sector 7 at the ALS, Lawrence Berkeley National Laboratory in the U.S.A. [178]. The ALS storage ring operates in top-up mode with an electron energy of 1.8 GeV and a current of 500 mA. To assure nanoscale alignment of the focusing optics, the specimen at this beamline is mounted on a high-precision sample plate; a similar technique as used at the ANTARES beamline [179].

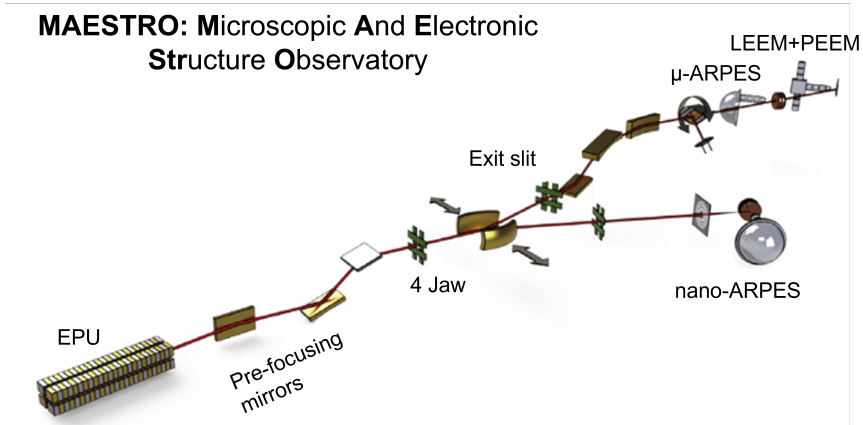


Figure 4.4: Schematic depiction of the MAESTRO beamline at ALS. It consists of various experimental end-stations including low-energy electron microscopy (LEEM), photoemission electron microscopy (PEEM), μ -ARPES and nano-ARPES techniques [180, 181].

The experimental end-station and spectroscopic features

The MAESTRO beamline is equipped with a versatile experimental end-station, as shown in fig. 4.4. It is divided into two main sections: preparation chamber and analysis chamber. The preparation chamber is equipped with a glove box, pulse laser deposition (PLD), and molecular beam epitaxy (MBE) techniques to do in-situ sample preparation. The analysis chamber of the beamline consists of state-of-the-art angle-resolved photoemission setups with different focusing

optics.

Depending on the spatial resolution, the spatially-resolved ARPES approach is referred to as μ -ARPES or nano-ARPES. The end-station at the MAESTRO beamline is fitted with two ARPES chambers. One is μ -ARPES equipped with K-B focusing optics [182], and the other one is nano-ARPES with two additional focusing optics (FZP, capillary) to perform μ -ARPES and nano-ARPES studies [183–186]. We had been using the nano-ARPES chamber, which is equipped with a multiaxis manipulator, allowing the precise positioning of the sample as described in section 4.2 integrated with the cooling sample stage, which can be cooled down to 40K by using liquid helium. In this chamber, two types of focusing optics can be used to focus the beam spot from $\sim 1\text{-}4\ \mu\text{m}$ down to a few hundred nm range, i.e., capillary optics and diffractive optics such as FZP. FZPs are limited to single-photon energies, whereas capillary optics allow one to choose of any photon energy within the available range [187]. The MAESTRO beamline has various capabilities, but we have only used capillary focusing because of the high X-ray flux, which makes it fast and convenient. Some of the spectroscopic features of the beamline are listed in table 4.2 and details could be found in [188].

Chambers	Analyzer	ALS Photon Range	Energy resolution	ALS spot size
nanoARPES (nARPES)	R4000	80-1000 eV	$\geq 50\ \text{meV}$	HiRes Mode: <120 nm using FZPs LoRes/ HiFlux Mode: <1-2 μm using capillary

Table 4.2: Spectroscopic features of the MAESTRO beamline at ALS [188].

Capillary optics

At the MAESTRO beamline, soft x-rays can be focused to a small beam spot using either zone plates or capillary optics. Some of the shortcomings of the zone plate technology can be overcome by using the capillary mirror optics developed by Sigray [189]. Capillary optics is in the shape of an ellipsoid, and the reflective surface is coated with a metal, typically platinum (Pt). The inside surface of a capillary is used to focus the incoming beam. It is necessary to block the center

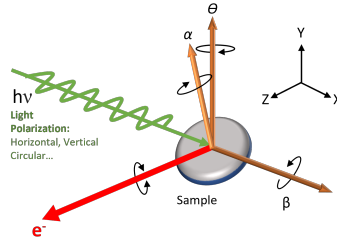


Figure 4.5: Illustration of the experimental geometry of the ARPES setup at MAESTRO beamline [180].

beam in order to eliminate the non-focused portion of the beam. Figure 4.6 depicts the beam layout used to test the capillary optics. The capillary optic is achromatic and has larger numerical apertures, allowing it to absorb a larger X-ray beam, resulting in a 100- to 1000-fold increase in the X-ray flux as compared to FZPs. A comprehensive description of how the capillary optic works can be found in [187].

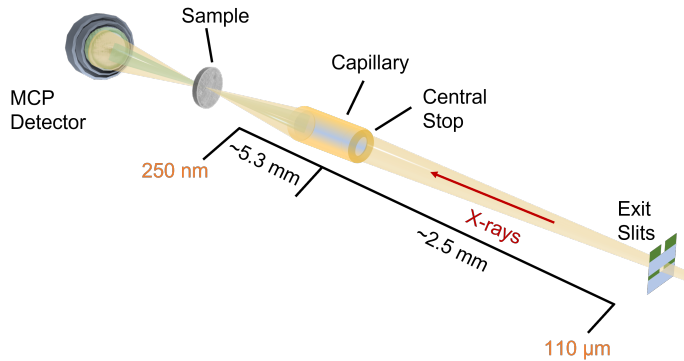


Figure 4.6: Beam layout used to test the capillary optics at MAESTRO beamline. Reproduced from [187].

The majority of the ARPES experiments in this thesis were carried out at the MAESTRO beamline using capillary focusing optics. This was beneficial since it allowed us to selectively explore different regions on the 2D flakes of WSe_2 due to the focusing down to $\sim 1\text{-}2\ \mu\text{m}$ beam spot. Additionally, having a large X-ray flux decreases the time needed to acquire 2D, 3D, or four-dimensional (4D) datasets for our studies, which will be presented in chapter 5.

4.4 NanoESCA beamline at Elettra

The beamline

PGI-6 operates the NanoESCA beamline at the Elettra synchrotron facility in Trieste, Italy, that is equipped with a modified momentum microscope based on the Focus NanoESCA concept. NanoESCA is a commercially available PEEM that is designed to combine the high spatial resolution (better than 150 nm) imaging with good energy resolution (better than 70 meV) to allow chemical analysis at each point in the image [190].

An advantage of the NanoESCA setup is that the E_{kin} versus $k_{||}$ analysis can be carried out in a way similar to standard ARPES by projecting the Fourier plane rather than the real space image of the energy-filtered photoelectrons onto the 2D detector, thus performing the so-called k -space microscopy. Utilizing the photon beam spot of $\sim 15 - 20 \mu\text{m}$ diameter, the NanoESCA setup can be used to selectively measure microscopic samples in the energy mode, making it suitable for probing the electronic band structure of larger exfoliated flakes.

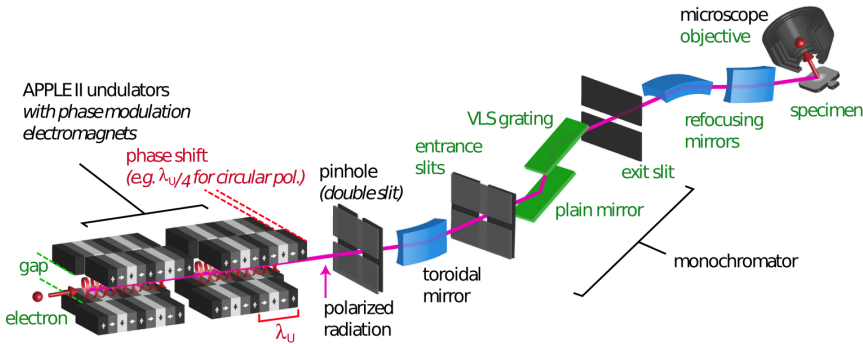


Figure 4.7: Illustration of the dual undulator beamline with micro-focusing at Elettra synchrotron facility (adapted from [191]).

The NanoESCA beamline is engineered to provide a high photon flux density, and the beamline scheme is depicted in fig. 4.7. A detailed characterization can be found in the Ph.D. thesis of Marten Patt [191]. The essential parameters of the NanoESCA beamline performance are summarized in table 4.3.

Polarization	Linear horizontal and vertical, elliptical
Energy range	40-1000 eV
Beamspot on the sample	15 μm x 10 μm (Hor. x Vert.) at 25° grazing incident

Table 4.3: NanoESCA Beamline specification.

The experimental end-station

The microscope consists of a first optical column that is placed in front of the specimen along its normal direction and collects the photo-emitted electrons. Following that, there is a double-hemispherical analyzer via which the extracted electrons pass through retaining the image during the energy filtering process, and a second optical column, that projects the electrons onto the 2D detector. In addition, another detector is installed after the first optical column, as well as a channeltron after the first hemisphere. Therefore, the NanoESCA microscope may operate in three different modes: PEEM, energy-filtered PEEM mode, channeltron, as shown in fig. 4.8 and further details can be found in [191].

The NanoESCA microscope can be adapted for momentum measurements. The size of the probing area offers a good spatial resolution in momentum mode, because the beam spot can be focused to $\sim 15\text{-}20 \mu\text{m}$. Moreover, a field aperture can be used to reduce the probed region to $\approx 8\text{-}10 \mu\text{m}$ because it is positioned inside the image plane, thereby reducing the field of view in real space. Figure 4.8 illustrates the microscope design. The performance of the NanoESCA microscope is summarized in table 4.4.

Lateral resolution	> 100 nm
k_{\parallel} resolution	$\sim 0.04 \text{ \AA}^{-1}$
Min T	40K with LHe cooling

Table 4.4: Performance parameters of the NanoESCA microscope.

The NanoESCA microscope can switch between real space and reciprocal space mode by applying the voltage to the electrostatic lens in different combinations.

- **Real space mode** In real space mode, the spatial information of the photo-emitted electrons is preserved by integrating over a range of emis-

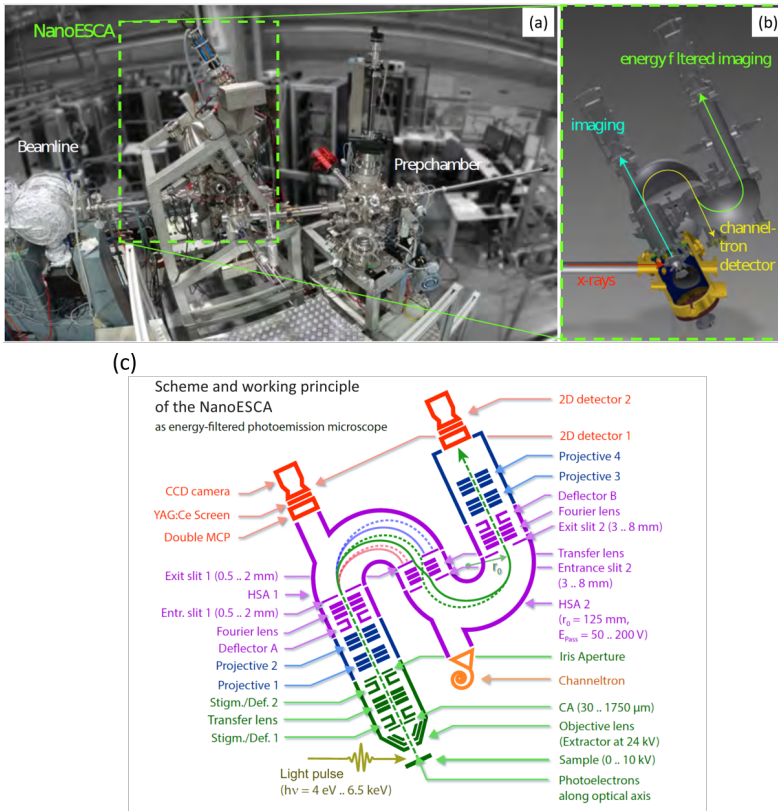


Figure 4.8: Panel (a): Photograph of the NanoESCA end station at the Elettra synchrotron in Trieste, Italy. The preparation chamber is employed with in-situ surface preparation and characterization techniques. The NanoESCA microscope can be operated in a variety of modes, as shown in panel (b). Panel (c) shows the scheme of the NanoESCA. Adapted from [191]).

sion angles at each point governed by the contrast aperture. This mode is compatible in both PEEM and energy-filtered PEEM modes. This operating mode is used to perform laterally-resolved chemical mapping and work function of the sample surfaces depending on the excitation light source.

- **Reciprocal space mode** In reciprocal space mode, the angularly and energetically resolved photo-emitted electrons are preserved while averaging over a selective area of the sample. This operating mode uses predominantly energy filter configuration, which allows access to detailed information on the electronic band structure of solid surfaces.

With a NanoESCA microscope at an extractor voltage of 12 kV, the objective lens has a wide momentum k_{\parallel} of acceptance, which helps to probe the entire Brillouin zone of most materials, i.e., $\pm 2 \text{ \AA}^{-1}$. This improves the efficiency and improved k-scale linearity of 2-D mapping of the entire BZ by eliminating the necessity for sample rotation. At a momentum microscope, the spectrum can be measured by scanning the in-plane momentum of the filtered kinetic energy of the photoelectrons in a single shot and obtaining a three-dimensional data stack $I(k_x, k_y, E_{kin})$ by measuring many (k_x, k_y) images at different kinetic energies. Thus, extracting intensity profiles from such image stacks can be used to determine electronic band dispersion along any desired reciprocal direction.

In this thesis work, the NanoESCA beamline was used to conduct ARPES and circular dichroism angular photoemission studies on monolayer, bilayer, and multi-layer of WSe_2 flakes. The details of the experiments will be provided in chapters 5 and 6.

Chapter 5

The Electronic Bandstructure of Twisted Monolayers and Bilayers of WSe₂

In the last few years, TMDCs have been one of the most studied vdW materials in 2D materials research, and particularly MoS₂, MoSe₂, WS₂ and WSe₂ have gained much attention [192]. It is well known that in these vdW materials, when thinned down to a monolayer, the change from an indirect bandgap semiconductor to a direct bandgap semiconductor occurs [129, 193]. Moreover, this transition has a direct impact on the optical and electric transport behavior of the material.

The vdW interlayer interaction allows for the exfoliation and artificial reassembling of various 2D materials into arbitrarily stacked hetero/homo-structures. Assembling individual layers with different electronic properties facilitates the idea of realizing artificial stacks of solids, so-called *van der Waals hetero-structures* (HSs) [25]. The HSs design enables the tailoring of band alignment at various semiconductor interfaces [27, 194] into different types of heterojunctions [28, 29, 101, 195, 196]. This approach of material design comprises the superposition of two crystal lattices with the same or different atomic registries, which leads to the construction of a long-range periodic superlattice. It often gives rise to a periodic moiré pattern potential, which can emerge either from the different lattice constants or the twist angle. In particular, the twist angle between such layers provides an adjustable degree of freedom compared to conventional materials. The strength of the moiré potential is typically in the range of several meV, and lattice electrons interacting with this additional potential may exhibit novel properties [30, 197]. Many fascinating experimental achievements have been published in recent years, and the resultant hetero/homo-structures pro-

vide novel features and use beyond their 2D parent crystals [42, 198–207]. This diversity offers the opportunity to construct atomically thin electronics based entirely on 2D materials [208–210].

Among the TMDCs, we have selected WSe₂ as a material of interest for this thesis, because of the strong SOC of W atoms, which makes the spin splitting in the valence band more significant in comparison to others. In recent years, large synthetic single crystals from WSe₂ became available commercially, and the crystals characterized in this chapter were purchased from the Dutch company HQ Graphene.

This chapter is divided into two sections: the first section summarizes multiple attempts to produce WSe₂ flakes on various substrates such as h-BN, SiO₂, and HOPG. This is followed by characterizing the WSe₂ mono/multi-layer sample structures to understand the influence of the substrate on its physical and electronic properties. This helps us to optimize the parameters required for our main ARPES experiments. In the second section, the electronic bandstructure of twisted monolayer, twisted bilayer, and multi-layer WSe₂ flakes on HOPG flakes were investigated using the μ -ARPES technique in combination with DFT calculations. The spotlight will be on the following issues in the twisted SL and twisted BL structures: the valence band maximum position, determination of twist angles, Dirac point replicas, photon energy dependence, and visualization of monolayer features in BL structures. All of the ab-initio DFT [77, 78] calculations presented in this chapter were performed by Dr. Hyun-Jung Kim and Dr. Gustav Bihlmayer at PGI-1 Forschungszentrum Juelich (FZJ).

5.1 μ -ARPES experiments at NanoESCA beamline

In this section, we study the effect of several substrates on exfoliated, atomically thin WSe₂ flakes by photoemission experiments, such as h-BN, SiO₂, and HOPG. Mechanical exfoliation is one of the most convenient ways for transferring a flake on different substrates for photoemission investigations. Thus, we procured mono/multi-layer flakes of WSe₂ on different substrates with the help of Dr. Sven Borghardt in collaboration with Prof. Beata Kardynal at PGI-9 Forschungszentrum Juelich. This group has expertise in fabricating monolayers and few layer 2D systems using the mechanical exfoliation technique. Each sample comprises a single twisted layer of a WSe₂ flake with a multi-layer part attached to it. A detailed description of the exfoliation and transfer process of the WSe₂ flake sample systems is presented in chapter 3.

Given the advantage of the NanoESCA beamline (NanoESCA end-station of PGI-6 at ELETTRA, Trieste) in detecting and measuring homogeneous regions on the sample surface at a micrometer scale ($\sim 10\text{-}20 \mu\text{m}$) by offering real-space imaging capabilities with microscopic control of the beam-spot, most of the photoemission experiments presented in this section on the WSe₂ samples were performed there. Although the lab-based photoemission setups provide higher resolution, their macroscopic beam spot makes them unfeasible to perform experiments on micrometers size ($\leq 10\text{-}20 \mu\text{m}$) WSe₂ flake samples. All measurements on WSe₂ samples presented in this section were performed with a photon energy of 40 eV at $T \sim 80\text{K}$.

5.1.1 h-BN as a substrate

For the first understanding of the sample system within this study, we started our studies by transferring SL WSe₂ on a few layers of h-BN substrate. Figure 5.1 presents monolayer WSe₂ on h-BN, thus forming a SL WSe₂/h-BN structure on Si(001). The group of Prof. Kardynal has analyzed this sample structure in photoluminescence (PL) studies by exciting it at 660 nm. The PL spectrum shows the neutral and charged excitons, as well as low energy bands characteristic for WSe₂ [211–213]. However, when the samples were examined in ARPES experiments, we noticed a charging effect, ruling out the possibility of employing

h-BN as a possible substrate for this research.

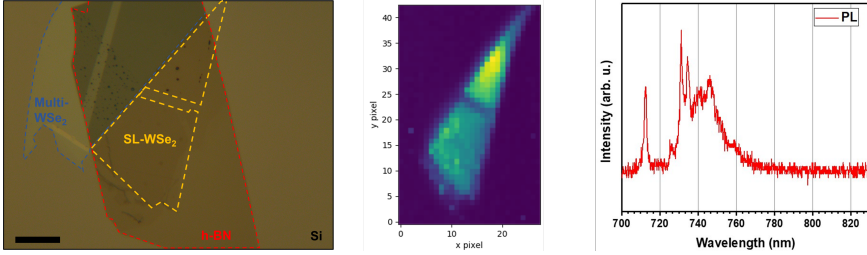


Figure 5.1: Left: Optical micrograph of a WSe₂ monolayer (yellow) partly placed on 30 nm h-BN (red) and partly placed on a Si(001) substrate. A multi-layer WSe₂ flake (blue) creates an electrical contact between the monolayer WSe₂ flake and the silicon substrate. The scale bar is 20 μm . Center: Spatial map of the integrated photoluminescence signal of the WSe₂ monolayer excited at 660 nm. Right: Representative photoluminescence spectrum of the WSe₂ monolayer.

5.1.2 SiO₂ as a substrate

Afterwards, the subsequent samples were fabricated by placing atomically thin WSe₂ flakes directly on highly n-doped Si substrates with native SiO₂. One can consider the Si substrate as a feasible candidate for studying quasi-freestanding layers [214, 215]. However, the photoemission studies exhibit a different issue, wherein the spectra acquired on such samples were of low quality. While the spectral features for the WSe₂ monolayer can be identified, they are not sharp enough to clearly reveal detailed dispersive features as we expected to observe from a WSe₂ monolayer. This is due to the presence of impurities introduced by the multiple layer coating of adsorbates on substrate.

To resolve this, possible scenarios were considered; this included preparing samples in the UHV system before the photoemission experiments, using different annealing temperatures, and sputtering with low energy argon ions. Despite following this, the sample surfaces were not clean and homogenous enough to exhibit a sharp, distinct band dispersion during the μ -ARPES experiments. Another possible reason for this could be a high and varying surface roughness of SiO₂ substrate causing corrugation and buckling of the WSe₂ flake.

Figure 5.2 shows an example where the monolayer WSe₂ flake is placed on top of SiO₂. Figure 5.2 (a) shows the optical micrograph of the SL WSe₂/SiO₂. The

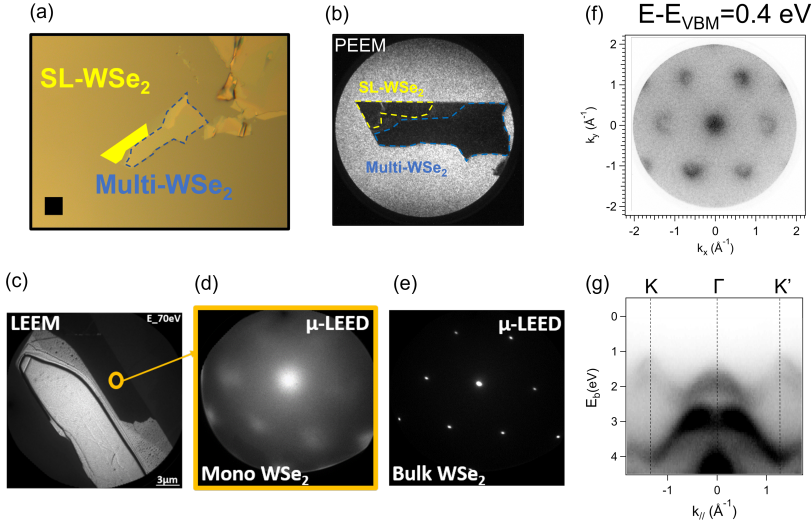


Figure 5.2: (a) Optical micrograph of a WSe₂ monolayer flake (yellow) and multi-layer WSe₂ flake (blue dashed line) placed on a Si(001) substrate. The scale bar is 10 μm . (b) PEEM image taken by a Hg lamp at the NanoESCA beamline with a field of view of 60 μm . (c) LEEM image of the optical micrograph taken at an electron energy of 70 eV. (d,e) μ -LEED images were acquired on monolayer and multi-layer region on the WSe₂ sample, respectively. It shows sharp features at multi-layer part indicating the 6-fold crystal symmetry. LEEM and μ -LEED experiments were performed at Jerzy Haber Institute of Catalysis and Surface Chemistry, Polish Academy of Sciences, Kraków, in collaboration with Prof. Nika Spiridis's group. (f) Constant energy map (CEM) at $E-E_{\text{VBM}} = 0.4$ eV and (g) is the $E(k)$ cut along K - Γ - K' on the monolayer part of WSe₂.

sample was introduced into UHV and degassed for two hours at 300°C prior to performing photoemission experiments at the NanoESCA beamline. (b) The PEEM image shows the intensity contrast indicating the monolayer and multi-layer parts of the WSe₂ flake. In this particular experiment, the beam spot on the sample is 15×20 μm in size and remains stable even after several hours. Moreover, the field aperture of the PEEM can limit the field of view in real space down to $\simeq 8$ μm . Therefore, in the ARPES mode, the monolayer and multi-layer parts of the sample can be measured selectively. The WSe₂ monolayer ARPES data is shown in fig. 5.2(f,g), measured at a photon energy of 40 eV to achieve a combination of high surface sensitivity and high photon flux from the beamline. Figure 5.2(f) is the constant energy map measured at $E-E_{\text{VBM}}=0.4$ eV and fig. 5.2(g) shows the energy-momentum map along the K - Γ - K' direction

on the monolayer region of WSe₂ flake. This indicates that the VBM lies at K and confirms that this is the monolayer part.

In order to resolve the difficulties with the ARPES experiments, an alternative approach was adopted, where WSe₂ flakes were placed on thick HOPG flakes that had previously been exfoliated onto the Si/SiO₂ substrates. HOPG is a vdW material offering a viable alternative to SiO₂ for degassing at moderate and high temperatures in UHV to provide a clean surface and interface. We will discuss these results in detail in the next section of this chapter.

5.2 μ -ARPES experiments at MAESTRO and ANTARES beamlines

All of the atomically thin WSe₂ sample structures used in this section were fabricated in collaboration with Dr. Bernd Beschoten's group at RWTH Aachen University by Lars Rathmann and me. As already discussed in chapter 3, the samples were prepared by mechanical exfoliation and dry transfer methods. Using this method, we prepared three SL samples and two different BL WSe₂ samples, labeled as sample *A*, sample *B* and sample *C*. Each BL sample comprises a twisted single layer of WSe₂/graphite (SL WSe₂/graphite) and twisted bilayer layer of WSe₂/graphite (BL WSe₂/graphite).

The majority of photoemission experiments on the atomically thin WSe₂ samples presented in this section were performed at the MAESTRO end-station at ALS, U.S.A. The samples were transported to the beamline in argon sealed gel boxes where they were inserted into the μ -ARPES UHV end-station with a base pressure lower than 5×10^{-11} mbar. The samples were annealed at 300°C for several hours prior to the measurement in order to desorb adsorbates. The μ -ARPES measurements were performed with capillary focusing primarily using a photon energy of 147 eV and a beam spot size of approximately 1 μm [187]. The data were collected using a customized hemispherical Scienta R4000 electron analyzer. All measurements were taken at $T \sim 40\text{K}$.

In addition, the μ -ARPES measurements were also conducted at the ANTARES beamline of the SOLEIL synchrotron facility on sample *A*. Before the actual measurements, we followed the same sample preparation procedures as those used at the MAESTRO beamline. At ANTARES, by utilizing Fresnel zone plate optics, the photon beam was focused below 1 μm . All measurements there were carried out at $h\nu = 100$ eV with linear horizontal light polarization and at $T \sim 100\text{K}$.

Further experiments on atomically thin SL WSe₂/graphite microstructure (sample *C*) were performed at the NanoESCA beamline of Elettra, Trieste, with the beam spot size of 10-15 μm using a modified FOCUS NanoESCA momentum microscope. Before the experiments, the sample was subjected to the same preparation processes as at other beamlines. Homogeneous region on the sample surface was identified by using the PEEM in real space with a Hg lamp as

an excitation source. Moreover, unlike traditional ARPES setups, a momentum microscope scans the complete half-space emission without rotating the sample and enables high linearity in the $k_{||x}$ vs $k_{||y}$ maps. All measurements at NanoESCA were taken at $h\nu = 40$ eV and at 80K.

5.2.1 Identification of SL and BL micro-regions

Figure 5.3(a) shows the schematic arrangement and 5.3(b), 5.4(a) the optical micrographs of the SL WSe₂/graphite and BL WSe₂/graphite flakes structures at different twist angles of sample *A* and sample *B*. They contain several interfaces with varying twist angles between the corresponding 2D flakes. A graphite flake was exfoliated directly onto a highly n-doped silicon wafer and served as an atomically flat conducting substrate for the sample structures. The sample region where any portion of the top WSe₂ monolayer flake covers the bottom monolayer flake of WSe₂ is the BL region. The areas of the overlapping regions of twisted BL WSe₂/graphite and twisted SL WSe₂/graphite flakes are denoted by the gray and yellow dotted lines in figs. 5.3(b) and 5.4(a), respectively.

The micro-focused beam of photons has been scanned over the sample surface at a photon energy of 147 eV in the same region as shown in the optical image in figs. 5.3(b) and 5.4(a) to identify each interface embedded in the sample by measuring photoelectrons emitted from the valence bands at the momenta related to WSe₂. Thus, the energy-momentum dispersion maps can be derived from any region of interest (ROI) on the sample surface. Figures 5.3(c) and 5.4(b) depict spatial photoemission maps of the integrated valence band intensity in the vicinity of Γ_0 of a sample *A* and sample *B*. These maps assist us in distinguishing between the distinct regions of the sample surface consisting of WSe₂ flakes and graphite flakes.

Each sample contains multiple SL, BL, and multi-layer flakes that are experimentally selected by focusing the micro-spot into the desired region. This behavior is studied in detail by acquiring the energy-momentum dispersion plots at normal emission (Γ_0) of the WSe₂ BZ. These measurements were conducted by using capillary focusing optics. The excellent efficiency of the capillary optics enables us to capture the 3D data $I(E_{bin}, k_x, k_y)$ in about 45 to 55 minutes, depending on the required signal to noise ratio. We present a collection of line-scan spectra for 11 points in sample *A* and sample *B* to illustrate that the experiments were car-

ried out at adequate resolution. In figs. 5.3(c) and 5.4(b), the numbered white and black boxes were used to illustrate the direction of the line-scan spectra and the positions at which we acquired the data set.

Figure 5.3(d) depicts a set of ARPES maps at 11 boxes indicated in (c), demonstrating that the microfocused beamspot can precisely select a desired area from the sample, clearly distinguishing between SL (boxes 1-2 in (c), single band at the VBM at Γ_0), BL (boxes 6-8, double band at Γ_0), and graphite (boxes 10-11)

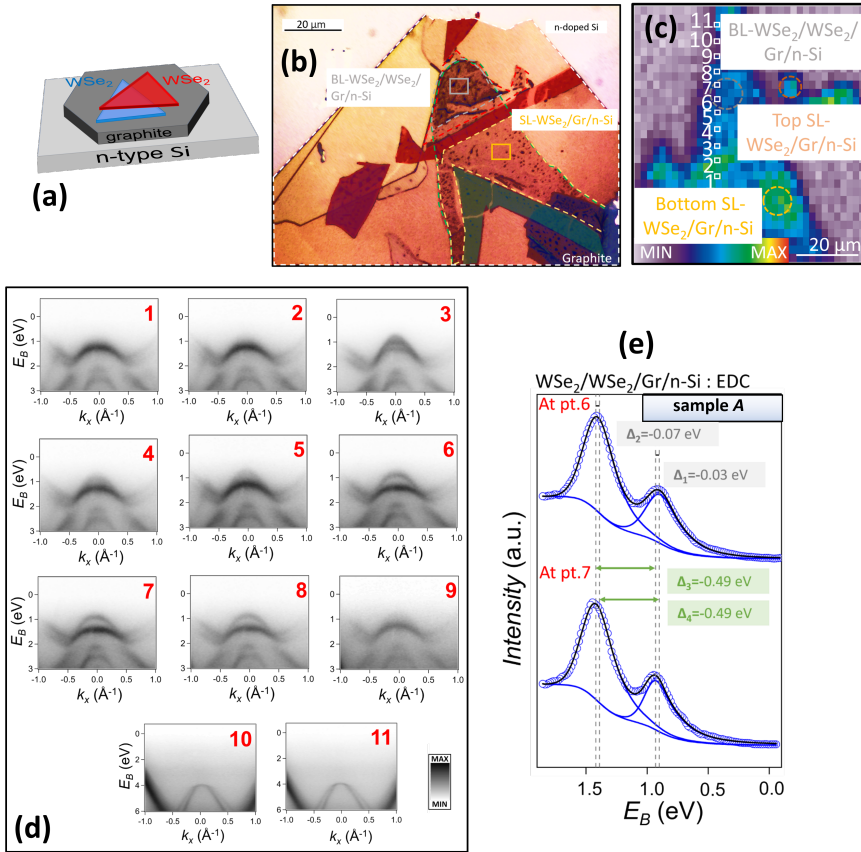


Figure 5.3: Characterization of sample A: (a) Schematic model of the sample configuration. Different nanosheets are denoted by blue, red, and gray colors. (b) Optical image of the twisted SL and BL WSe₂/graphite/n-Si, and (c) the spatial photoemission intensity map of the integrated intensity of the valence band near the Γ_0 point of WSe₂. (d) Set of normal emission ARPES maps at $h\nu = 147$ eV at white boxes indicated in (c). (e) Normal emission EDCs at boxes 6 and 7.

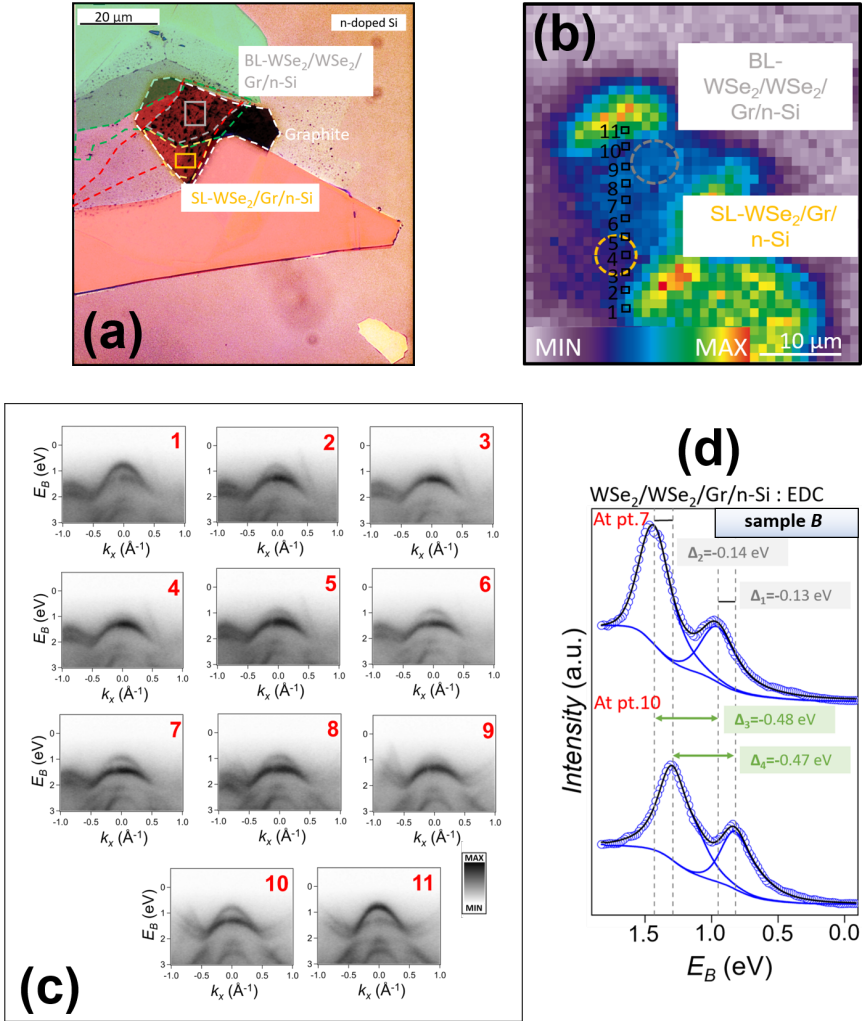


Figure 5.4: Characterization of sample *B*: (a) Optical image of the twisted SL and BL WSe_2 /graphite/n-Si, and (b) the spatial photoemission intensity map of the integrated intensity of the valence band near the Γ_0 point of WSe_2 . (c) Set of normal emission ARPES maps at $h\nu = 147$ eV at black boxes indicated in (b). (d) Normal emission EDCs at boxes 7 and 10.

regions of sample *A*. Similar kind of measurements were observed in sample *B* as shown in fig. 5.4(c) where boxes 3-4 indicate single band and boxes 6-8, 10-11 show double bands at the Γ_0 . The double band near VBM at Γ_0 results from bonding-antibonding interaction between d_{z^2} and p_z orbitals from the adjacent

layers, and is a signature of a BL. Respectively a single band is a signature of a SL. Therefore, the results of figs. 5.3 and 5.4 indicate that we were able to exclusively probe either SL or BL regions by adjusting the position of the beam spot on the sample. In figs. 5.3(e) and 5.4(d) we show Voigt fits of the normal emission energy dispersion curves (EDCs) at different points on the same micro flakes. For the BL regions, we identify binding energy shift of the order of ~ 30 meV of a sample *A* from boxes 6 and 7. Similarly, in sample *B* the binding energy shift from boxes 7 and 10 is ~ 130 meV. This suggests inhomogeneities and local doping varying on the μm scale on the flake surface within the BL region. The splitting between bonding and antibonding states at Γ is between 0.48 and 0.52 eV at different positions of samples *A* and *B*. These values are significantly smaller than ~ 0.6 eV in non-twisted BL WSe₂ [45, 46, 216, 217], which suggests reduced hybridization in our twisted layers.

Additionally, sample *A* had been characterized at the ANTARES beamline (SOLEIL synchrotron). As seen in fig. 5.5(a), utilizing nano-APRES in the imaging mode, different regions of the WSe₂ flake can be distinguished. The electronic band structure could be acquired using the nano-ARPES beamline in spectroscopic mode, as shown in fig. 5.5(b,c), which depict the band dispersions of the monolayer and bilayer regions. At the high symmetry Γ_0 point, the monolayer region exhibits a single band at the local valence band maximum. In the bilayer region, the band is split into two branches. The results observed at the ANTARES beamline are in agreement with those obtained at the MAESTRO beamline.

5.2.2 Photon energy dependence

Figure 5.6(a) shows the photon energy dependence ($E_b(k_\perp)$) map at the BL region of sample *A* made from normal emission EDCs for $h\nu$ between 80 and 150 eV, with the perpendicular momentum $k_\perp = \sqrt{(E_{kin} + V_0)2m/\hbar^2}$, and V_0 set to 10 eV. The bonding-antibonding features near the local VBM at Γ_0 (E_b near 1 eV and 1.5 eV) are present at all probed k_\perp . Furthermore, these states exhibit the expected intensity modulation due to the final state interference (the matrix element effect), with no other states appearing in this range. This indicates that we are exclusively probing the BL region. Qualitatively, the mechanism of this modulation can be explained through the free-electron final state ARPES

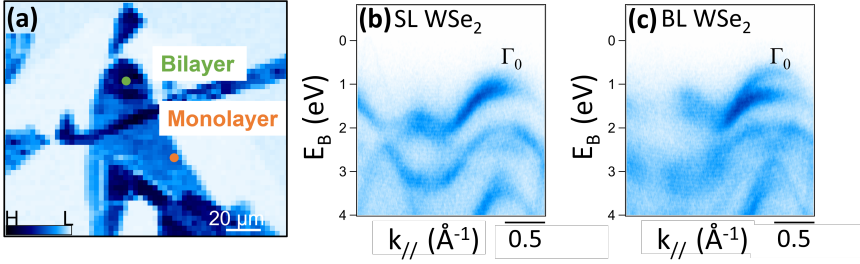


Figure 5.5: Band structure of different regions of WSe₂ flake by nano-ARPES. Panel (a) shows the nano-ARPES image obtained by integrating intensity from 0.5 eV to 0.9 eV. Panels (b,c) show the band dispersion taken at $h\nu = 100$ eV along the Γ - K direction of the Brillouin zone from the two regions labeled in panel (a) by green and orange dots.

model [56], where the normal emission free-electron final state (FEFS) matrix element $\langle e^{ik_{f\perp}\cdot z} | \Psi \rangle$ for the two hybridized layers separated by a distance d is modulated by the factor $1 + e^{ik_{\perp}\cdot d}$. In more accurate models of photoemission, one takes into account not only the radial part of the orbital wave function and the selection rules [56], that will lead to further intensity modulation, but also the proper inverse LEED final state [218].

A similar photon energy scan for sample *B* is reported in fig. 5.7. For sample *B*, we did a photon energy scan from 80 to 150 eV with a 2 eV step width to investigate what could change for different twist angles. However, we see virtually the same findings as in sample *A*.

We plotted normal emission EDC profiles of the first two non-dispersive features near the local VBM followed by a Voigt fitting to precisely determine the peak positions as shown in fig. 5.6(b) and fig. 5.7(b) for both samples. At different photon energies, we observed that the average splitting between bonding and antibonding orbitals is in the order of ~ 450 meV. In the figs. 5.6(c) and 5.7(c), we show selected EDC profiles obtained at two different photon energies for each sample, where the spectra indicate a considerable energy shift between the topmost valence bands. The selected photon energies for sample *A* were 130 eV and 90 eV, while the selected photon energies for sample *B* were 146 eV and 88 eV. For the specified photon energies, sample *A* exhibits an energy shift of ~ 60 meV, while sample *B* show an energy shift of ~ 30 meV. This effect can be attributed to the inhomogeneity of the sample surface and operating conditions, which enabled a slight beam drifting during the sample measurements.

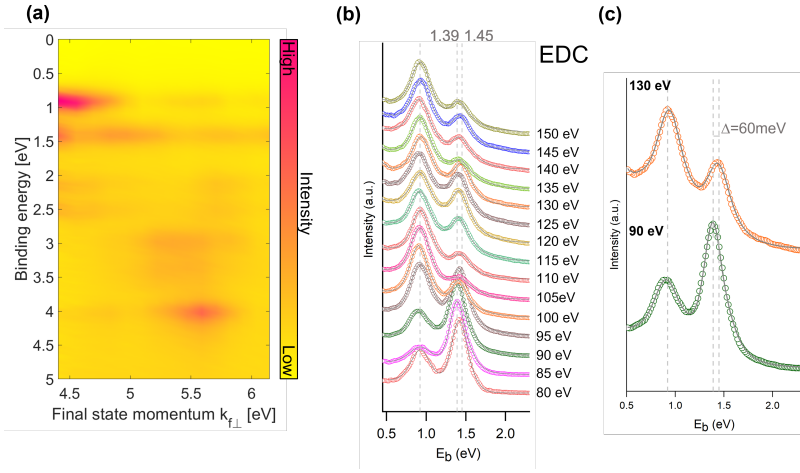


Figure 5.6: Sample A: (a) $E_B(k_{\perp})$ map made from set of normal emission EDCs for $h\nu$ between 80 and 150 eV. (b) EDC profiles taken at non-dispersive features of (a) at different photon energies. EDC profiles at $h\nu = 180$ eV and 90 eV are shown in (c), indicating a ~ 60 meV energy shift.

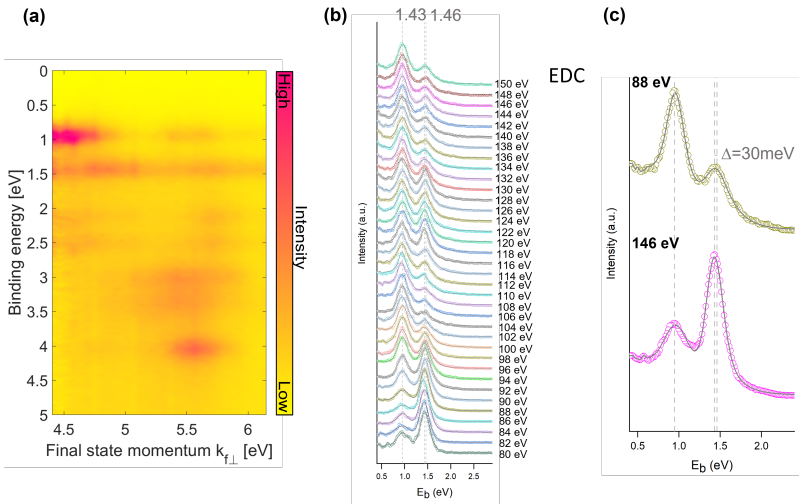


Figure 5.7: Sample B: (a) $E_B(k_{\perp})$ map made from set of normal emission EDCs for $h\nu$ between 80 and 150 eV. (b) EDC profiles taken at non-dispersive features of (a) at different photon energies. EDC profiles at $h\nu = 88$ eV and 146 eV are shown in (c), indicating a ~ 30 meV energy shift.

5.2.3 ARPES 3D data sets

Figure 5.8 shows an overview of $I(E_B, k_x, k_y)$ data sets from Sample *B*. The extended measured angular range allows imaging both Γ_0 (center of the first surface BZ, $k_x = k_y = 0$) and Γ_1 (second BZ) points of WSe₂ in a single map. The lower binding energy region shows K_{gr} points of the graphite substrate, depicted by hexagons in maps at $E_B = 0.4$ eV in (a-c). The binding energy region at $E_B = 0.8$ eV and higher contains a mixture of graphite and WSe₂ bands, and in the maps at $E_B = 0.8$ eV we identify first and second BZs of the WSe₂ layers through their respective Γ_1 points.

Similar maps for sample *A* are shown in fig. 5.9. The details of the Γ_1 region for the BL WSe₂ of sample *A* are shown in Fig. 5.10. A faint intensity related to the Γ_1 hole pocket of the bottom WSe₂ layer can be identified in fig. 5.9(a), and is depicted by the green circle in (b). The intensity ratio between top and bottom layer Γ_1 features is $\sim 5/1$, suggesting the inelastic mean free path of < 1 nm for WSe₂ valence electrons at our photon energy of 147 eV. Figure 5.10(c-e) show the $E_B(k_x)$ cuts through the Γ_1 points of the top and bottom WSe₂ layers. In (d) the faint shadow related to the hole pocket of the bottom WSe₂ layer can be identified, and it is depicted by the green dotted line in (e). Neither of these maps show the indications of the flat band formations due to the moiré potential of the twisted BL.

Figure 5.8(d-f) show details of the maps at $E_B = 1.2$ eV. Due to the lack of inversion symmetry, that results in a trigonal symmetry of the WSe₂ monolayer, the intensity of Γ_1 points at neighboring BZs is strongly modulated, with the signal from every second Γ_1 nearly vanishing. This effect is similar to trigonal LEED patterns measured on single-terrace terminations from TMDCs [135]. Interestingly, since the effect is observed in a SL, it indicates that it derives from the direction of the topmost W-Se bonds.

Since the topmost valence bands at Γ derive almost exclusively from the d_{z^2} orbitals localized on the W sites and p_z orbitals localized on Se, the effect can be explained by interference within the FEFS matrix element $\langle e^{i\mathbf{k}_f \cdot \mathbf{r}} | \Psi \rangle$, however, for a quantitative description one would need to consider a more complete final state.

We can utilize the clear trigonal symmetry of the CEMs to unambiguously assign the twist angle as visualized in fig. 5.8(f) and 5.9(d) for samples *B* and *A*

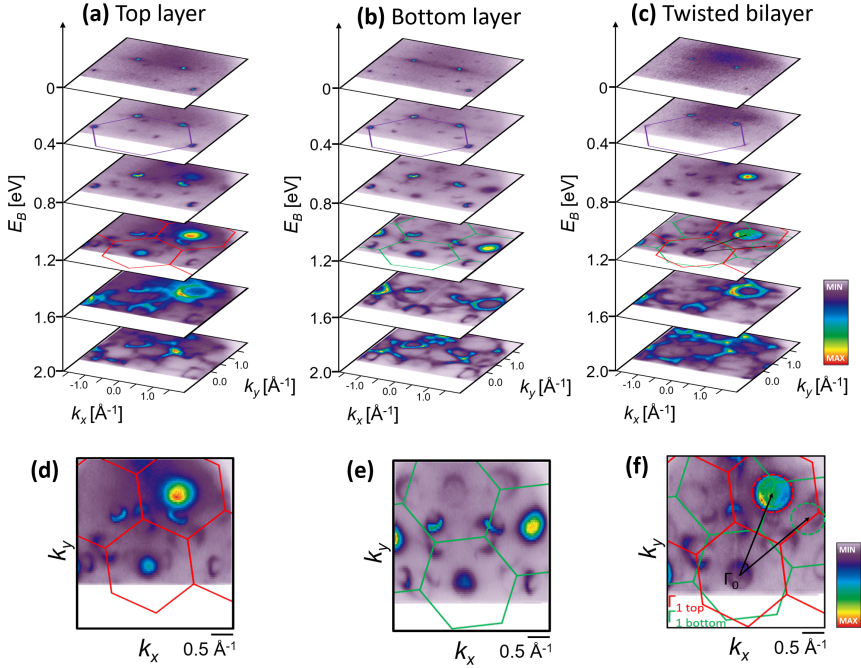


Figure 5.8: ARPES spectra from WSe₂ SL and BL of sample *B*. (a) and (b) show maps from top and bottom SLs, and (c) from the BL. (d-f) show details of the maps for top SL, bottom SL, and BL, respectively, at $E_B = 1.2$ eV. Red and green dashed circles in (f) represent the positions of the Γ_1 from top and bottom layer, and black arrows depict the twist angle.

respectively. The detailed analysis is presented in the 5.2.5, and yielded $\sim 28^\circ$ for sample *B* and $\sim 10^\circ$ for sample *A*. An accurate determination of the twist angle from hemispherical analyzer CEMs is complicated by intrinsic non-linearities in the angular scale, in particular, with the wide-angle mode ($\sim 36^\circ$) used in this work. These issues originate mostly from the analyzer lens system, and are difficult to systematically correct. We will further discuss them in the later part of the chapter.

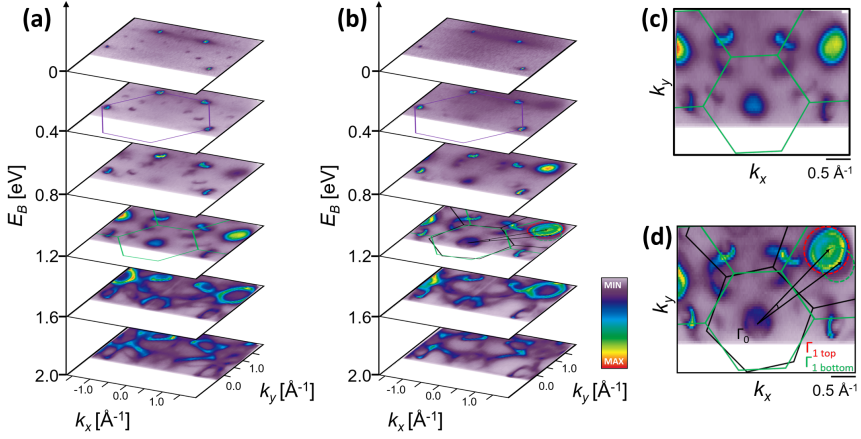


Figure 5.9: ARPES spectra from WSe_2 SL and BL of sample A. (a) shows the maps from the bottom SL and (b) from the BL. (c,d) show details of the maps from bottom SL, and BL, respectively, at $E_B = 1.2$ eV. Red and green dashed circles in (d) represent the positions of the Γ_1 from top and bottom layer, and black arrows depict the twist angle.

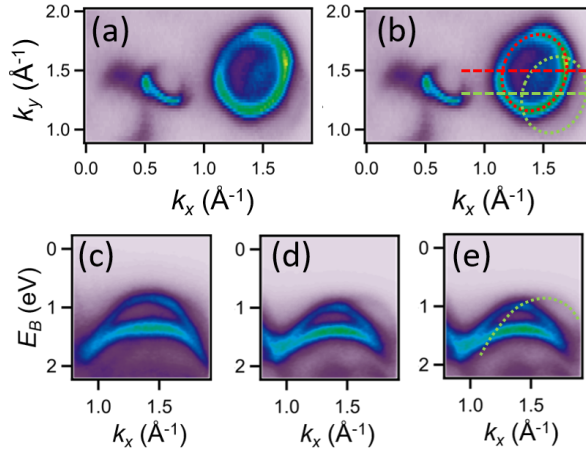


Figure 5.10: (a) Details of the spectra from sample A near the Γ_1 at $E_B = 1.14$ eV. (b) Same map as in (a) but with red and green circles indicating the positions of Γ_1 from top and bottom layers, respectively. (c,d) $E_B(k)$ cuts along the red and green dashed lines indicated in (b), respectively. (e) Same as (d) but with the guide line indicating the dispersion of the bottom layer Γ_1 band.

5.2.4 Copies of graphite K -point Dirac cones

The Fermi surface maps in figs. 5.8 and 5.9 show a set of dot-like features, which stem from the graphite Dirac cone-like dispersions. These maps are shown in detail in fig. 5.11, where one can see a set of intense dots related to the graphite K_{gr} point and additional weaker dots, which we attribute to their copies. When the electrons emitted from graphite are passing through the WSe₂ monolayer, they can be diffracted leading to first and higher order copies in the CEMs. These copies shall appear for all graphite bands, but they are most pronounced near the Fermi level, where the K_{gr} points are sharp and no other bands are present. Copies are further characterized to demonstrate their conical dispersion through the CEM at $E_B = 1$ eV (panel (e)) and comparison between the $E(k)$ map at the zero order graphite K_{gr} point (fig. 5.11 (f)) and one of the first order copies (fig. 5.11 (g)). Another case of such diffraction copies has been discussed by Ulstrup et al. [219] for a similar interface of graphene/WS₂. Compared to our WSe₂/graphite interface, in their case the sequence of layers is reversed, hence electrons emitted from WS₂ Γ_0 have been diffracted through the graphene layer.

Mathematically, the wave vectors of the copies can be computed through the reciprocal space vectors of participating layers, \mathbf{G}_W and \mathbf{G}_G for WSe₂ and graphite, respectively. We define the twist angle between graphite and WSe₂ as $\theta = \arccos(\frac{\mathbf{G}_W \cdot \mathbf{G}_G}{|\mathbf{G}_W| |\mathbf{G}_G|})$ and the moiré vector $\mathbf{G}_m = \mathbf{G}_W - \mathbf{G}_G$. Following ref. [219] we obtain the angle of the copies as $\phi_m = \arctan(\frac{\sin \theta}{\cos \theta - |\mathbf{G}_G|/|\mathbf{G}_W|})$ and the length of their vectors $|\mathbf{G}_m| = \frac{G_G^2 - |\mathbf{G}_G| |\mathbf{G}_W| \cos \theta}{|\mathbf{G}_G| \cos \phi_m}$.

Figure 5.12 shows the simulated results between the WSe₂ and graphite lattices. We show a few examples of the twist angle ranging from 2° to 25° to depict the position of graphite Dirac cones and their copies.

Figure 5.11(a-d) show the CEMs near the Fermi level ($E_B = 30$ meV) for the *bottom* and *top* SL WSe₂ structures of sample *B* (*bottom* and *top* refer to the SLs of the BL WSe₂, see fig. 5.8(a-b)). Panels (b) and (d) show the same data as (a) and (c), respectively, but with added simulated positions of the Dirac point copies according to the above equations. We have used $\theta = 7^\circ$ for the *bottom* SL (panel (b)) and $\theta = 24^\circ$ for the *top* SL (panel (d)) to obtain the best overall match with the experiment. Physically, the first order diffraction creates 6 copies around each K_{gr} point of graphite, at a reciprocal distances of \mathbf{G}_W . Some of these \mathbf{G}_W vectors are plotted in Fig. 5.11(h) to clarify the arrangement of copies

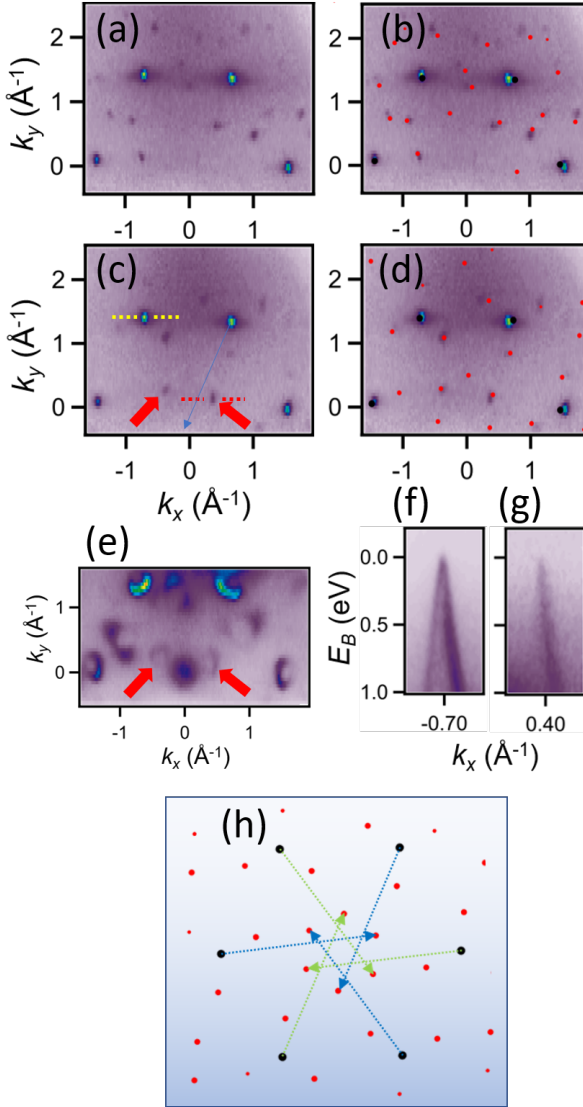


Figure 5.11: (a,b) Fermi level CEMs ($E_B = 30$ meV) for the bottom SL WSe₂/graphite in sample *B*. (c,d) Same for the top SL WSe₂/graphite. (e) CEM for the top SL WSe₂/graphite at $E_B = 1$ eV. (f) and (g) show $E_B(k_x)$ maps of zero order graphite *K* point and one of the copies along the trajectories indicated respectively by yellow and red dashed lines in (c). Red arrows in (c) and (e) identify selected copies of graphite *K* points, confirming conical shapes of their dispersions. (h) Arrangement of copies related to (d) with indicated \mathbf{G}_W vectors of SL WSe₂. Different color of the arrows reflect the trigonal symmetry of SL WSe₂.

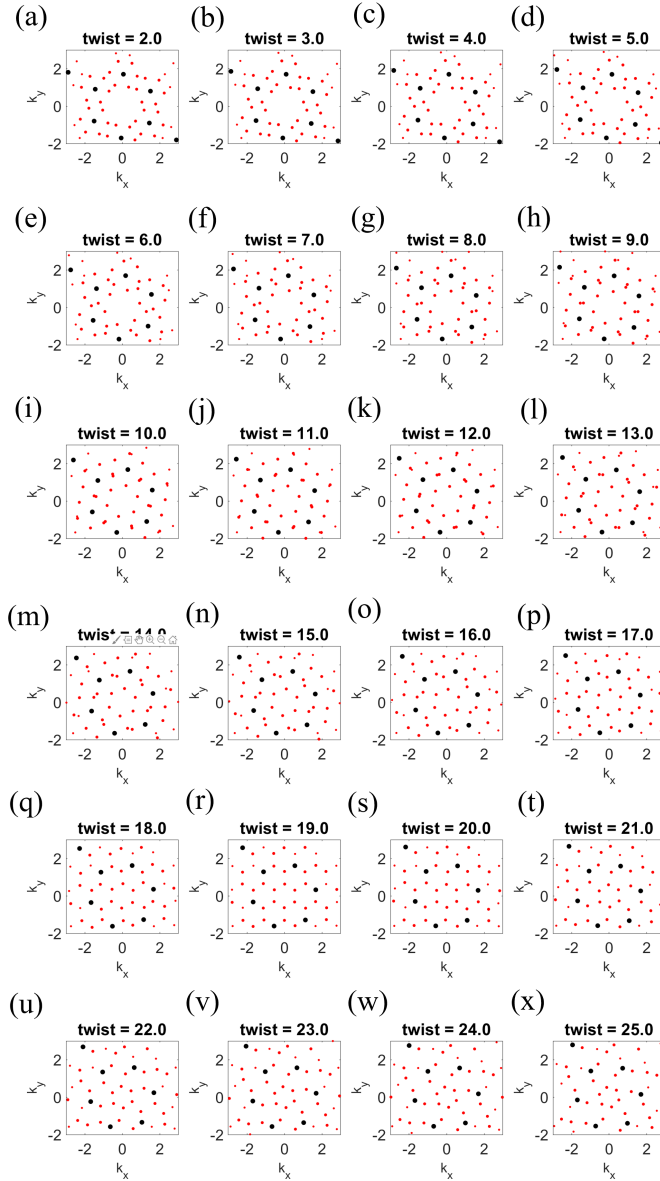


Figure 5.12: Analysis of main graphite Dirac cone and its copies on SL WSe₂ and graphite lattice:(a-x) show the possible orientations between these 2D lattices from 2° to 25° twist angle. The black dots indicate the graphite Dirac cones, and the red dots are their replicas.

near the zone center in fig. 5.11(d). Interestingly, in fig. 5.11 (d) only 3 out of these 6 copies can be identified, which we attribute to the lack of inversion symmetry in WSe_2 and the directional bonds, as discussed earlier.

Closer inspection of fig. 5.11 (b) and (d) reveals small discrepancies between the experimental and computed positions of the Dirac copies. We argue this is related to the non-linearities of the angular scale in the hemispherical analyzer 2D MCP detector, which might be further influenced by a slight off-axis misalignment of the photon beamspot with respect to the analyzer lens axis. These effects directly translate into momentum scale non-linearities. ARPES maps can also be measured by an alternative spectrometer design, the so-called momentum microscope [173]. In a momentum microscope, the rotational symmetry of the reciprocal space around the sample surface normal is faithfully reproduced through the cylindrical symmetry of the spectrometer lens due to the momentum microscope design. Raw data exhibits a small binding energy shift of 20-50 meV throughout the 2D map, which in principle can be corrected, but has been neglected here.

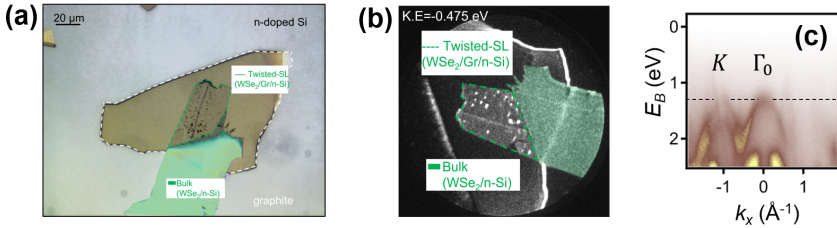


Figure 5.13: Overview of sample C . (a) Optical micrograph of twisted SL WSe_2 placed on graphite with the entire sample structure lying on the top of n -Si. (b) PEEM image of the sample taken with a Hg lamp at NanoESCA beamline at Elettra, where twisted SL and bulk WSe_2 flakes are represented by the dotted green lines and shaded green color regions, respectively. (c) $E(k_x)$ map at Γ_0 indicating single band at normal emission.

We have performed momentum microscopy at the NanoESCA beamline at Elettra synchrotron on sample C . Sample C was also fabricated by mechanical exfoliation and dry transfer techniques, and contained a SL WSe_2 flake of 20 μm lateral size on graphite as shown in fig. 5.13. It was essential to prepare such large flake due to the photon beamspot of 15-20 μm at the NanoESCA beamline. Figure 5.14 shows the momentum microscope maps from sample C . One can see that the overall fitting of the Dirac copies is more accurate as compared to fig.

5.11, and allows to establish the twist angle of $\sim 17.2^\circ$ between graphite and SL WSe₂ in sample *C*. Again, the arrangement of copies has a trigonal symmetry, in contrast to zero-order K_{gr} points which have a hexagonal symmetry.

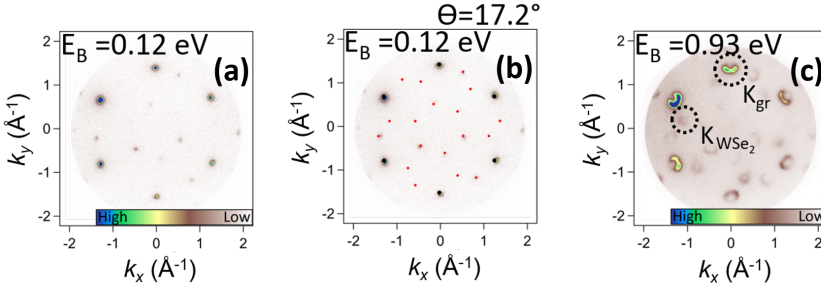


Figure 5.14: Maps measured on sample *C* at the NanoESCA beamline with *p*-polarized light at $h\nu = 40$ eV at 80K. (a) CEM of SL WSe₂/graphite at $E_B = 0.12$ eV. (b) same as (a) but overlaid with Dirac copies calculated for 17.2° twist angle between WSe₂ and graphite. (c) CEM at $E_B = 0.93$ eV, indicating the K points of graphite and WSe₂. The measurement was performed by using linearly *p*-polarized light at 40 eV and at $T \sim 80$ K

In BL WSe₂ flakes of sample *B*, replicas of graphite K -point Dirac cones are also present, although the intensity is relatively low in comparison to the twisted SL WSe₂/graphite. Most of the copies on the Fermi surfaces of twisted BL structures are attributed to the top monolayer of the WSe₂ flake but the contribution from the bottom layer, which is very small, is also present, as shown in fig. 5.15. The copies contributed from the bottom layer are marked by a circle on the Fermi surface of BL, and on the respective monolayer, it is marked by black arrows, as shown in fig. 5.15(c,d). We observed here the fainter copies of the graphite Dirac points. The color scale is saturated to highlight these copies.

In both twisted SL and BL WSe₂/graphite sample structures, the electrons emitted from graphite near the Fermi level are focused in K_{gr} points, and we observe diffraction of these electrons when passing through WSe₂. The arrangement of these replicas (sometimes called mini-bands [219]), which are basically umklapp transitions due to the WSe₂ lattice vectors, can be explained as a final state effect that would be present also in non-interacting layers. Essentially the same process is expected when shooting the electron beam through a freestanding SL WSe₂ or when performing a LEED scattering experiment. Accordingly, the intensity of the copies follows the trigonal symmetry of a monolayer. Therefore,

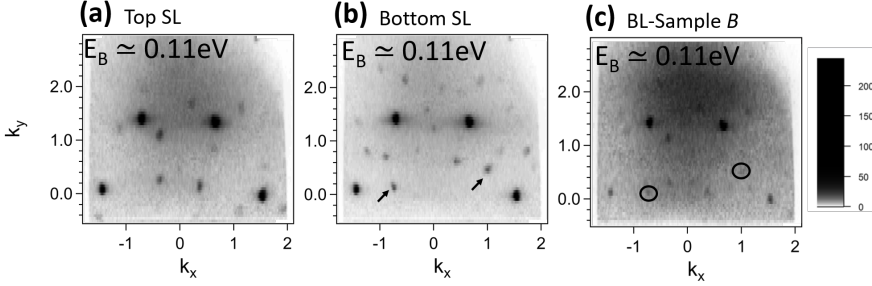


Figure 5.15: Constant energy cuts at $E_B \approx 0.11$ eV: (a,b) Fermi surface of the top and bottom monolayer of WSe₂ of sample *B*. The color scale is saturated to highlight copies of the main graphite Dirac cone. The k_x and k_y scaling of each constant energy map are in \AA^{-1} .

the existence of such band replicas is an indication of neither a hybridization between the layers nor of a moiré physics.

With the twisted BL WSe₂/graphite sample structures, a variety of events could occur. ARPES is a surface-sensitive technique; and probing the bottom layer buried in the same sample structure is challenging. In typical ARPES experiments, the photoexcited electrons have a mean free path of a few Angstrom ($\approx 1 \text{ \AA}$ - 20 \AA). As a result, even if the X-ray beam penetrates deeper into the crystal, the elastic photoelectrons originate primarily from the first layer; in our case, the thickness of one monolayer of WSe₂ is ~ 0.9 nm. Another possibility is that the photoexcited electrons from the graphite layer during their transmission towards the sample surface are diffracted by the bottom WSe₂ monolayer and could be further diffracted by the top monolayer of WSe₂ as explained earlier, leading to first and second order copies.

5.2.5 Visualization of the SL features in twisted BL WSe₂

ARPES studies are often limited to mapping a limited portion of the SBZ, and probing dispersions simultaneously in both the first and the second SBZ is not performed routinely. Since the parallel momentum k_{\parallel} depends on the emission angle θ and kinetic energy E_{kin} as $k_{\parallel} = \sqrt{\frac{2m}{\hbar^2} E_{kin}} \sin \theta$, there are often technical limitations in reaching large enough θ at low E_{kin} , or the required resolution at large E_{kin} . The size of the SBZ depends on the lattice constant a as $2\pi/a$; therefore, for many materials, one needs to reach $k_{\parallel} \simeq 2 \text{ \AA}^{-1}$ to map the second SBZ, and this is, for example, out of reach using a helium discharge lamp with

the He I line at $h\nu \simeq 21.2$ eV. Also momentum microscopes exhibit a limit of the maximum parallel momentum at higher E_{kin} [173], which depends on the high voltage applied between the sample and the spectrometer. The flexibility of the MAESTRO beamline allows one to use $h\nu = 147$ eV for 3D $I(E_{bin}, k_x, k_y)$ mapping, allowing us to reach the second SBZ of WSe₂ at moderate emission angles of $\theta \simeq 20^\circ$.

Figure 5.16 shows the constant energy surfaces of twisted BL WSe₂/graphite of sample *A* and *B* across first and second SBZs at $E_B \simeq 0.9$ eV, where we were able to visualize the intensity pockets at Γ_0 and Γ_1 contributing from both WSe₂ monolayers that constitute the BL WSe₂ structures. The characteristic features are labeled by the white (Γ_0), red (top flake, Γ_{1top}), and green (bottom flake, $\Gamma_{1bottom}$) dotted color circles, as illustrated in fig. 5.16.

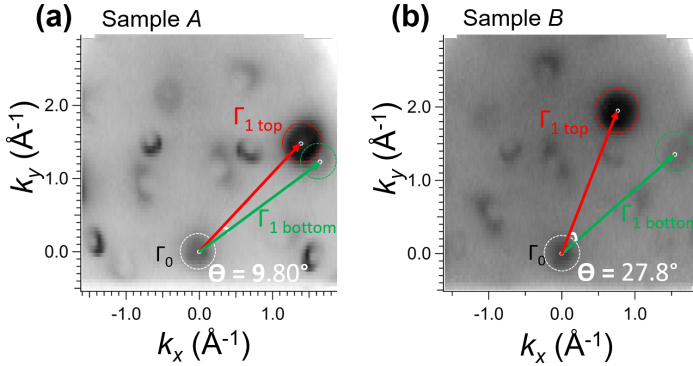


Figure 5.16: Panel (a) and panel (b) present the (k_x, k_y) -dependent constant energy maps taken at $E_B \simeq 0.9$ eV with the determined twist angles of sample *A* and *B*. The red and green arrows connect Γ_0 and Γ_{1top} , Γ_0 and $\Gamma_{1bottom}$ high symmetry points of WSe₂ bilayer structures indicating the twist angle between BL WSe₂.

As a result of observation of the characteristic features from the top and bottom monolayers, we were able to determine the twist angle between the BL WSe₂ of sample *A* and *B*. For doing so, we utilize the band contours around the high symmetry Γ points on CEMs as illustrated in figs. 5.16, 5.17, and 5.18. We mapped out the 3D $I(E_B, k_x, k_y)$ dispersion of each bilayer structures and their respective monolayers. The vectors connecting Γ_0 and Γ_{1top} , Γ_0 and $\Gamma_{1bottom}$ are determined by identifying the centers of the Γ pockets, as illustrated in figs. 5.17, and 5.18. The selection of the k coordinates of the high symmetry

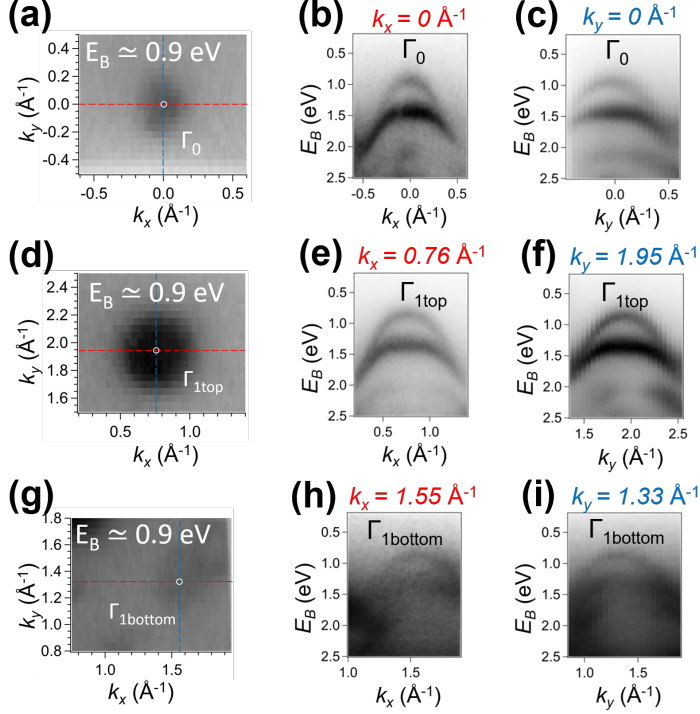


Figure 5.17: Sample *B*: (a,d,g) Constant energy contours at $E_B \approx 0.9$ eV taken around Γ_0 , Γ_{1top} and $\Gamma_{1bottom}$ respectively. (b,c,e,f,h,i) Extracted $E(k_x)$, $E(k_y)$ dispersions at different k_x and k_y cuts performed on all gammas, as indicated by dashed red and blue lines in (a,d,g). A white circle marking in the (a,d,g) indicates the center of for Γ_0 , Γ_{1top} , and $\Gamma_{1bottom}$ retrieved from 3D dataset.

Γ points is based on a comprehensive examination of the complete (E_B, k_x, k_y) -dependent intensity of BL WSe₂ structures. We analyzed $E(k_x)$ and $E(k_y)$ dispersions across all the Γ pockets originating from top and bottom monolayers features in BL WSe₂ datasets of sample *A* and *B* as shown in figs. 5.17 and 5.18. Essentially, we used all the Γ pockets visualized on the CEM from the WSe₂ bilayers datasets. The intensity of the $\Gamma_{1bottom}$ is relatively low in sample *A*, making it difficult to select the k coordinates. For this, we approximated the coordinates from the monolayer dataset. The angle between the red and green vectors corresponds to the twist angles, which we determine as $9.80^\circ \pm 1^\circ$ and $27.80^\circ \pm 1^\circ$ of sample *A* and *B* as shown in fig. 5.16.

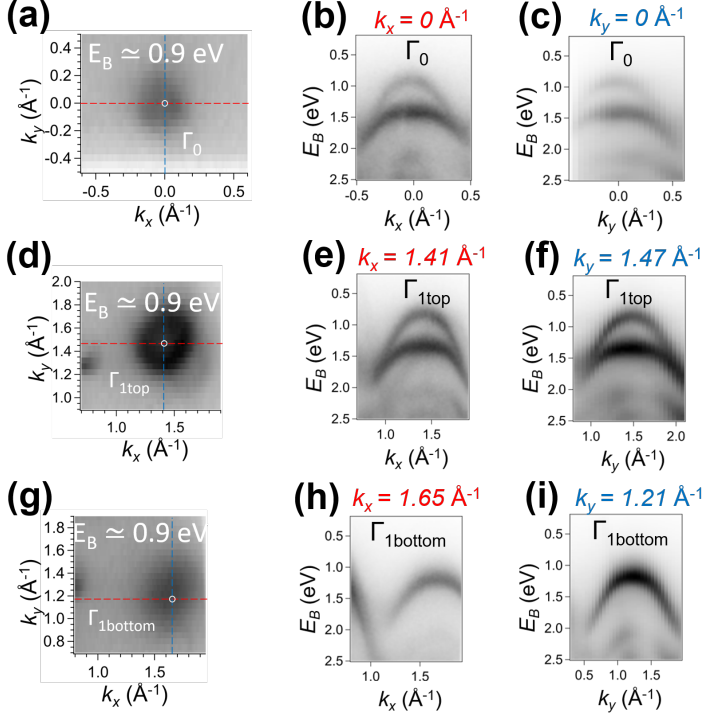


Figure 5.18: Same as fig. 5.17 but for sample A.

5.2.6 Orbital character and VBM estimation

To investigate the orbital character of the bands of the twisted SL and twisted BL WSe₂, the computed eigenstates from the DFT calculation can be projected onto atomic orbitals. The results are shown in fig. 5.19. As can be seen, the valence and conduction bands are primarily made up of p and d orbitals. The local valence band maximum at Γ is made from out-of-plane Se p_z and W $5d_{z^2}$ orbitals, which in the BL hybridize leading to bonding and antibonding-like splitting to the uppermost band and at K_W have a mixture of in-plane $d_{x^2-y^2}$ and d_{xy} orbital characters. This is one of the mechanisms of the direct to indirect band gap transition in few layer TMDCs. In BL WSe₂ this causes energies at the local VB maxima at Γ and K points to differ by ~ 0.2 eV [220], which is different to BL MoS₂, wherein the VBM is clearly at Γ [221].

Figure 5.19 shows the calculated bands structures of a freestanding SL, and aligned AA' stacking derived from bulk 2H polytype, and AA stacking [220,222]

with layers on the top of each other for a BL WSe₂.

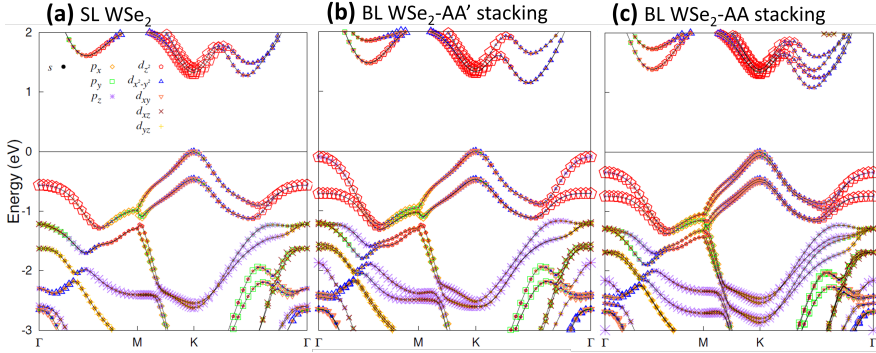


Figure 5.19: Calculated orbital characters for the (a) freestanding SL, (b) AA' (2H)-BL, and (c) AA-BL WSe₂.

Figure 5.20 shows selected maps from the twisted BL of sample *B* measured with *p*- (top row, panels (a-c)) and *s*-polarized light (bottom row, panels (d-f)). As expected from the orbital character, the bands near Γ_0 are more intense for *p*-polarized light, due to their out-of-plane orbital character, fig. 5.20 (b). Conversely, bands at K_W are more pronounced for *s*-polarized excitation, fig. 5.20 (f). The VBM of a 2H-stacked BL is at K_W [46], therefore, in the twisted BL, where the interaction between the layers is weaker, the VBM is also expected at K_W . This is indeed the case, as seen from comparing figs. 5.20 (b) and (f). To determine the bands positions from the ARPES data, we plotted the EDCs of the valence band dispersion at high symmetry Γ_0 and K points of twisted WSe₂ of sample *B*. As shown in fig. 5.20 (g,h), at the Γ_0 and K_W points in BL WSe₂/graphite of sample *B* the local VBs lie respectively at $E_B \simeq 0.95$ eV and $\simeq 0.72$ eV. The splitting between the bands at K_W point is ~ 0.48 eV in agreement with the previous studies [45,46,223], where values between 0.47–0.5 eV were obtained. Due to their shape, these K_W bands are usually referred to as valleys and, as mentioned earlier, are highly spin-polarized in WSe₂ [133].

The bonding-antibonding gap at Γ , that is a signature of interlayer hybridization, persists in our twisted BL WSe₂ microflakes. Its large energy scale of ~ 0.4 eV is in stark contrast to negligible hybridization between these bands near Γ from top and bottom layers, as demonstrated in fig. 5.10. This is likely related to the directional character of the participating d_{z^2} and p_z orbitals that form out-of-plane σ -like-bonds, but any interlayer in-plane hopping between these

out-of-plane orbitals (which can be imagined as π -like) is inhibited. Conversely, the in-plane orbital character at K_W points would allow interlayer in-plane σ -like hopping, but this interaction is inhibited by the large interlayer distance of these orbitals that are primarily located on a transition metal.

Figure 5.21(a) shows the same map as fig. 5.8(d), where the graphite Dirac cone bands are located in the vicinity of the Γ_1 of SL WSe₂. We have focused on this region since the graphite Dirac bands are made from C $2p_z$ and topmost WSe₂ Γ bands from W $5d_{z^2}$ and Se $4p_z$ orbitals that could potentially hybridize,

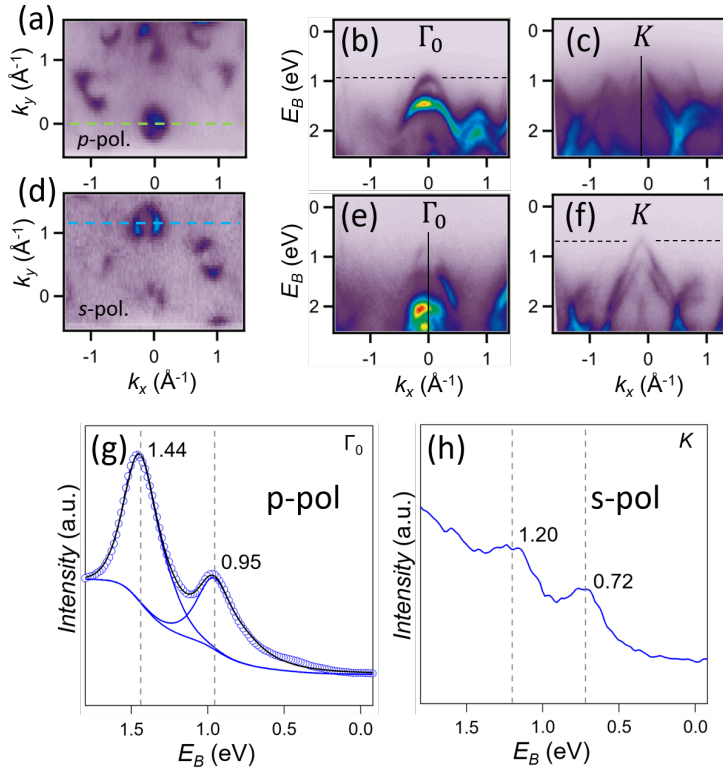


Figure 5.20: Selected maps from the BL of sample *B*. Top row (a-c): CEM at $E_B = 1$ eV for *p*-polarized light. Bottom row (d-f): CEM at $E_B = 1$ eV for *s* polarized light. Green dashed line in (a) shows the momentum trajectory for maps (b) and (e). Blue dashed line (d) shows the momentum trajectory for (c) and (f). Black dashed lines in (b) and (f) indicate the local VBM at Γ_0 and K points respectively. (g,h) EDCs of twisted BL WSe₂ of sample *B* taken at Γ_0 (b) and K (f).

leading to avoided crossings. Previously, such avoided crossings were proposed in monolayer graphene on MoS₂ [224] and in SL MoS₂/graphene [225] through the analysis of the second derivative μ -ARPES spectra. Within our experimental resolution, we observe no sign of such hybridization since the dispersion of the WSe₂ Γ_1 band is unaffected in the region where it crosses with the graphite Dirac band. We took advantage of the "dark corridor" of the Dirac bands [226], where the spectral intensity of one of the Dirac band branches is essentially turned off. This avoids having an incoherent intensity sum of the two bands, allowing to inspect any modification of the Γ_1 band separately.

Figure 5.21(d) displays the $E(k_x)$ map of the Dirac band of graphite at a high symmetry K_{gr} point. Graphite is typically made up of layers of graphene having the Bernal stacking (ABAB), a sequence which is one of the most stable polytypes [227, 228]. In comparison to the ideal two-dimensional graphene, the interlayer interaction in graphite induces the splitting of π bands. The splitting between π bands at K_{gr} is ~ 600 meV. Within the measurement precision of \sim

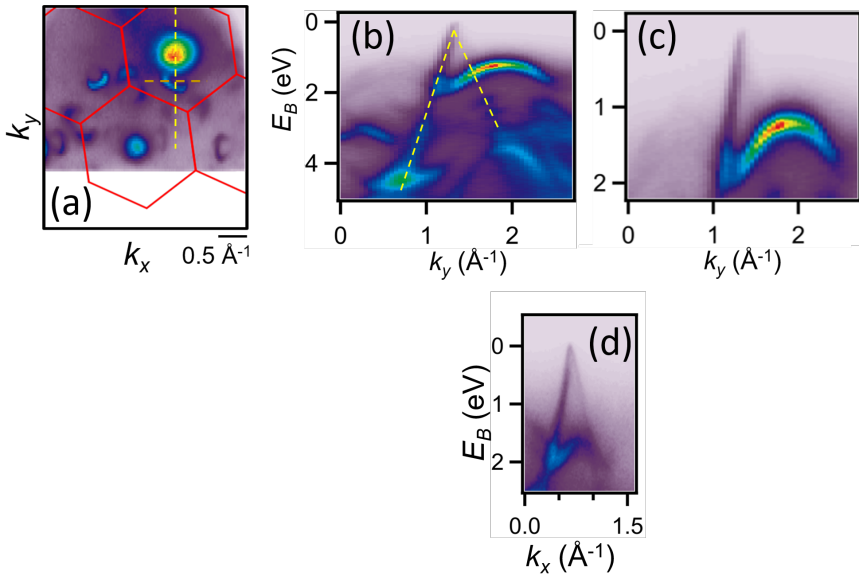


Figure 5.21: Crossing between Γ_1 and graphite bands in sample *B*. (a) CEM at $E_B = 1.2$ eV; yellow dashed line shows the BZ trajectory for maps (b-c). (b) $E(k_y)$ showing the region where graphite and Γ_1 band cross; yellow dashed line depicts the graphite Dirac cone dispersion. (c) Magnified region of the crossing. Orange dashed line presents cut at graphite Dirac cone along k_x (d).

50 meV, the quadratic touching point coincides with the Fermi level indicating a minimal charge transfer between graphite and WSe₂ flakes.

5.2.7 Theoretical calculations

In order to understand our experimental observations on twisted SL, BL WSe₂, our collaborators have carried out density functional theory calculations, including van der Waals interactions. Figure 5.22 shows theoretical calculations for the hetero-bilayer structure (WSe₂/graphene) with 0° and 21.79° hexagonal supercells. The ratio of the experimental WSe₂ to graphene lattice constants is very close to 4/3, with only ~0.5% mismatch. Therefore, we modeled a WSe₂/graphene heterostructure containing a 3×3 WSe₂ and a 4×4 graphene supercell [229]. The 2:1 ratio of these unit cells gives the twist angle of 21.79°, we define it as $(m, n) = (1, 2)$. A single layer of graphene approximates our experimental graphite substrate. Given the presence of heavy elements (W and Se), SOC effects were specifically incorporated.

As shown in fig. 5.22 (a-b) for both aligned (0° twist angle) and twisted (21.79° twist angle) SL WSe₂/graphene, there are only minor differences in band positions, as compared to the freestanding SL WSe₂ (green lines), in particular in the region near the VBM. Figure 5.22 (c) shows a magnified region where SL WSe₂ and graphene bands cross for the case of 0° twist angle, where one can see band crossings without significant hybridization gaps. Figure 5.22 (d) shows a similar region, but for the case of 21.79° twist angle. In this case hybridization gaps of the order of 50 meV can be resolved. This finding is probably related to the band character of WSe₂ at momenta where they cross the graphene band. As shown in fig. 5.19(a), the band character changes from in-plane at the K point into out-of-plane at Γ . In case of the fig. 5.22 (b) the crossing is further from the K point, (as compared to fig. 5.22(a)), suggesting less in-plane character, more hybridization, and larger hybridization gaps. This process is competing with the interlayer distance, which is larger for the twisted SL WSe₂/graphene.

Different stacking sequences in the WSe₂ BL have been considered in previous work [220, 222], however, besides the previously defined AA' and AA , their nomenclature appears inconsistent. SL WSe₂ has three-fold rotation axis C_3 without inversion symmetry, therefore it has polarity in the in-plane direction (along ΓM reciprocal direction). For the bilayer, in the aligned case, there are

two general options: the polarities of the adjacent layers face either in the same direction (such as in the $3R$ bulk polytype) or in opposite directions (the $2H$ bulk polytype). During the natural growth process, the in-plane shift between the layers is naturally adjusted, however, in the twisted structures it becomes an additional parameter. One can also imagine that at very small twist angle, the twisted BL will contain large regions of stackings which differ only by that shift, and that the regions of energetically favorable stacking will become larger due to the atomic relaxation. Following ref. [220] at a small twist angle the structure

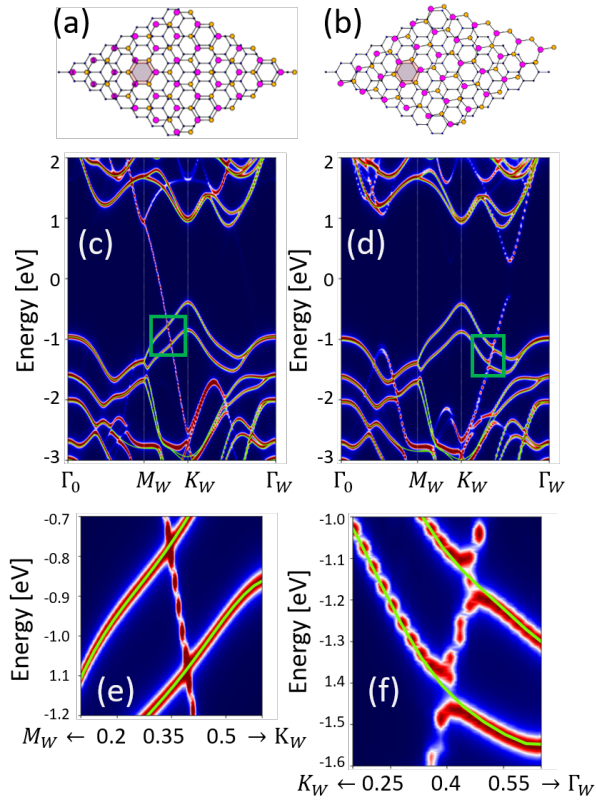


Figure 5.22: Atomic model and theoretical calculations for aligned (a,c) and 21.79° twisted (b,d) SL WSe_2 on graphene. The theoretical band structure is deconvoluted onto the Brillouin zone of the freestanding SL WSe_2 . (e) and (f) show magnified areas of the green boxes in (c) and (d), respectively. Green lines (in all panels) show the band structure of a freestanding SL WSe_2 , for comparison.

where the polarities of the layers are (nearly) aligned contains regions of *AA*, *AB*, and *BA* stackings [230]. Out of these the *AA* is an energetically unfavorable stacking where layers are on top of each other, while *AB* and *BA* are two variants of the 3R-polytype stacking. Similarly, for the anti-aligned polarities of the layers, according to ref. [220] the small twist angle structure contains regions of *AA'*, *A'B*, and *AB'* stackings, out of which *AA'* corresponds to 2H, while the other two are not typical in the bulk crystals.

We focus on *AA* and *AA'* stackings as starting points for modeling twisted bilayers, with the *AA'* stacking being the same as in the most stable 2H polytype, and *AA* being the two layers directly stacked on top of each other. Starting with *AA* we considered situations when twisting is either around the center of the W-Se hexagon, around the W atoms, or around Se atoms (considering the top view of a BL). Starting with *AA'* we only considered twisting around the center of the W-Se hexagon. We define (m, n) as the number of the unit cells from the top and bottom WSe₂ layers, respectively, that make up the moiré unit cell. This relates to the twist angle θ through $\cos \theta = \frac{1}{2} \frac{m^2+n^2+4mn}{m^2+n^2+mn}$.

We have relaxed the twisted BL WSe₂ structures defined above for several twist angles with the resulting total energy differences and structural information provided in Table 5.1. To reduce the complexity, SOC was not included in these calculations. For the aligned layers, we find the difference δE between the most energetically favorable and unfavorable stackings, *AA'* and *AA* to be 40.25 meV per W atom in the unit cell. Since the twisted structures contain regions of favorable and unfavorable stackings, their expected energy should be approximately half way between those of aligned *AA'* and *AA*. This is indeed the case, however, as the twist angle becomes small, the energies become lower, probably due to extended regions of favorable stacking. The average interlayer distance \bar{d}_{W-W} is larger for larger twist angles, which is again probably related to the larger areas of energetically-favorable stacking for smaller twist angles. Accordingly, the corrugation Δd due to the moiré pattern is smaller at larger twist angles.

We also investigated the energy differences $\Delta E_{t,hex}$ for the layers where the starting stacking is *AA* or *AA'*. We find that the difference in energy is smaller for larger twist angles, with the structures starting from *AA'* always being more stable. At small twist angles it likely reflects the energy differences between 2H (*AA'*) and 3R-like stackings, which form the areas of favorable stacking.

Table 5.1: The calculated total energies and interlayer distances of twisted BL WSe_2 for the stacking sequence where twisting is around the center of in-plane WSe_2 hexagons. In these calculations SOC was not included. N_W is the number of W atoms per moiré unit cell. ΔE is the energy difference between the AA stacking rotated around the center of the hexagon, as compared to the aligned AA ($\theta = 0$) stacking; $\Delta E = E(AA) - E_{t,hex}(AA)$. $\Delta E_{t,hex} = E_{t,hex}(AA') - E_{t,hex}(AA)$ is the energy difference, between the twisted AA' and AA stackings with the rotation axis at the center of the hexagon. The energies are given in meV per W atom. The structural parameters (in \AA) are given for AA' stacking twisted around the center of the W -Se hexagon: \bar{d}_{W-W} is the average interlayer out-of-plane distance (along z -axis) between W atoms, while Δd is the maximum out-of-plane difference of W atom positions within the layer, it represents the corrugation due to formation of the moiré pattern.

θ	N_W	(m, n)	ΔE	$\Delta E_{t,hex}$	\bar{d}_{W-W}	Δd
21.79°	14	(2,1)	18.50	-0.04	6.839	0.003
13.17°	38	(3,2)	18.73	-0.10	6.842	0.017
7.34°	122	(5,4)	20.20	-0.43	6.814	0.077
6.01°	182	(6,5)	21.04	-0.58	6.813	0.104
3.89°	434	(9,8)	22.56	-0.76	6.768	0.132
0	2	(1,1)	0	-40.25	6.547	0

Figure 5.23 (a-c) shows the arrangement of BZs and theoretical band dispersions for BL WSe_2 at the twist angle 13.17° with twisting around the center of the W -Se hexagon starting with the AA' stacking. Similarly, (d-f) presents the situation for 21.79° . Therefore, in absolute terms related to the experimental results of figs. 5.8 and 5.9, the twist angle is $\theta = 60^\circ - 13.17^\circ(21.79^\circ) = 46.83^\circ(38.21^\circ)$. Our actual experimental system consists of BL WSe_2 /graphite, however, we omit graphite to reduce numerical complexity. The bands are deconvoluted onto the BZ of one of the layers. As compared to the bands of a 2H BL WSe_2 shown by green lines (see also fig. 5.19(b)), the difference near the VBM is mainly in the reduced bonding-antibonding splitting of the bands at Γ as indicated by the white rectangle in fig. 5.23(b). Figure 5.23 (c) shows the details of the region where anticrossing hybridizations are observed, with the local gaps of the order of 50 meV. We observed the similar results for the other twist angle 21.79° .

Both studied twisted BL WSe_2 samples exhibited a doubly split band at the Γ point, similarly to the non-twisted case. For both theoretically studied twist angles of $\sim 21.79^\circ$ and $\sim 13.17^\circ$ the global VBM is located at the K_W point, and the splitting of the doublet at Γ remains the same within our experimental

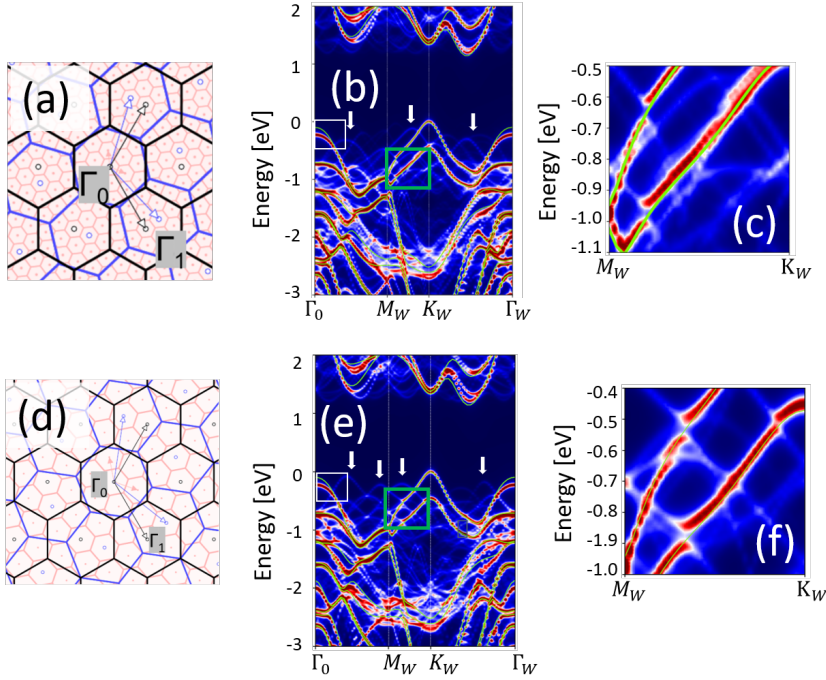


Figure 5.23: Theoretical calculations for twisted BL WSe₂ at two twist angle $60^\circ - 13.17^\circ (21.79^\circ) = 46.83^\circ (a-c)$ (38.21°) (d-f). (a,d) Black and blue lines depict BZs of the two SLs and the network red lines the moiré BZs of the twisted layers. (b,e) Band structure unfolded onto the BZ one of the SL WSe₂. (c,f) Magnified region depicted by the green rectangle in (b). For comparison, green solid lines show the bands for the 2H BL WSe₂.

accuracy.

In our photoemission experiments, we studied twisted BL WSe₂ samples, as discussed in previous sections, wherein a change in the alignment between two lattices induces a moiré pattern. The periodicity of the moiré pattern leads to a periodic change in the coupling between the layers. The potential landscape within the moiré pattern gives rise to a mini-Brillouin zone, a phenomenon first observed in van-der-Waals materials with twisted graphene bilayers [231], and results in the formation of moiré Bloch bands. We expected to map the moiré bands, but we did not observe any. On the other hand, the presence of moiré bands may easily be demonstrated in theoretical calculations. They are clearly recognizable, indicated by white arrows in fig. 5.23(b,e), since they are prominent in the vicinity of high symmetrical points at the topmost valence

bands. Depending on the formation of the moiré superlattice, the band positions of the moiré bands vary for different twist angles.

No indication of flat bands is present in our experimental ARPES maps, and our calculations for twisted BL WSe₂ do not indicate any flat bands that are split-off from the band structure of separate SLs. For moiré cells larger than in our calculations, recent calculations by Kundu et al. [220] identify flat bands over the ~ 50 meV energy scale for twist angle up to 5.1° . Small twist angles lead to large moiré unit cells, and to large areas of relatively well-defined stacking areas which exhibit significantly shifted band structures in the vicinity of Γ , as shown in fig. 5.19(b-c). Our smallest experimental twist angle of $\sim 10^\circ$ for BL WSe₂ of sample *A* is too large to allow for formation of experimentally observable gaps between the bands, and in the experimental data small anticrossings might be smeared out. So far no interlayer hybridization gaps have been reported in μ -ARPES from twisted TMDCs, and the only potential indirect indication of the formation of a moiré potential is through the observation of multiple Dirac copies near the K_{gr} in the graphene/WS₂/WSe₂ heterostructure [232].

5.3 Conclusion

In summary, we have described and critically examined properties of μ -ARPES spectra from several twisted WSe₂ flake samples on graphite substrates. We established that valence bands maximum of WSe₂ lies at K_W in all studied microstructures. Hybridization effects between twisted BL WSe₂ are manifested in the bonding-antibonding splitting at Γ that is readily observed in the experiment, but does not translate into further emergent interlayer hybridization gaps. Such hybridization gaps are also not observed in the studied twisted SL WSe₂/graphite. The Fermi level electrons emitted into the K_{gr} points diffract when passing through the WSe₂ overlayer, forming sharp replicas whose positions can be predicted by combining the reciprocal vectors of WSe₂ and graphite. The characteristic features derived from the monolayers involved in the formation of the twisted WSe₂ BLs are visualized on the constant energy contours. By utilizing the band contours around the high symmetry Γ points on CEMs, the twist angle between BL WSe₂ is determined. Experimental findings are supported by accurate theoretical DFT modeling with the inclusion of vdW forces, which suggests that forming of hybridization in WSe₂/graphite system sensitively depends on the orbital character of the WSe₂ at the crossing with the graphene Dirac cone band.

This work paves the way for designing future experiments on twisted TMDC bilayers at smaller twist angles, which would enable imaging their fascinating predicted properties such as topologically non-trivial flat bands.

Chapter 6

Circular Dichroism in the Bandstructure of Twisted SL, BL, and Bulk WSe₂

In an ARPES experiment, changing the photon polarization from non-polarized light to linearly or circularly polarized light has a significant impact on the measured photocurrent. Depending on different photon polarizations, dipole selection rules result in different atomic cross-sections for the interaction of polarized light and matter. ARPES setups with a circularly polarized light source are seen to be an ideal instrument for measuring information on valley-resolved properties in two-dimensional systems. This section will provide a brief overview of the circular dichroism in ARPES studies of twisted SL, twisted BL, and bulk of WSe₂ flakes.

6.1 Circular dichroism in the angular distribution of photoelectrons

Circular dichroism (CD) is defined as the difference in response to left-handed and right-handed circularly polarized light. The selective absorption of left-handed circular polarization (LCP) and right-handed circular polarization (RCP) by chiral compounds is well-recognized [233]. X-ray magnetic circular dichroism (XMCD) studies, in which the difference spectrum of two X-ray absorption spectra is obtained in a magnetic field, also employ dichroic signals. This approach enables researchers to examine the magnetic characteristics of an atom and molecule and was first observed for the K-edge of iron [234]. It is also possible to acquire information on orbital and, more indirectly, spin magnetic moments. These measurements require the presence of two basic interactions:

spin-orbit coupling, which couples the electron spin and orbital angular momentum, and exchange splitting, which arises from the interaction between the electron spins [235]. In CD, dipole selection rules govern the optical transitions in matter

$$\Delta l = \pm 1, \Delta m_l = 0, \pm 1 \quad (6.1)$$

For example: In ferromagnets as reported in ref. [234], the XMCD response of the electrons originating from the $2p_{1/2}$ state has 100% polarization when excited by a photon with positive helicity, whereas electrons occupying the $2p_{3/2}$ state have -50% polarization. However, it is important to note that the polarization values can vary depending on a variety of experimental parameters, including the energy and polarization of the X-rays, the sample orientation, and the details of the experimental setup. For the same allowed transition, there is an asymmetry between left and right helicities, because different photon energies are required for the excitation [236]. Moreover, significant CD signals are observed in 3d transition metals at the $L_{2,3}$ edge transition given that the d-electrons are the primary carriers of magnetism. Details could be found in ref. [237]. The mentioned technique is not straightforward to apply to the band electrons, because the atomic model is not a reasonable approximation here as it is in case of core levels since the electrons orbitals are perturbed [238, 239].

Even in the absence of a chiral sample and a magnetic field, the dichroism effect can be seen. The light and matter-coupled system with a defined handedness is the important need for a dichroic signal. The experimental geometry can induce chirality even if the sample is not chiral. In theory, every crystal may exhibit CD effects if the direction of photon photoelectron momentum \vec{k} , and surface normal \vec{n} and photon impact \vec{q} are non-coplanar [240].

In ARPES experiments, the difference between photoemission spectra measured by LCP and RCP polarized light is used to calculate the CD signal. The detected signals are referred to as CD-ARPES. Polarization-dependent measurements can reveal symmetry details about the initial states depending on the polarization of the incident light [69, 241]. For instance, initial states derived from a d orbital, d_{z^2} orbital, can exhibit substantially different ARPES intensities. Recently, there has been a lot of interest in employing CD-ARPES to assess certain initial state features, such as OAM [242, 243] or the Berry curvature [244]. Circular

dichroism observed by photoemission is sensitive to the orbital angular momenta of the electronic states and can be used to gather critical information about the electronic structure [245]. In sample systems without inversion symmetry [246–249], such as solid surfaces and monolayers of transition metal dichalcogenides [250–252], the presence of OAM plays a critical role in determining the spin-splitting observed at K and K' in the BZ [105, 133, 250]. These inequivalent K valleys lead to a valley Hall effect, which had been understood in terms of Berry curvature [253–257]. Symmetries at these valleys may cause the Berry curvature sign to change from K to K' valleys in BZ. [250–252, 254, 258–260].

In CD-ARPES, the spectral asymmetry as a function of binding energy is described by

$$A(E, \vec{k}) = \frac{I^+(E) - I^-(E)}{I^+(E) + I^-(E)}$$

where the photoemission intensities with positive and negative light helicities are represented by I^+ and I^- , respectively.

It is critical to comprehend the origin of the CD data to make a meaningful interpretation. The many factors that might induce circular dichroism, as mentioned above, may superimpose onto each other and complicate the interpretation of the collected data. The most accurate theoretical treatment of CD-ARPES is based on relativistic band structure calculations and one-step model photoemission calculations [261]. Spin-orbit coupling is likely to play a significant role. However, it is undoubtedly not the sole component, as graphene also exhibits a significant CD effect [262, 263]. Other parameters that influence the CD signal include the geometrical configuration [240], and photon energy [264].

6.2 Circular dichroism in WSe₂

In this work, CD-ARPES mapping of twisted SL, twisted BL, and bulk WSe₂ has been demonstrated. All the CD-ARPES measurements were carried out at the NanoESCA endstation at Elettra and data were taken with left-handed and right-handed circularly polarized 40 eV photon light at $T \sim 80\text{K}$ [265, 266].

As previously mentioned in chapter 3, all the samples were fabricated by mechanical exfoliation and dry transfer technique in collaboration with Dr. Bernd Beschoten's group. All samples were brought to the NanoESCA beamline in

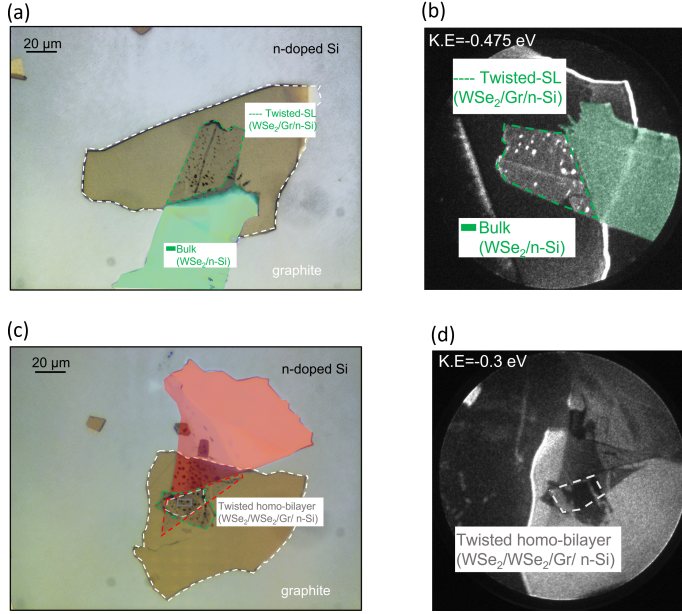


Figure 6.1: (a,c) are the optical micrographs of twisted SL and twisted BL of WSe₂ placed on graphite, and the entire sample structure is lying on the top of n-Si. (b,d) are the PEEM images of the samples taken with a Hg lamp, where, twisted SL, twisted BL and bulk WSe₂ flake are represented by the dotted green and gray lines and shaded green color region, respectively.

argon-sealed gel boxes. Prior to the CD-ARPES measurements, the samples were annealed at 300°C. The microscopic control of the beam position and real-space imaging capabilities at the NanoESCA endstation make it possible to identify and measure different regions at the sample surface. The homogeneous region on the sample surface was identified by using the PEEM in real space mode with a Hg lamp as an excitation source. Furthermore, a k-space microscope scans the reciprocal space without rotating the sample; thus, precisely the same region is probed during the entire experiment, and the parallel momentum scale is imaged faithfully, an advantage over traditional ARPES setups.

The SL and BL of WSe₂ are embedded in different samples, unlike previous ones because, as shown in fig. 6.1(c) following the overlap of WSe₂ monolayer to produce twisted BL, the region belonging to the SL flake is extremely small, making measurement difficult due to the beam spot, which is in the order of $\sim 15 \mu\text{m}$. Figure 6.1 shows the optical and PEEM images of the twisted SL and twisted

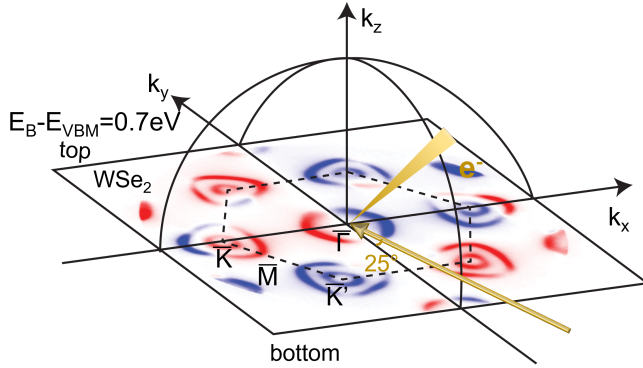


Figure 6.2: Scheme of the experimental setup: a circularly polarized light (40 eV) is focused onto the bulk WSe₂ crystal at an angle of incidence of 65° with respect to the surface normal, ejected photoelectrons are detected by the momentum microscope. The dashed contour represents the two-dimensional SBZ of 2H-WSe₂ with the high symmetry points (\bar{K} , $\bar{\Gamma}$, \bar{K}' , \bar{M}).

BL of WSe₂ flake samples. The lateral size of twisted SL WSe₂/graphite/n-Si: sample *C* and twisted BL Wse₂/graphite/n-Si: sample *D* is in the order of $\approx 15 \mu\text{m}$. Each sample consists of different regions with different twists between the atomically thin flakes.

6.2.1 Bulk-WSe₂

Figure 6.2 shows the layout of the experimental geometry of the NanoESCA momentum microscope. The momentum image shows the electronic states at a constant energy $E_B - E_{VBM} = 0.7 \text{ eV}$. Photoelectrons are collected simultaneously over the entire solid angle above the sample, allowing efficient measurements. The experimental geometry is critical for the observation of a dichroic effect. In our experimental scheme for bulk WSe₂, light is aligned with the crystal mirror plane, which is along Γ - M high symmetry direction.

Due to optical selection rule criteria, circularly polarized light with either left or right-handed circularity can provide different photoemission intensities, providing information about the orbital angular momentum of the material's electronic bands. The CD-ARPES has been widely used to study the modulation of the photoemission transition matrix element [267–270]. Moreover, in certain cases, CD-ARPES has been proposed to be related to the momentum-resolved orbital polarization of the local Berry curvature [271].

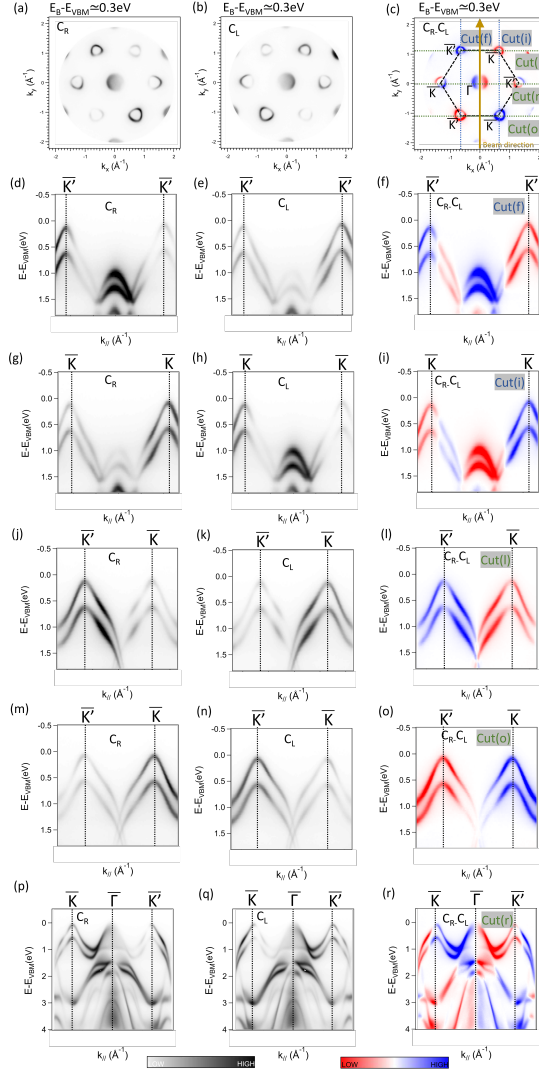


Figure 6.3: Bulk WSe₂: Panels (a,b) show ARPES maps at $E_B - E_{VBM} = 0.3$ eV taken by RCP and LCP incident light respectively. The CD signal is depicted in panel (c), with the hexagonal BZ represented by a black dotted hexagon and the high symmetry spots are marked. The energy-momentum cut along vertical ($\overline{K'}-\overline{K'}$, $\overline{K}-\overline{K}$) and horizontal cuts ($\overline{K'}-\overline{M}-\overline{K}$, $\overline{K}-\overline{\Gamma}-\overline{K'}$) are measured by RCP and LCP incident light utilizing 40 eV photons is shown in panels (d,g,j,m,p) and (e,h,k,n,q). Panels (f,i,l,o,r) correspond to CD-ARPES signals along the $\overline{K'}-\overline{K'}$, $\overline{K}-\overline{K}$, $\overline{K'}-\overline{M}-\overline{K}$, and $\overline{K}-\overline{\Gamma}-\overline{K'}$ cuts, respectively. Vertical and horizontal cuts are indicated by dotted green and blue lines, respectively.

CD-ARPES signals are mapped in momentum space with an intensity corresponding to the difference between the intensity taken by RCP (C_R) and LCP (C_L), respectively, $I_{CD} = C_R - C_L$. Figure 6.3(a,b) represents the constant energy ARPES maps taken with the RCP and LCP incident light at a binding energy (E_B) of 0.3 eV and fig. 6.3(c) shows the I_{CD} signals.

As discussed in chapter 1, a single layer of WSe₂ exhibits a broken inversion symmetry; however, in the bulk form of 2H-WSe₂, the adjacent layers are rotated 180° with respect to each other, restoring the inversion symmetry. Since CD-ARPES is a surface-sensitive experiment, the top layer contributes the majority of the signal compared to the following sublayers in the actual experiments.

In bulk 2H-WSe₂, layers are stacked such that $K(K')$ of one layer is at the same momentum location as $K'(K)$ of the following layer. As a result of the recovered inversion symmetry, spin and valley symmetries are restored, and any valley sensitive signal should vanish [105, 251, 272, 273]. The in-plane nature of the orbital character of the electronic states around K and K' , on the other hand, strongly suppresses interlayer hopping along the c axis and makes them quasi-two-dimensional [272, 274]. Nonetheless, the spin-split nature, as well as the valley physics of each layer, is preserved. As already mentioned, the signal predominantly comes from the topmost layer in CD-ARPES; which has broken inversion symmetry and this is related to the “hidden spin polarization” [275].

As illustrated in fig. 6.3, the ARPES and CD-ARPES data are plotted along vertical ($\overline{K'}-\overline{K'}$, $\overline{K}-\overline{K}$) and horizontal ($\overline{K'}-\overline{M}-\overline{K}$, $\overline{K}-\overline{\Gamma}-\overline{K'}$) directions indicated by blue and green dotted lines in fig. 6.3(c). We observed that in the vertical cuts as shown in fig. 6.3(f,i), that the energy dispersion in both spectra looks to be symmetric. Yet, the intensities vary strangely, indicating that there is no symmetry. This is related to the symmetry breaking by the experimental geometry and by the lack of the x - z (M_y) mirror plane. However, following on with a close interpretation of the CD data obtained from the $\overline{K'}-\overline{K'}$ (see fig. 6.3(f)) and $\overline{K}-\overline{K}$ (see fig. 6.3(i)) cuts reveals striking similarities, if the colors of one of the images are inverted. Here, the CD-ARPES signals retrieved from the K and K' valleys are nearly identical, but their signs, which the valley index should dictate, are opposite. Thus, the sign is found to be the same for the two spin-split bands most likely because they have the same OAM [276]. Accordingly, one can see that spin-split \overline{K} bands of WSe₂ invert colors on the left/right sides in horizontal cuts as shown in fig. 6.3(l,o). In this case the CD-

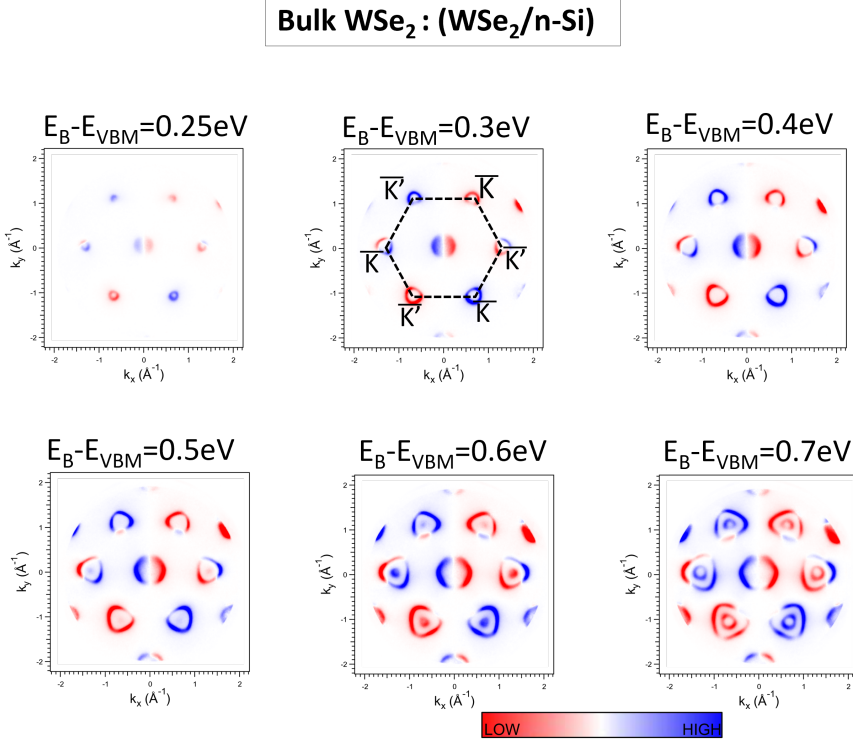


Figure 6.4: Circular dichroism in momentum space at various energies $E_B - E_{VBM}$ measured for the bulk WSe₂. The radius of each constant dichroism map corresponds to 1.9 \AA^{-1} . The SBZ of WSe₂ is represented in $E_B - E_{VBM} = 0.3 \text{ eV}$, with the high symmetry points designated by \bar{K} and \bar{K}' .

APRES signal is spin-independent, because CD-ARPES is sensitive to OAM but not to spin-polarization. This suggests that the CD-ARPES data reflect characteristics of the electronic structure that are opposite, but symmetric at the \bar{K} and \bar{K}' points of the SBZ of 2H-WSe₂. Moreover, this is attributed to the signatures of the momentum-resolved orbital moment contribution in two-dimensional materials [271, 277, 278].

Recently, following the analysis of Schueler et al. [271], Cho et al. attempted to relate the CD-ARPES from the WSe₂ to a hidden Berry curvature and OAM experimentally [279, 280]. Our findings are remarkably similar to theirs. However, we note that extrinsic contributions to dichroism can come in via experimental geometry-induced symmetry breaking [56]. It is difficult to disentangle the intrinsic and extrinsic contributions to the dichroic signal, yet it is critical for

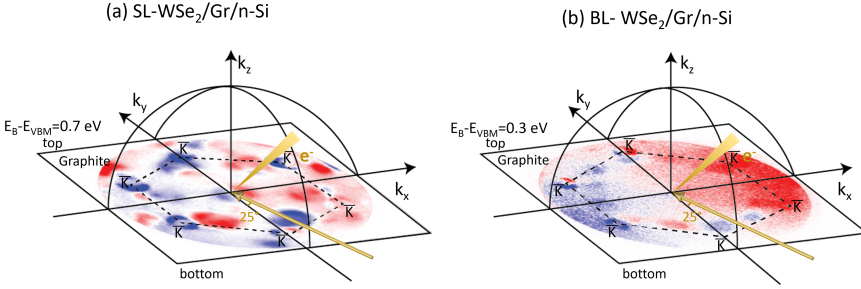


Figure 6.5: Panel (a) and panel (b) show the scheme of the experimental setup of SL and BL WSe₂/graphite/n-Si. A circularly polarized light (40 eV) is focused at a 65° angle of incidence with respect to the surface normal onto the graphite \bar{K} bands. The dashed contour represents the SBZ of graphite with the high symmetry \bar{K} points.

gaining meaningful knowledge about initial states.

Fig. 6.4 shows CEM maps at various binding energies near the VBM for bulk WSe₂. One can observe on experimentally recorded CEMs, that the photoemission intensity around each \bar{K} and \bar{K}' valley is strongly anisotropic, resulting in “croissant”-shaped patterns. This has recently been explained as the result of the in-plane interference effect between photoelectrons emitted from transition metal d-type orbitals [281].

6.2.2 Twisted SL and BL WSe₂

We also performed CD-ARPES measurements on twisted SL and twisted BL WSe₂ lying on a graphite flake, which are labeled as sample *C* and sample *D* (see fig. 6.1). We had shown that the twist angle between SL WSe₂ lattice and graphite lattice in sample *C* is $\theta = 17.2^\circ$ in chapter 5. The details of applied method can be found in section 5.2.4 and [219].

In CD-ARPES measurements of twisted SL WSe₂/graphite and twisted BL WSe₂/graphite sample structures, the graphite K points are aligned along the beam direction, i.e., from bottom to top of the momentum maps, as seen in fig. 6.5. We measured the 2D momentum maps from the twisted single layer and bilayer of WSe₂ at different binding energies, as shown in fig. 6.6. Features of both graphite and WSe₂ are clearly visible in constant energy contours from SL and from BL; there is a contribution from both monolayers on the momentum maps. However, the features of bilayer WSe₂ are not as sharp as those of the

monolayer sample structures.

We compared our SL and BL WSe₂/graphite experimental results to the one-step photoemission calculations based on fully relativistic density functional theory. The theoretical calculation is implemented in the fully Korringa-Kohn-Rostoker (KKR) method. The theoretical calculations were performed by Prof. Jan Minar and Dr. Jakub Schusser from the University of West Bohemia, Czech Republic. In our one-step photoemission calculations, we calculated constant energy maps of WSe₂ monolayers at five different binding energies (0.3 eV, 0.4 eV, 0.5 eV, 0.6 eV, 0.7 eV) at two different angles (0° and 24.3°) with respect to the light incidence, without the contribution of graphite. The estimated photoemission signal on each constant energy map is layer-resolved and incorporates all matrix element effects related to experimental geometry, photon energy, and polarization state influence [218, 282, 283].

As previously described, the combination of the broken inversion symmetry within each layer and the strong spin-orbit coupling, results in unusual momentum-space orbital patterns. As shown in fig. 6.6, panels 6.6(a,c) show the experimentally measured CD photoemission intensity, and panels 6.6(b,d) show the calculated CD photoemission intensity.

We considered a 0° rotated WSe₂ monolayer to make the comparison with twisted SL WSe₂/graphite. In our experimental data set as shown in panel 6.6(a), we observed that at the Γ points at all the energy contours the dichroic signal is symmetric, and the valence bands around each K/K' valley show the same dichroic signal, which are the same negative/positive (red/blue) intensities being in qualitative agreement with our theoretical results (see panel 6.6(b)) marked by black arrows on the constant energy maps for selected regions.

To compare with the experimental CD-ARPES data for twisted BL WSe₂/graphite, we used two isolated computed WSe₂ monolayers, which are rotated by 0° and 24.3° twist angles. To generate a reasonable dichroic signal from the theoretical calculations, we performed an addition separately on respective C_{plus} datasets and C_{minus} datasets corresponding to the differently rotated layers. We are dealing here with two WSe₂ monolayers, so to make good visualization of which layer is at the top and which one is at the bottom, we multiplied the data set by 0.9 factor to adjust the transparency such that the top layer is 90% weighted and the bottom layer is 10% weighted. Thus, the signal from the top layer is more intense than the bottom layer. Finally, using $CD = C_{plus} - C_{minus}$,

we generate the CD-ARPES signals.

As can be seen in panels 6.6(c,d) for twisted BL WSe₂, there are some similarities between theory and experiment. The dichroic signal at the Γ bands is the same in terms of symmetry, which shows red/blue intensities indicated by black arrow

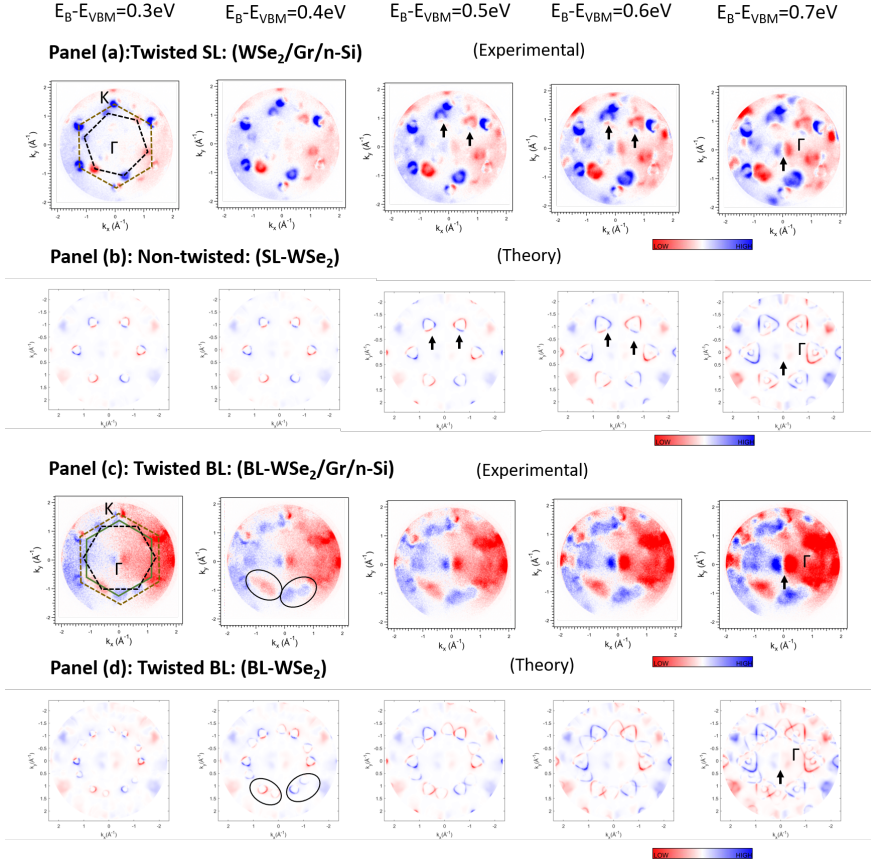


Figure 6.6: Comparison between experimentally measured and theoretically calculated CD-ARPES: Panel (a, c) show experimental observation on twisted SL, twisted BL WSe₂/graphite structures, circular dichroism in momentum space was measured at various energies. On constant energy maps at $E_B - E_{VBM} = 0.3$ eV, the BZ for SL, BL WSe₂ is represented by green and dotted black hexagons with high symmetry points (Γ , K), whereas brown dotted lines represent the BZ for graphite. All the corners of the BZs represent the K points. Panel (b, d) shows the theoretical calculations on non-twisted SL WSe₂ and twisted BL WSe₂ layers. The radius of each constant dichroism map corresponds to 1.9 \AA^{-1} . Black arrows and ellipses indicate similarities between theory and experiments.

on $E_B - E_{VBM} = 0.7$ eV. Additionally, in our experimental data of twisted BL WSe₂/graphite, the dichroic signals coming from the K valleys are less sharp, but we could observe the hint of red and blue intensities quite well. As shown in fig. 6.6, $E_B - E_{VBM} = 0.4$ eV presents the energy contour showing the different color intensities belonging to the individual WSe₂, which is quite comparable with our experimental results marked by ellipses on selected K points of WSe₂ BZs. Furthermore, at higher binding energies in the experimental data, the dichroic signals from the K bands are not clear; however, we observe the well-defined blue and red intensities scattered on the constant energy map, which could be seen in approximately the same regions as in our theory calculations (see panel 6.6(d)).

Furthermore, we plotted four energy-momentum cuts along with the high symmetry directions of the WSe₂ SBZ for twisted SL WSe₂/graphite as shown in fig. 6.7, as we did for bulk WSe₂ (fig. 6.3). We observed that the top surface layer in bulk WSe₂ has some CD-ARPES characteristics of a SL WSe₂. On the other hand, for the twisted BL WSe₂ (sample D), the dichroic signals are different from the bulk WSe₂ or SL WSe₂, as depicted in fig. 6.8. In twisted BL WSe₂, we observed the features contributing from both WSe₂ layers and graphite at the constant energy map $E_B - E_{VBM} = 0.2$ eV as shown in fig. 6.8(c) indicated by green and black hexagons with high symmetry points K , K' , Γ . This is shown in detail in the previous chapter.

In our experimental geometry, the photon beam has been oriented along the graphite K points, as depicted on the constant energy map fig. 6.5(c) and fig. 6.8(c). Our sample structure is composed of two WSe₂ layers, with the top WSe₂ layer BZ nearly along K point of the graphite lattice. Moreover, for the bottom WSe₂ layer, there are dichroic features, which behave as if they have aligned along the $M-\Gamma-M$ axis, which is the crystal mirror plane of the corresponding WSe₂ SL along the beam, as illustrated by green and black hexagons in fig. 6.8(c). The $M-\Gamma-M$ high symmetry direction lies within the “reaction plane” for that SL, meaning that the light propagation vector and $M-\Gamma-M$ lie in the same plane. We plotted five energy-momentum dispersion maps along with the high symmetry directions, with two $K'-K$ horizontal cuts belonging to one WSe₂ layer, $K-K$, $K'-K'$ belonging to the other WSe₂ layer and $K/M-\Gamma-K'/M$ cut sharing M points of one WSe₂ layer and K , K' points of another layer.

We observed in fig. 6.8(f), which is measured along with $K/M-\Gamma-K'/M$ cut, that

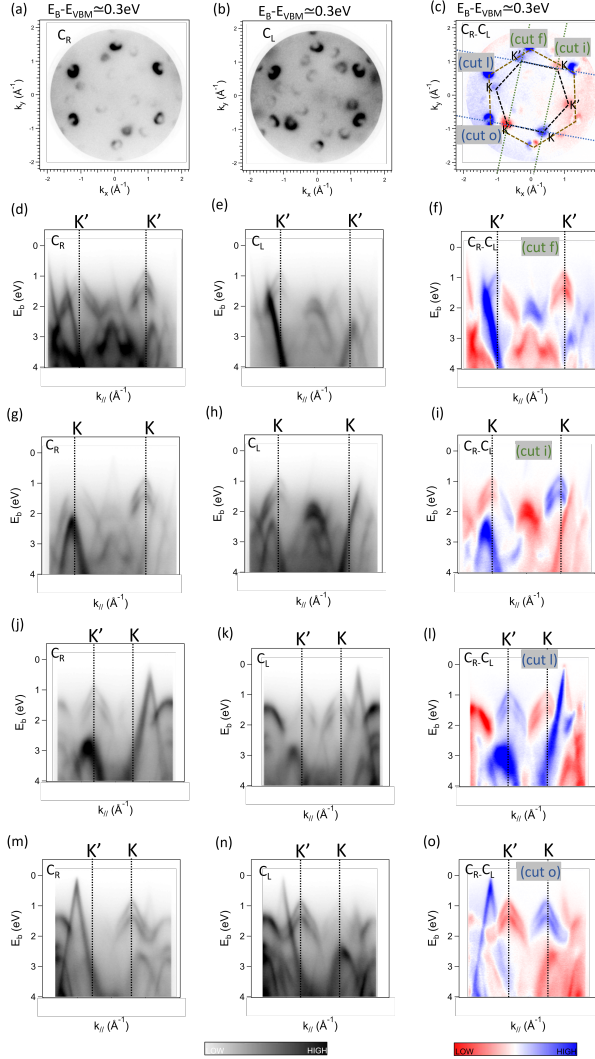


Figure 6.7: SL WSe₂/graphite: Panel (a,b) show ARPES maps at $E_B - E_{VBM} = 0.3$ eV taken by RCP and LCP incident light respectively. The CD signal is depicted in panel (c), with the hexagonal BZ represented by a black dotted hexagon and the high symmetry spots are marked. The energy-momentum cut along vertical ($K'-K', K-K$) and horizontal cut ($K'-M-K$) are measured by RCP and LCP incident light utilizing 40 eV photons is shown in panels (d,g,j,m) and (e,h,k,n). Panels (f,i,l,o) correspond to CD-ARPES signals along the $K'-K', K-K$ and $K'-M-K$ cuts, respectively. Vertical and horizontal cuts are indicated by dotted green and blue lines, respectively.

the dichroic signals are asymmetrical around the binding energy 3 eV, the bands which are red on the left-hand side are not of blue color on the right-hand side indicated by black colored dashed circular line. This asymmetric dichroic signal is attributed to the orbital angular momentum originating from the combination of two twisted WSe₂ bilayers. Furthermore, in all the E(k) dispersion maps, the electronic bands are not well-defined at high symmetry K and K' points from both the monolayer layers of the BL WSe₂ sample. Still, there are signatures of graphite and WSe₂ bands in the energy-momentum maps, as shown in fig. 6.8(d,e,g,h). Nevertheless, we observe blue and red color intensities at K points, suggesting that the K valley integrated circular dichroism is still present in the

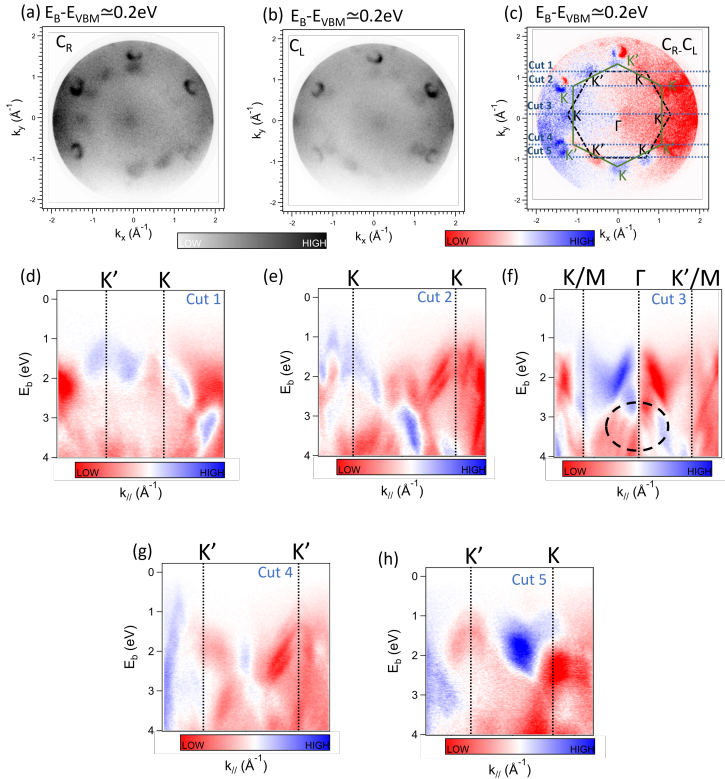


Figure 6.8: BL WSe₂/graphite/n-Si: Panel (a,b) show momentum maps taken by RCP and LCP incident light at $E_B - E_{VBM} = 0.3$ eV. Panel (c) depicts the CD-ARPES signals, with green and black hexagons denoting the BZ from both WSe₂ monolayers, and blue dotted lines along high symmetry points of WSe₂. Panel (d-i) show the E(k) maps.

WSe₂ bilayer sample system.

In principle, one may expect signatures of hybridization with some new features in CD-ARPES data, but disentangling such an effect would require further calculations, which should include hybridized layers. The presented theoretical DFT calculations do not account for hybridization, and any realistic calculations of CD-ARPES from twisted layers will be computationally demanding because it would require large unit cells. Furthermore, the OAM is mostly oriented out-of-plane in WSe₂, but an in-plane component may appear in twisted bilayers [284–287]. In twisted bilayer TMDCs, the orientation of OAM can be influenced by a range of factors, including the twist angle, the number of layers, as well as the applied magnetic and electric fields [288, 289].

6.2.3 Conclusions

This chapter reported circular dichroism investigation in the angular distribution of photoelectrons on a WSe₂ transition metal dichalcogenide. We measured twisted SL WSe₂/graphite and twisted BL WSe₂/graphite with different twist angles, as well as bulk WSe₂. The experimental results were compared to theoretical DFT calculations. We observed a significant circular dichroism at *K* valleys of WSe₂, which is primarily due to the pronounced layer-resolved valley orbital polarization in bulk WSe₂ crystal despite being centrosymmetric, and we observed similar behavior in twisted SL WSe₂/graphite. Furthermore, the *K* valley circular dichroism is still observable in the twisted bilayer system, and also at the Γ point, but there is an asymmetry in the dichroic signal around 3 eV binding energy.

These findings are significant not just for this fascinating and technologically relevant material, but also for potential relation to the existence of recently introduced hidden local Berry curvature [271, 279, 280].

Chapter 7

Summary and Outlook

A focused approach in exploiting vdW structures for advanced electronics can reshape the future of currently available semiconductor materials. The advancement in tailoring material properties associated with band structure alignment has extended interest into probing layered vdW semiconductor materials [27–29, 101, 194–196]. Such an approach can bring out specialized properties in materials such as periodic moiré patterns, where the periodicity on semiconductor interfaces or hetero-junctions arises either from the different lattice constant or the twist angles. In particular, the twist angle between such layers provides an adjustable degree of freedom compared to conventional materials. The strength of the moiré potential is typically in the range of several meV, and lattice electrons interacting with this additional potential exhibit novel properties [30, 197]. In recent years, several exciting experimental breakthroughs have been documented, and the resulting hetero/homo-structures offer unique features and applications beyond their 2D parent crystals [42, 198–207]. These attributes offer the opportunity to construct atomically thin electronics based entirely on 2D materials [208–210]. Among the transition metal dichalcogenides, we have selected WSe₂ as a material of interest for this thesis.

In this thesis, the micro-angle resolved photoemission spectroscopy (μ -ARPES) experiments were utilized to study the mechanically restacked vdW hetero/homo-structures, such as twisted SL and BL WSe₂ on graphite flake. We investigated microstructures containing regions of SL and BL at different twist angles between WSe₂ and graphite and within the BL WSe₂. The WSe₂-related band manifold exhibits shifts in the binding energy of the order of 30 meV when probing different spots separated by only 2-4 μm on the same microflake. This is observed both for twisted SL and twisted BL WSe₂ flakes, and indicates inhomogeneities and local doping varying laterally on the μm scale. In all cases, the global valence band maximum of WSe₂ has been found at the K_{WSe_2} point of

the Brillouin zone. Within this thesis, we investigated two twisted BL WSe₂ at twist angles of $\sim 28^\circ$ and $\sim 10^\circ$ showing bonding and antibonding interlayer hybridization at local VBM at Γ , and found no evidence of hybridization gaps at the interlayer band crossing points, that could be precursors of the flat bands at smaller twist angles. Hybridization gaps are also not observed in the studied twisted SL WSe₂/graphite structures. In twisted SL WSe₂/graphite, Fermi level electrons emitted from the graphite are sharply focused near their K_{gr} points in BZ, and when passing through the WSe₂ get diffracted to form band replicas readily observed on Fermi surface maps whose positions can be predicted by combining the reciprocal lattice vectors of graphite and WSe₂. Utilizing this, we determine the twist angle between the SL WSe₂/graphite. The combination of experimental findings and DFT calculations allows the identification of interlayer hybridization at Γ point and VBM at K_{WSe_2} point. The theoretical DFT modeling, with the inclusion of vdW forces, suggests that forming of hybridization in WSe₂/graphene system sensitively depends on the orbital character of the WSe₂ at the crossing with the graphene Dirac cone band.

We also experimentally showed photon energy-dependent intensity modulations of the hybridized bands of twisted WSe₂ bilayers. The relative ARPES intensities of these bands are different at different photon energies. In the twisted BL spectra taken at different photon energies between 80 and 150 eV, the bonding and antibonding splitting at Γ_0 also exhibit similar photon energy-dependent differences. We propose that these effects are related to the combination of intrinsic and extrinsic effects. The former is due to the photoemission matrix element effects that can be selectively sensitive to the regions of different local doping at different emission angles and photon energies. The latter could be due to the ARPES data collection technique that has been used, with possible 1-2 μm photon beam position shifts at different electron emission angles.

Additionally, we examined circular dichroism in the angular distribution of photoelectrons on a 2H-WSe₂. Within this work, SL WSe₂/graphite and twisted BL WSe₂/graphite structures with different twist angles, as well as bulk WSe₂, were measured. We reported significant CD signals at K valley in both bulk WSe₂ and SL WSe₂/graphite, while in twisted BL WSe₂, K valley integrated CD-ARPES is still visible in addition to the dichroic signal asymmetry shown at Γ . The CD-ARPES results were modeled theoretically by one-step model photoemission calculations, and they show qualitative agreement to the experimental

data, however, further calculations with the interlayer hybridization included would be needed to obtain a quantitative agreement.

The reported findings presented here indicate compelling evidence of the fundamental importance of WSe_2 , suggesting its use in the fabrication of a variety of electronic devices, from transistors to optical sensors. As such, small twist angle between WSe_2 monolayers alters its electronic band structure, thus influencing overall optical and electric transport behavior. Moreover, the results presented here also provide a possible relation to the recently introduced hidden local Berry curvature [271, 279, 280].

Overall, the results are encouraging, which can be further stretched to study the modulation in hetero/homo-structures properties at smaller twist angles between atomically thin layers, which would enable imaging their fascinating predicted properties such as topologically non-trivial flat bands [290]. Other similar TMDCs structures such as WS_2 and MoS_2 of various thicknesses and different mechanically restacked hetero-structures such as $\text{WSe}_2/\text{MoSe}_2$, WSe_2/WS_2 can also be included. Subsequently, the next phase of the research shall include the study of spin-texture in twisted SL and BL structures of TMDCs which can open up new possibilities for spintronics, valleytronics, and other related disciplines.

List of Abbreviations

AES	Auger electron spectroscopy
AFM	Atomic force microscopy
ALS	Advanced light source
ANTARES	Analysis nano-spot angle resolved photoemission spectroscopy
ARPES	Angle-resolved photoemission spectroscopy
BL	Bilayer
BP	Black phosphorous
BZ	Brillouin zone
CBM	Conduction band minimum
CD-ARPES	Circular dichroism in angle-resolved photoemission spectroscopy
CD	Circular dichroism
CEM	Constant energy map
CVD	Chemical vapor deposition
DFT	Density functional theorem
EDC	Energy dispersion curves
FEFS	Free-electron final-state
FZP	Fresnel zone plate
GGA	Generalized gradient approximation
HAXPES	Hard X-ray photoelectron spectroscopy
HS	Heterostructure
HOPG	Highly-oriented pyrolytic graphite
IMFP	Inelastic mean free path
KKR	Korringa-Kohn-Rostoker
LAPW	Linearized augmented plane wave
LCP	Left-handed circularly polarization
LDA	Local density approximation
LED	Light-emitting diodes
LEED	Low-energy electron diffraction
LEEM	Low-energy electron microscopy
MAESTRO	Microscopic and electronic structure observatory

MBE	Molecular beam epitaxy
MCP	Multi channel plate
OAM	Orbital angular momentum
OSA	Order sorting aperture
PDMS	Polydimethylsiloxane
PEEM	Photoemission electron microscopy
PES	Photoemission electron spectroscopy
PGI	Peter Grünberg Institut
PGM	Plane-grating monochromator
PL	Photoluminescence
PLD	Pulse laser deposition
PMMA	Poly-methylmethacrylate
PPC	Polypropylene carbonate
RCP	Right-handed circularly polarization
RMS	Root mean square
ROI	Region of interest
SBZ	Surface Brillouin zone
SL	Single layer
SOC	Spin-orbit coupling
TMDC	Transition metal dichalcogenides
TRIM	Time-reversal invariant momenta
UHV	Ultra-high vacuum
UPS	Ultraviolet photoemission spectroscopy
UV	Ultraviolet
VASP	Vienna Ab initio Simulation Package
VBM	Valence band maximum
vdW	van der Waals
VUV	Vacuum ultraviolet
XC	Exchange-correlation
XMCD	X-ray magnetic circular dichroism
XPS	X-ray photoemission spectroscopy
2D	Two-dimensional
3D	Three-dimensional
4D	Four-dimensional

Bibliography

- [1] C. Weiner, “How the transistor emerged,” *IEEE Spectr.*, vol. 10, no. 1, pp. 24–33, 2009. (Cited in page 1).
- [2] W. Shockley, M. Sparks, and G. K. Teal, “p-n junction transistors,” *Phys. Rev.*, vol. 83, no. 1, pp. 151–162, 1951. (Cited in page 1).
- [3] W. S. Gorton, “The genesis of the transistor,” *Proc. IEEE*, vol. 86, no. 1, pp. 50–52, 1998. (Cited in page 1).
- [4] J. Bardeen and W. H. Brattain, “The transistor, a semi-conductor triode,” *Physical Review*, vol. 74, no. 2, p. 230, 1948. (Cited in page 1).
- [5] G. E. Moore, “Cramming more components onto integrated circuits,” *Proc. IEEE*, vol. 86, no. 1, pp. 82–85, 1998. (Cited in page 1).
- [6] T. S. of the Intel 4004, <https://www.intel.com/content/www/us/en/history/museum-story-of-intel-4004>, accessed: 2023-16-02. [Online]. Available: <https://www.intel.com/content/www/us/en/history/museum-story-of-intel-4004> (Cited in page 1).
- [7] M. Waldrop, “More than Moore,” *New Sci.*, vol. 164, no. 2206, p. 58, 1999. (Cited in page 1).
- [8] A. Geim and K. S. Novoselov, “The rise of graphene,” *Nat. Mater.*, vol. 6, no. 3, pp. 183–191, 2007. (Cited in pages 1, 25, 37).
- [9] F. Schwierz, “Graphene transistors,” *Nat. Nanotechnol.*, vol. 5, no. 7, pp. 487–496, 2010. (Cited in pages 1, 25).
- [10] N. O. Weiss, H. Zhou, L. Liao, Y. Liu, S. Jiang, Y. Huang, and X. Duan, “Graphene: An emerging electronic material,” *Adv. Mater.*, vol. 24, no. 43, pp. 5782–5825, 2012. (Cited in pages 1, 25).
- [11] X. Tian, J. Xu, and X. Wang, “Band gap opening of bilayer graphene by F4-TCNQ molecular doping and externally applied electric field,” *J. Phys. Chem. B*, vol. 114, no. 35, pp. 11 377–11 381, 2010. (Cited in pages 1, 25).
- [12] S. Y. Lee, D. L. Duong, Q. A. Vu, Y. Jin, P. Kim, and Y. H. Lee, “Chemically modulated band gap in bilayer graphene memory transistors with high on/off ratio,” *ACS Nano*, vol. 9, no. 9, pp. 9034–9042, 2015. (Cited in pages 1, 25).

-
- [13] J. Bai, X. Zhong, S. Jiang, Y. Huang, and X. Duan, "Graphene nanomesh," *Nat. Nanotechnol.*, vol. 5, no. 3, pp. 190–194, 2010. (Cited in pages 1, 25).
- [14] J. T. Robinson, J. S. Burgess, C. E. Junkermeier, S. C. Badescu, T. L. Reinecke, F. K. Perkins, M. K. Zalalutdniov, J. W. Baldwin, J. C. Culbertson, P. E. Sheehan, and E. S. Snow, "Properties of fluorinated graphene films," *Nano Lett.*, vol. 10, no. 8, pp. 3001–3005, 2010. (Cited in pages 1, 25).
- [15] Y. Zhang, T. T. Tang, C. Girit, Z. Hao, M. C. Martin, A. Zettl, M. F. Crommie, Y. R. Shen, and F. Wang, "Direct observation of a widely tunable bandgap in bilayer graphene," *Nature*, vol. 459, no. 7248, pp. 820–823, 2009. (Cited in pages 1, 25).
- [16] J. B. Oostinga, H. B. Heersche, X. Liu, A. F. Morpurgo, and L. M. Vandersypen, "Gate-induced insulating state in bilayer graphene devices," *Nat. Mater.*, vol. 7, no. 2, pp. 151–157, 2008. (Cited in pages 1, 25, 47).
- [17] M. Y. Han, B. Özyilmaz, Y. Zhang, and P. Kim, "Energy band-gap engineering of graphene nanoribbons," *Phys. Rev. Lett.*, vol. 98, no. 20, pp. 1–4, 2007. (Cited in pages 1, 25).
- [18] D. L. Duong, S. M. Lee, S. H. Chae, Q. H. Ta, S. Y. Lee, G. H. Han, J. J. Bae, and Y. H. Lee, "Band-gap engineering in chemically conjugated bilayer graphene: Ab initio calculations," *Phys. Rev. B - Condens. Matter Mater. Phys.*, vol. 85, no. 20, pp. 2–6, 2012. (Cited in pages 1, 25).
- [19] W. Zhang, C. T. Lin, K. K. Liu, T. Tite, C. Y. Su, C. H. Chang, Y. H. Lee, C. W. Chu, K. H. Wei, J. L. Kuo, and L. J. Li, "Opening an electrical band gap of bilayer graphene with molecular doping," *ACS Nano*, vol. 5, no. 9, pp. 7517–7524, 2011. (Cited in pages 1, 25).
- [20] D. Jariwala, V. K. Sangwan, L. J. Lauhon, T. J. Marks, and M. C. Hersam, "Emerging device applications for two-dimensional semiconductors," *ACS Nano*, vol. 8, no. 2, pp. 1102–1120, 2014. (Cited in pages 2, 25, 26).
- [21] W. T. Hsu, L. S. Lu, D. Wang, J. K. Huang, M. Y. Li, T. R. Chang, Y. C. Chou, Z. Y. Juang, H. T. Jeng, L. J. Li, and W. H. Chang, "Evidence of indirect gap in monolayer WSe₂," *Nat. Commun.*, vol. 8, no. 1, pp. 1–7, 2017. (Cited in pages 2, 25).
- [22] M. A. Cazalilla, H. Ochoa, and F. Guinea, "Quantum spin hall effect in two-dimensional crystals of transition-metal dichalcogenides," *Phys. Rev. Lett.*, vol. 113, no. 7, 2014. (Cited in pages 2, 25, 26).

- [23] S. G. Benka, “Two-dimensional atomic crystals,” *Phys. Today*, vol. 58, no. 9, pp. 9–9, 2005. (Cited in pages 2, 25).
- [24] A. K. Geim, “Atomic-scale Legos,” *Sci. Am.*, vol. 311, no. 6, pp. 50–51, 2014. (Cited in page 2).
- [25] A. K. Geim and I. V. Grigorieva, “Van der Waals heterostructures.” *Nature*, vol. 499, no. 7459, pp. 419–25, 2013. (Cited in pages 2, 25, 61).
- [26] H. Yuan, Z. Liu, G. Xu, B. Zhou, S. Wu, D. Dumcenco, K. Yan, Y. Zhang, S. K. Mo, P. Dudin, V. Kandyba, M. Yablonskikh, A. Barinov, Z. Shen, S. Zhang, Y. Huang, X. Xu, Z. Hussain, H. Y. Hwang, Y. Cui, and Y. Chen, “Evolution of the valley position in bulk transition-metal chalcogenides and their monolayer limit,” *Nano Lett.*, vol. 16, no. 8, pp. 4738–4745, 2016. (Cited in page 2).
- [27] M. H. Chiu, M. Y. Li, W. Zhang, W. T. Hsu, W. H. Chang, M. Terrones, H. Terrones, and L. J. Li, “Spectroscopic signatures for interlayer coupling in MoS₂-WSe₂ van der waals stacking,” *ACS Nano*, vol. 8, no. 9, pp. 9649–9656, 2014. (Cited in pages 2, 26, 61, 113).
- [28] G. Fiori, F. Bonaccorso, G. Iannaccone, T. Palacios, D. Neumaier, A. Seabaugh, S. K. Banerjee, and L. Colombo, “Electronics based on two-dimensional materials,” *Nat. Nanotechnol.*, vol. 9, no. 10, pp. 768–779, 2014. (Cited in pages 2, 61, 113).
- [29] L. Wang, E. M. Shih, A. Ghiotto, L. Xian, D. A. Rhodes, C. Tan, M. Claassen, D. M. Kennes, Y. Bai, B. Kim, K. Watanabe, T. Taniguchi, X. Zhu, J. Hone, A. Rubio, A. N. Pasupathy, and C. R. Dean, “Correlated electronic phases in twisted bilayer transition metal dichalcogenides,” *Nat. Mater.*, vol. 19, no. 8, pp. 861–866, 2020. (Cited in pages 2, 61, 113).
- [30] F. He, Y. Zhou, Z. Ye, S. H. Cho, J. Jeong, X. Meng, and Y. Wang, “Moiré Patterns in 2D Materials: A Review,” *ACS Nano*, vol. 15, no. 4, pp. 5944–5958, 2021. (Cited in pages 2, 61, 113).
- [31] Y. Cao, V. Fatemi, S. Fang, K. Watanabe, T. Taniguchi, E. Kaxiras, and P. Jarillo-Herrero, “Unconventional superconductivity in magic-angle graphene superlattices,” *Nature*, vol. 556, no. 7699, pp. 43–50, 2018. (Cited in pages 2, 47).
- [32] S. A. Wolf, D. D. Awschalom, R. A. Buhrman, J. M. Daughton, v. S. von Molnár, M. L. Roukes, A. Y. Chtchelkanova, and D. M. Treger, “Spintron-

- ics: a spin-based electronics vision for the future,” *Science*, vol. 294, no. 5546, pp. 1488–1495, 2001. (Cited in page 2).
- [33] K. Sato and H. Katayama-Yoshida, “First principles materials design for semiconductor spintronics,” *Semicond. Sci. Technol.*, vol. 17, no. 4, pp. 367–376, 2002. (Cited in page 2).
- [34] D. D. Awschalom and M. E. Flatté, “Challenges for semiconductor spintronics,” *Nat. Phys.*, vol. 3, no. 3, pp. 153–159, 2007. (Cited in page 2).
- [35] M. V. Kamalakar, A. Dankert, J. Bergsten, T. Ive, and S. P. Dash, “Spintronics with graphene-hexagonal boron nitride van der Waals heterostructures,” *Appl. Phys. Lett.*, vol. 105, no. 21, pp. 2–6, 2014. (Cited in page 2).
- [36] J. L. Garcia-Pomar, A. Cortijo, and M. Nieto-Vesperinas, “Fully valley-polarized electron beams in graphene,” *Phys. Rev. Lett.*, vol. 100, no. 23, pp. 1–4, 2008. (Cited in page 2).
- [37] D. Gunlycke and C. T. White, “Graphene valley filter using a line defect,” *Phys. Rev. Lett.*, vol. 106, no. 13, pp. 1–4, 2011. (Cited in page 2).
- [38] R. Suzuki, M. Sakano, Y. J. Zhang, R. Akashi, D. Morikawa, A. Harasawa, K. Yaji, K. Kuroda, K. Miyamoto, T. Okuda, K. Ishizaka, R. Arita, and Y. Iwasa, “Valley-dependent spin polarization in bulk MoS₂ with broken inversion symmetry,” *Nat. Nanotechnol.*, vol. 9, no. 8, pp. 611–617, 2014. (Cited in page 2).
- [39] A. Pulkin and O. V. Yazyev, “Spin-and valley-polarized transport across line defects in monolayer MoS₂,” *Physical Review B*, vol. 93, no. 4, p. 041419, 2016. (Cited in pages 2, 33).
- [40] S. D. Conte, F. Bottegoni, E. A. A. Pogna, S. Ambrogio, I. Bargigia, C. D’Andrea, D. De Fazio, A. Lombardo, M. Bruna, F. Ciccacci *et al.*, “Valley and spin dynamics in monolayer MoS₂,” *arXiv:1502.06817*, 2015. (Cited in page 2).
- [41] A. Pospischil, M. M. Furchi, and T. Mueller, “Solar-energy conversion and light emission in an atomic monolayer p-n diode,” *Nat. Nanotechnol.*, vol. 9, no. 4, pp. 257–261, 2014. (Cited in pages 2, 26).
- [42] F. Withers, O. Del Pozo-Zamudio, A. Mishchenko, A. P. Rooney, A. Gholinia, K. Watanabe, T. Taniguchi, S. J. Haigh, A. K. Geim,

- A. I. Tartakovskii, and K. S. Novoselov, “Light-emitting diodes by band-structure engineering in van der Waals heterostructures,” *Nat. Mater.*, vol. 14, no. 3, pp. 301–306, 2015. (Cited in pages 2, 62, 113).
- [43] H. Tian, M. L. Chin, S. Najmaei, Q. Guo, F. Xia, H. Wang, and M. Dubey, “Optoelectronic devices based on two-dimensional transition metal dichalcogenides,” *Nano Res.*, vol. 9, no. 6, pp. 1543–1560, 2016. (Cited in pages 2, 35).
- [44] N. Perea-López, A. L. Elías, A. Berkdemir, A. Castro-Beltran, H. R. Gutiérrez, S. Feng, R. Lv, T. Hayashi, F. López-Urías, S. Ghosh, B. Muchharla, S. Talapatra, H. Terrones, and M. Terrones, “Photosensor device based on few-layered WS₂ films,” *Adv. Funct. Mater.*, vol. 23, no. 44, pp. 5511–5517, 2013. (Cited in pages 2, 35).
- [45] S. Agnoli, A. Ambrosetti, T. O. Menteş, A. Sala, A. Locatelli, P. L. Silvestrelli, M. Cattelan, S. Eichfeld, D. D. Deng, J. A. Robinson, J. Avila, C. Chen, and M. C. Asensio, “Unraveling the structural and electronic properties at the WSe₂-graphene interface for a rational design of van der Waals heterostructures,” *ACS Appl. Nano Mater.*, vol. 1, no. 3, pp. 1131–1140, 2018. (Cited in pages 3, 71, 86).
- [46] N. R. Wilson, P. V. Nguyen, K. Seyler, P. Rivera, A. J. Marsden, Z. P. Laker, G. C. Constantinescu, V. Kandyba, A. Barinov, N. D. Hine, X. Xu, and D. H. Cobden, “Determination of band offsets, hybridization, and exciton binding in 2D semiconductor heterostructures,” *Sci. Adv.*, vol. 3, no. 2, pp. 1–8, 2017. (Cited in pages 3, 71, 86).
- [47] F. Bloch, “Über die Quantenmechanik der Elektronen in Kristallgittern,” *Zeitschrift für Phys.*, vol. 52, no. 7-8, pp. 555–600, 1929. (Cited in page 5).
- [48] C. Kittel, *Introduction to Solid State Physics*. Chapter 2, John Wiley & Sons, Inc., New York, 6th edition, 1986. (Cited in pages 5, 6).
- [49] S. Hüfner, *Photoelectron Spectroscopy*. Chapter 6, Springer-Verlag Berlin and Heidelberg GmbH Co. KG, 1995. (Cited in pages 8, 9, 13).
- [50] E. W. Plummer and W. Eberhardt, *Angle-Resolved Photoemission as a Tool for the Study of Surfaces*. John Wiley Sons, Ltd, 1982. (Cited in page 8).

-
- [51] S. Hüfner, *Very High Resolution Photoelectron Spectroscopy*. Springer-Verlag Berlin Heidelberg, 2007. (Cited in page 8).
- [52] A. S. Shigemasa Suga, *Bulk and Surface Electronic Structures*. Springer Berlin, Heidelberg, 2014. (Cited in page 8).
- [53] A. Damascelli, “Probing the Electronic Structure of Complex Systems by ARPES,” *Phys. Scr.*, vol. T109, pp. 61–74, 2004. (Cited in pages 8, 9).
- [54] C. M. Schneider, *Photoelectron Emission Spectroscopy*. Chapter F3, Forschungszentrum Jülich GmbH, 43rd IFF Spring School, 2012. (Cited in pages 8, 11).
- [55] L. Plucinski, *Photoelectron Spectroscopy*. Chapter C5, Forschungszentrum Jülich GmbH, 47th IFF Spring School, 2016. (Cited in page 8).
- [56] S. Moser, “An experimentalist’s guide to the matrix element in angle resolved photoemission,” *J. Electron Spectros. Relat. Phenomena*, vol. 214, pp. 29–52, 2017. (Cited in pages 8, 72, 104).
- [57] H. Hertz, “Ueber einen einfluss des ultravioletten liches auf die electriche entladung,” *Annalen der Physik*, vol. 267, no. 8, pp. 983–1000, 1887. (Cited in page 8).
- [58] H. P. Bonzel and C. Kleint, “On the history of photoemission,” *Progress in surface science*, vol. 49, no. 2, pp. 107–153, 1995. (Cited in page 8).
- [59] A. Einstein, “Über einen die erzeugung und verwandlung des liches betreffenden heuristischen gesichtspunkt,” *Annalen der Physik*, vol. 322, no. 6, pp. 132–148, 1905. (Cited in page 8).
- [60] A. X. Gray, C. Papp, S. Ueda, B. Balke, Y. Yamashita, L. Plucinski, J. Minár, J. Braun, E. R. Ylvisaker, C. M. Schneider, W. E. Pickett, H. Ebert, K. Kobayashi, and C. S. Fadley, “Probing bulk electronic structure with hard X-ray angle-resolved photoemission,” *Nat. Mater.*, vol. 10, no. 10, pp. 759–764, 2011. (Cited in page 9).
- [61] E. Kokkonen, M. Kaipio, H.-E. Nieminen, F. Rehman, V. Miikkulainen, M. Putkonen, M. Ritala, S. Huotari, J. Schnadt, and S. Urpelainen, “Ambient pressure x-ray photoelectron spectroscopy setup for synchrotron-based in situ and operando atomic layer deposition research,” *Review of Scientific Instruments*, vol. 93, no. 1, p. 013905, 2022. (Cited in page 9).
- [62] S. Ueda, “Application of hard X-ray photoelectron spectroscopy to electronic structure measurements for various functional materials,” *Journal*

- of Electron Spectroscopy and Related Phenomena*, vol. 190, pp. 235–241, 2013. (Cited in page 9).
- [63] S. Mathias, M. Wiesenmayer, F. Deicke, A. Ruffing, L. Miaja-Avila, M. Murnane, H. Kapteyn, M. Bauer, and M. Aeschlimann, “Time and angle resolved photoemission spectroscopy using femtosecond visible and high-harmonic light,” in *Journal of Physics: Conference Series*, vol. 148, no. 1. IOP Publishing, 2009, p. 012042. (Cited in page 9).
- [64] J. Osterwalder, “Spin-polarized photoemission,” *Magnetism: A Synchrotron Radiation Approach*, pp. 95–120, 2006. (Cited in page 9).
- [65] A. D. Palczewski, “Angle-resolved photoemission spectroscopy (ARPES) studies of cuprate superconductors,” *J. Chem. Inf. Model.*, vol. 53, no. 9, pp. 1689–1699, 2019. (Cited in page 9).
- [66] P. J. Feibelman and D. E. Eastman, “Photoemission spectroscopy—correspondence between quantum theory and experimental phenomenology,” *Phys. Rev. B*, vol. 10, pp. 4932–4947, Dec 1974. (Cited in page 10).
- [67] N. Smith, “Photoemission linewidths and quasiparticle lifetimes,” *Phys. Rev. B*, vol. 47, no. 23, 1993. (Cited in page 11).
- [68] M. M. Traum, “Angular dependence of photoemission and atomic orbitals in the layer compound 1T-TaSe₂,” *Phys. Rev. Lett.*, vol. 32, no. 22, pp. 1–4, 1974. (Cited in page 11).
- [69] A. Damascelli, Z. Hussain, and Z. X. Shen, “Angle-resolved photoemission studies of the cuprate superconductors,” *Rev. Mod. Phys.*, vol. 75, no. 2, pp. 473–541, 2003. (Cited in pages 11, 13, 98).
- [70] R. H. Williams and A. J. McEvoy, “Photoemission studies of MoS₂,” *Phys. Status Solidi*, vol. 47, no. 1, pp. 217–224, 1971. (Cited in page 11).
- [71] Wikipedia: "ARPES", https://en.wikipedia.org/wiki/Angle-resolved_photoemission_spectroscopy, accessed:2021-11-21. [Online]. Available: https://en.wikipedia.org/wiki/Angle-resolved_photoemission_spectroscopy (Cited in page 13).
- [72] G. D. Mahan, “Theory of photoemission in simple metals,” *Phys. Rev. B*, vol. 2, pp. 4334–4350, Dec 1970. (Cited in page 14).
- [73] M. P. Seah and W. A. Dench, “Quantitative electron spectroscopy of surfaces,” *Surf. Interface Anal.*, vol. 1, no. 1, pp. 2–11, 1979. (Cited in page 15).

-
- [74] F. Schwabl, *Quantenmechanik (QM I): Springer-Lehrbuch*. Springer, 2002. (Cited in page 18).
- [75] A. Manchon and A. Belabbes, *Spin-orbitronics at transition metal interfaces*. Chapter C1, Solid State Physics, Elsevier, 2017. (Cited in page 18).
- [76] J. C. Slater, “Wave functions in a periodic potential,” *Phys. Rev.*, vol. 51, no. 10, pp. 846–851, 1937. (Cited in page 21).
- [77] P. Hohenberg, “Inhomogenous electron gas,” *Phys. Rev.*, vol. 136, 1964. (Cited in pages 21, 62).
- [78] W. Kohn and L. J. Sham, “Self-consistent equations including exchange and correlation effects,” *Phys. Rev.*, vol. 140, 1965. (Cited in pages 21, 62).
- [79] G. Bihlmayer, *Electronic structure of matter: Basics and DFT. in: Probing the Nanoworld*. Chapter A3, Forschungszentrum Jülich GmbH, 38th IFF Spring School, 2007. (Cited in page 22).
- [80] J. P. Perdew and Y. Wang, “Pair-distribution function and its coupling-constant average for the spin-polarized electron gas,” *Phys. Rev. B*, vol. 46, pp. 12 947–12 954, Nov 1992. (Cited in page 22).
- [81] D. M. Ceperley and B. J. Alder, “Ground state of the electron gas by a stochastic method,” *Phys. Rev. Lett.*, vol. 45, no. 7, pp. 566–569, 1980. (Cited in page 22).
- [82] A. Dal Corso, A. Pasquarello, A. Baldereschi, and R. Car, “Generalized-gradient approximations to density-functional theory: A comparative study for atoms and solids,” *Phys. Rev. B - Condens. Matter Mater. Phys.*, vol. 53, no. 3, pp. 1180–1185, 1996. (Cited in page 22).
- [83] A. García, C. Elsässer, J. Zhu, S. G. Louie, and M. L. Cohen, “Use of gradient-corrected functionals in total-energy calculations for solids,” *Phys. Rev. B*, vol. 46, no. 15, pp. 9829–9832, 1992. (Cited in page 22).
- [84] G. Kresse and J. Furthmüller, “Efficient iterative schemes for ab initio total-energy calculations using a plane-wave basis set,” *Phys. Rev. B - Condens. Matter Mater. Phys.*, vol. 54, no. 16, pp. 11 169–11 186, 1996. (Cited in page 22).
- [85] G. Kresse and J. Hafner, “Ab initio molecular dynamics for liquid metals,” *Phys. Rev. B*, vol. 47, no. 1, pp. 558–561, 1993. (Cited in page 22).

- [86] P. E. Blöchl, “Projector augmented-wave method,” *Phys. Rev. B*, vol. 50, no. 24, pp. 17 953–17 979, 1994. (Cited in page 22).
- [87] F. project homepage, <https://www.flapw.de/>, accessed: 2022-03-11. [Online]. Available: <https://www.flapw.de/> (Cited in page 23).
- [88] P. Blaha, K. Schwarz, F. Tran, R. Laskowski, G. K. H. Madsen, and L. D. Marks, “WIEN2k: An APW+lo program for calculating the properties of solids,” *J. Chem. Phys.*, vol. 152, no. 7, feb 2020. (Cited in page 23).
- [89] O. Gunnarsson and B. I. Lundqvist, “Exchange and correlation in atoms, molecules, and solids by the spin-density-functional formalism,” *Phys. Rev. B*, vol. 13, pp. 4274–4298, May 1976. (Cited in page 23).
- [90] E. McCann, “Interlayer asymmetry gap in the electronic band structure of bilayer graphene,” *Phys. Status Solidi Basic Res.*, vol. 244, no. 11, pp. 4112–4117, 2007. (Cited in page 25).
- [91] D. C. Elias, R. R. Nair, T. M. G. Mohiuddin, S. V. Morozov, P. Blake, M. P. Halsall, A. C. Ferrari, D. W. Boukhvalov, M. I. Katsnelson, A. K. Geim, and K. S. Novoselov, “Control of graphene’s properties by reversible hydrogenation: Evidence for graphane,” *Science*, vol. 323, no. 5914, pp. 610–613, 2009. (Cited in page 25).
- [92] J. Park, S. B. Jo, Y. J. Yu, Y. Kim, J. W. Yang, W. H. Lee, H. H. Kim, B. H. Hong, P. Kim, K. Cho, and K. S. Kim, “Single-gate bandgap opening of bilayer graphene by dual molecular doping,” *Adv. Mater.*, vol. 24, no. 3, pp. 407–411, 2012. (Cited in page 25).
- [93] P. Joensen, R. F. Frindt, and S. R. Morrison, “Single-layer MoS₂,” *Mater. Res. Bull.*, vol. 21, no. 4, pp. 457–461, 1986. (Cited in page 25).
- [94] B. Radisavljevic, A. Radenovic, J. Brivio, V. Giacometti, and A. Kis, “Single-layer MoS₂ transistors,” *Nat. Nanotechnol.*, vol. 6, no. 3, pp. 147–150, 2011. (Cited in page 26).
- [95] Y.-M. Lin, K. A. Jenkins, A. Valdes-Garcia, J. P. Small, D. B. Farmer, and P. Avouris, “Operation of graphene transistors at gigahertz frequencies,” *Nano Letters*, vol. 9, no. 1, pp. 422–426, 2009. (Cited in page 26).
- [96] Y. Deng, Z. Luo, N. J. Conrad, H. Liu, Y. Gong, S. Najmaei, P. M. Ajayan, J. Lou, X. Xu, and P. D. Ye, “Black phosphorus-monolayer MoS₂ van der Waals heterojunction p-n diode,” *ACS Nano*, vol. 8, no. 8, pp. 8292–8299, 2014. (Cited in page 26).

- [97] J. A. Wilson and A. D. Yoffe, “The transition metal dichalcogenides discussion and interpretation of the observed optical, electrical and structural properties,” *Adv. Phys.*, vol. 18, no. 73, pp. 193–335, 1969. (Cited in pages 26, 33).
- [98] P. Chen, W. W. Pai, Y. H. Chan, W. L. Sun, C. Z. Xu, D. S. Lin, M. Y. Chou, A. V. Fedorov, and T. C. Chiang, “Large quantum-spin-Hall gap in single-layer 1T'-WSe₂,” *Nat. Commun.*, vol. 9, no. 1, pp. 1–7, 2018. (Cited in page 26).
- [99] X. Xi, Z. Wang, W. Zhao, J. H. Park, K. T. Law, H. Berger, L. Forró, J. Shan, and K. F. Mak, “Ising pairing in superconducting NbSe₂ atomic layers,” *Nat. Phys.*, vol. 12, no. 2, pp. 139–143, 2016. (Cited in page 26).
- [100] Y. T. Hsu, A. Vaezi, M. H. Fischer, and E. A. Kim, “Topological superconductivity in monolayer transition metal dichalcogenides,” *Nat. Commun.*, vol. 8, 2017. (Cited in page 26).
- [101] S. Manzeli, D. Ovchinnikov, D. Pasquier, O. V. Yazyev, and A. Kis, “2D transition metal dichalcogenides,” *Nat. Rev. Mater.*, vol. 2, 2017. (Cited in pages 27, 61, 113).
- [102] Z. Wang, D. Gresch, A. A. Soluyanov, W. Xie, S. Kushwaha, X. Dai, M. Troyer, R. J. Cava, and B. A. Bernevig, “MoTe₂: A Type-II Weyl Topological Metal,” *Phys. Rev. Lett.*, vol. 117, no. 5, pp. 1–5, 2016. (Cited in page 27).
- [103] A. A. Soluyanov, D. Gresch, Z. Wang, Q. Wu, M. Troyer, X. Dai, and B. A. Bernevig, “Type-II Weyl semimetals,” *Nature*, vol. 527, no. 7579, pp. 495–498, 2015. (Cited in page 27).
- [104] K. S. Novoselov, A. K. Geim, S. V. Morozov, D. Jiang, M. I. Katsnelson, I. V. Grigorieva, S. V. Dubonos, and A. A. Firsov, “Two-dimensional gas of massless Dirac fermions in graphene,” *Nature*, vol. 438, no. 7065, pp. 197–200, 2005. (Cited in page 28).
- [105] Z. Y. Zhu, Y. C. Cheng, and U. Schwingenschlögl, “Giant spin-orbit-induced spin splitting in two-dimensional transition-metal dichalcogenide semiconductors,” *Phys. Rev. B - Condens. Matter Mater. Phys.*, vol. 84, no. 15, pp. 1–5, 2011. (Cited in pages 29, 34, 99, 103).
- [106] M. Gehlmann, “The electronic structure of transition metal dichalcogenides investigated by angle-resolved photoemission spectroscopy,” dissertation, Universität Duisburg-Essen, 2017. (Cited in page 30).

- [107] F. Hanke and J. Björk, “Structure and local reactivity of the Au(111) surface reconstruction,” *Phys. Rev. B - Condens. Matter Mater. Phys.*, vol. 87, no. 23, pp. 1–6, 2013. (Cited in page 29).
- [108] X. Chen and A. R. McDonald, “Functionalization of two-dimensional transition-Metal dichalcogenides,” *Adv. Mater.*, vol. 28, no. 27, pp. 5738–5746, 2016. (Cited in page 29).
- [109] D. Jariwala, T. J. Marks, and M. C. Hersam, “Mixed-dimensional van der Waals heterostructures,” *Nat. Mater.*, vol. 16, no. 2, pp. 170–181, 2017. (Cited in page 29).
- [110] D. Nutting, J. F. Felix, E. Tillotson, D. W. Shin, A. De Sanctis, H. Chang, N. Cole, S. Russo, A. Woodgate, I. Leontis, H. A. Fernández, M. F. Craciun, S. J. Haigh, and F. Withers, “Heterostructures formed through abraded van der Waals materials,” *Nat. Commun.*, vol. 11, no. 1, pp. 1–10, 2020. (Cited in page 29).
- [111] Y. Cao, V. Fatemi, S. Fang, K. Watanabe, T. Taniguchi, E. Kaxiras, and P. Jarillo-Herrero, “Unconventional superconductivity in magic-angle graphene superlattices,” *Nature*, vol. 556, no. 7699, pp. 43–50, 2018. (Cited in page 31).
- [112] Z. Zuo, Z. Xu, R. Zheng, A. Khanaki, J.-G. Zheng, and J. Liu, “In-situ epitaxial growth of graphene/h-bn van der waals heterostructures by molecular beam epitaxy,” *Scientific reports*, vol. 5, no. 1, p. 14760, 2015. (Cited in page 31).
- [113] D. K. Singh and G. Gupta, “van der waals epitaxy of transition metal dichalcogenides via molecular beam epitaxy: looking back and moving forward,” *Materials Advances*, vol. 3, no. 15, pp. 6142–6156, 2022. (Cited in page 31).
- [114] X. Ma, S. Fu, J. Ding, M. Liu, A. Bian, F. Hong, J. Sun, X. Zhang, X. Yu, and D. He, “Robust interlayer exciton in ws2/mose2 van der waals heterostructure under high pressure,” *Nano Letters*, vol. 21, no. 19, pp. 8035–8042, 2021. (Cited in page 32).
- [115] Y. Meng, T. Wang, C. Jin, Z. Li, S. Miao, Z. Lian, T. Taniguchi, K. Watanabe, F. Song, and S.-F. Shi, “Electrical switching between exciton dissociation to exciton funneling in mose2/ws2 heterostructure,” *Nature Communications*, vol. 11, no. 1, p. 2640, 2020. (Cited in page 32).

- [116] X. Lin, F. Wang, X. Shan, Y. Miao, X. Chen, M. Yan, L. Zhang, K. Liu, J. Luo, and K. Zhang, “High-performance photodetector and its optoelectronic mechanism of mos₂/ws₂ vertical heterostructure,” *Applied Surface Science*, vol. 546, p. 149074, 2021. (Cited in pages 32, 35).
- [117] J. Sitek, I. Pasternak, K. Czerniak-Łosiewicz, M. Świniarski, P. P. Michałowski, C. McAleese, X. Wang, B. R. Conran, K. Wilczyński, M. Macha *et al.*, “Three-step, transfer-free growth of mos₂/ws₂/graphene vertical van der waals heterostructure,” *2D Materials*, vol. 9, no. 2, p. 025030, 2022. (Cited in page 32).
- [118] E. C. Ahn, “2d materials for spintronic devices,” *npj 2D Materials and Applications*, vol. 4, no. 1, p. 17, 2020. (Cited in page 32).
- [119] S. K. Mallik, A. K. Jena, N. K. Sharma, S. Sahoo, M. C. Sahu, S. K. Gupta, R. Ahuja, and S. Sahoo, “Transition metal substituted mos₂/ws₂ van der waals heterostructure for realization of dilute magnetic semiconductors,” *Journal of Magnetism and Magnetic Materials*, vol. 560, p. 169567, 2022. (Cited in page 32).
- [120] C. H. Lee, G. H. Lee, A. M. Van Der Zande, W. Chen, Y. Li, M. Han, X. Cui, G. Arefe, C. Nuckolls, T. F. Heinz, J. Guo, J. Hone, and P. Kim, “Atomically thin p-n junctions with van der Waals heterointerfaces,” *Nat. Nanotechnol.*, vol. 9, no. 9, pp. 676–681, 2014. (Cited in page 32).
- [121] J. Yuan, T. Sun, Z. Hu, W. Yu, W. Ma, K. Zhang, B. Sun, S. P. Lau, Q. Bao, S. Lin, and S. Li, “Wafer-scale fabrication of two-dimensional PtS₂/PtSe₂ heterojunctions for efficient and broad band photodetection,” *ACS Appl. Mater. Interfaces*, vol. 10, no. 47, pp. 40 614–40 622, 2018. (Cited in page 32).
- [122] S. J. Liang, B. Cheng, X. Cui, and F. Miao, “Van der Waals heterostructures for high-performance device applications: challenges and opportunities,” *Adv. Mater.*, vol. 32, no. 27, pp. 1–27, 2020. (Cited in page 32).
- [123] T. Cheiwchanchamnangij and W. R. Lambrecht, “Quasiparticle band structure calculation of monolayer, bilayer, and bulk MoS₂,” *Physical Review B*, vol. 85, no. 20, p. 205302, 2012. (Cited in pages 32, 33).
- [124] A. Kuc, N. Zibouche, and T. Heine, “Influence of quantum confinement on the electronic structure of the transition metal sulfide TS₂,” *Phys. Rev. B - Condens. Matter Mater. Phys.*, vol. 83, no. 24, pp. 1–4, 2011. (Cited in page 32).

- [125] A. Kumara and P. K. Ahluwalia, “Electronic structure of transition metal dichalcogenides monolayers 1H-MX₂ (M = Mo, W; X = S, Se, Te) from ab-initio theory: New direct band gap semiconductors,” *Eur. Phys. J. B*, vol. 85, no. 6, pp. 18–22, 2012. (Cited in page 32).
- [126] E. S. Kadantsev and P. Hawrylak, “Electronic structure of a single MoS₂ monolayer,” *Solid State Commun.*, vol. 152, no. 10, pp. 909–913, 2012. (Cited in page 32).
- [127] W. S. Yun, S. Han, S. C. Hong, I. G. Kim, and J. Lee, “Thickness and strain effects on electronic structures of transition metal dichalcogenides: 2h-m x 2 semiconductors (m= mo, w; x= s, se, te),” *Physical Review B*, vol. 85, no. 3, p. 033305, 2012. (Cited in page 32).
- [128] A. Splendiani, L. Sun, Y. Zhang, T. Li, J. Kim, C. Y. Chim, G. Galli, and F. Wang, “Emerging photoluminescence in monolayer MoS₂,” *Nano Lett.*, vol. 10, no. 4, pp. 1271–1275, 2010. (Cited in pages 32, 33).
- [129] K. F. Mak, C. Lee, J. Hone, J. Shan, and T. F. Heinz, “Atomically thin MoS₂: A new direct-gap semiconductor,” *Phys. Rev. Lett.*, vol. 105, no. 13, pp. 2–5, 2010. (Cited in pages 32, 33, 35, 61).
- [130] K. F. Mak, K. He, J. Shan, and T. F. Heinz, “Control of valley polarization in monolayer mos₂ by optical helicity,” *Nature nanotechnology*, vol. 7, no. 8, pp. 494–498, 2012. (Cited in page 33).
- [131] S. Lebègue and O. Eriksson, “Electronic structure of two-dimensional crystals from ab initio theory,” *Phys. Rev. B - Condens. Matter Mater. Phys.*, vol. 79, no. 11, pp. 4–7, 2009. (Cited in page 33).
- [132] C. Mai, A. G. Barrette, Y. Yu, Y. G. Semenov, K. W. Kim, L. Cao, and K. Gundogdu, “Many-body effects in valleytronics: direct measurement of valley lifetimes in single-layer mos₂,” *Nano letters*, vol. 14 1, pp. 202–6, 2014. (Cited in page 34).
- [133] J. M. Riley, F. Mazzola, M. Dendzik, M. Michiardi, T. Takayama, L. Bawden, C. Granerød, M. Leandersson, T. Balasubramanian, M. Hoesch, T. K. Kim, H. Takagi, W. Meevasana, P. Hofmann, M. S. Bahramy, J. W. Wells, and P. D. King, “Direct observation of spin-polarized bulk bands in an inversion-symmetric semiconductor,” *Nat. Phys.*, vol. 10, no. 11, pp. 835–839, 2014. (Cited in pages 34, 86, 99).

- [134] N. Alidoust, G. Bian, S. Y. Xu, R. Sankar, M. Neupane, C. Liu, I. Belopolski, D. X. Qu, J. D. Denlinger, F. C. Chou, and M. Z. Hasan, “Observation of monolayer valence band spin-orbit effect and induced quantum well states in MOX₂,” *Nat. Commun.*, vol. 5, pp. 1–8, 2014. [Online]. Available: <http://dx.doi.org/10.1038/ncomms5673> (Cited in page 34).
- [135] M. Gehlmann, I. Aguilera, G. Bihlmayer, E. Młyńczak, M. Eschbach, S. Döring, P. Gospodarič, S. Cramm, B. Kardynał, L. Plucinski, S. Blügel, and M. C. Schneider, “Quasi 2D electronic states with high spin-polarization in centrosymmetric MoS₂ bulk crystals,” *Scientific reports*, vol. 6, pp. 1–6, 2016. (Cited in pages 34, 74).
- [136] D. W. Latzke, W. Zhang, A. Suslu, T.-R. Chang, H. Lin, H.-T. Jeng, S. Tongay, J. Wu, A. Bansil, and A. Lanzara, “Electronic structure, spin-orbit coupling, and interlayer interaction in bulk mos 2 and ws 2,” *Physical Review B*, vol. 91, no. 23, p. 235202, 2015. (Cited in page 34).
- [137] D. Akinwande, C. J. Brennan, J. S. Bunch, P. Egberts, J. R. Felts, H. Gao, R. Huang, J.-S. Kim, T. Li, Y. Li *et al.*, “A review on mechanics and mechanical properties of 2d materials—graphene and beyond,” *Extreme Mechanics Letters*, vol. 13, pp. 42–77, 2017. (Cited in page 35).
- [138] P. Hess, “Bonding, structure, and mechanical stability of 2d materials: the predictive power of the periodic table,” *Nanoscale Horizons*, vol. 6, no. 11, pp. 856–892, 2021. (Cited in page 35).
- [139] M. C. Lemme, S. Wagner, K. Lee, X. Fan, G. J. Verbiest, S. Wittmann, S. Lukas, R. J. Dolleman, F. Niklaus, H. S. van der Zant *et al.*, “Nanoelectromechanical sensors based on suspended 2d materials,” *Research*, vol. 2020, 2020. (Cited in page 35).
- [140] D. J. Joe, E. Park, D. H. Kim, I. Doh, H.-C. Song, and J. Y. Kwak, “Graphene and two-dimensional materials-based flexible electronics for wearable biomedical sensors,” *Electronics*, vol. 12, no. 1, p. 45, 2022. (Cited in page 35).
- [141] G. Eda and S. A. Maier, “Two-dimensional crystals: Managing light for optoelectronics,” *ACS Nano*, vol. 7, no. 7, pp. 5660–5665, 2013. (Cited in page 35).

- [142] A. Grubišić Čabo, J. A. Miwa, S. S. Grønberg, J. M. Riley, J. C. Johannsen, C. Cacho, O. Alexander, R. T. Chapman, E. Springate, M. Gri-
oni, J. V. Lauritsen, P. D. King, P. Hofmann, and S. Ulstrup, “Observation
of ultrafast free carrier dynamics in single layer MoS₂,” *Nano Lett.*, vol. 15,
no. 9, pp. 5883–5887, 2015. (Cited in page 35).
- [143] R. S. Sundaram, M. Engel, A. Lombardo, R. Krupke, A. C. Ferrari,
P. Avouris, and M. Steiner, “Electroluminescence in single layer MoS₂,”
Nano Lett., vol. 13, no. 4, pp. 1416–1421, 2013. (Cited in page 35).
- [144] Z. Yin, H. H. Li, H. H. Li, L. Jiang, Y. Shi, Y. Sun, G. Lu, Q. Zhang,
X. Chen, and H. Zhang, “Single-layer MoS₂ phototransistors,” *ACS Nano*,
vol. 6, no. 1, pp. 74–80, 2012. (Cited in page 35).
- [145] N. Peimyoo, J. Shang, C. Cong, X. Shen, X. Wu, E. K. Yeow, and T. Yu,
“Nonblinking, intense two-dimensional light emitter: Monolayer WS₂ Tri-
angles,” *ACS Nano*, vol. 7, no. 12, pp. 10985–10994, 2013. (Cited in page
35).
- [146] B. Zhou, L. Yang, F. Chen, M. Xu, T. Wu, G. Wu, X. Chen, and D. Feng,
“Evolution of electronic structure in atomically thin sheets of WS₂ and
WSe₂,” *ACS Nano*, vol. 7, no. Xx, pp. 1, 791–797, 2013. (Cited in page
35).
- [147] A. Ennaoui, S. Fiechter, W. Jaegermann, and H. Tributsch, “Photoelectro-
chemistry of highly quantum efficient single-crystalline n-FeS₂ (Pyrite),”
J. Electrochem. Soc., vol. 133, no. 1, pp. 97–106, 1986. (Cited in page 35).
- [148] Z. Cheng, R. Cao, K. Wei, Y. Yao, X. Liu, J. Kang, J. Dong, Z. Shi,
H. Zhang, and X. Zhang, “2d materials enabled next-generation inte-
grated optoelectronics: from fabrication to applications,” *Advanced Sci-
ence*, vol. 8, no. 11, p. 2003834, 2021. (Cited in page 35).
- [149] K. S. Novoselov and A. H. Castro Neto, “Two-dimensional crystals-based
heterostructures: Materials with tailored properties,” *Phys. Scr.*, vol.
014006, no. T146, 2012. (Cited in pages 37, 38).
- [150] G. F. Schneider, V. E. Calado, H. Zandbergen, L. M. Vandersypen, and
C. Dekker, “Wedging transfer of nanostructures,” *Nano letters*, vol. 10,
no. 5, pp. 1912–1916, 2010. (Cited in pages 38, 39).
- [151] C. R. Dean, A. F. Young, I. Meric, C. Lee, L. Wang, S. Sorgenfrei,
K. Watanabe, T. Taniguchi, P. Kim, K. L. Shepard *et al.*, “Boron nitride

- substrates for high-quality graphene electronics,” *Nature nanotechnology*, vol. 5, no. 10, pp. 722–726, 2010. (Cited in pages 38, 39).
- [152] P. J. Zomer, S. P. Dash, N. Tombros, and B. J. Van Wees, “A transfer technique for high mobility graphene devices on commercially available hexagonal boron nitride,” *Applied Physics Letters*, vol. 99, no. 23, p. 232104, 2011. (Cited in pages 38, 39).
- [153] P. Blake, E. W. Hill, A. H. Castro Neto, K. S. Novoselov, D. Jiang, R. Yang, T. J. Booth, and A. K. Geim, “Making graphene visible,” *Appl. Phys. Lett.*, vol. 91, no. 6, 2007. (Cited in page 38).
- [154] S. Roddaro, P. Pingue, V. Piazza, V. Pellegrini, and F. Beltram, “The optical visibility of graphene: Interference colors of ultrathin graphite on SiO₂,” *Nano Lett.*, vol. 7, no. 9, pp. 2707–2710, 2007. (Cited in page 38).
- [155] A. Castellanos-Gomez, N. Agrat, and G. Rubio-Bollinger, “Optical identification of atomically thin dichalcogenide crystals,” *Appl. Phys. Lett.*, vol. 96, no. 21, pp. 94–97, 2010. (Cited in page 38).
- [156] Y. Y. Wang, R. X. Gao, Z. H. Ni, H. He, S. P. Guo, H. P. Yang, C. X. Cong, and T. Yu, “Thickness identification of two-dimensional materials by optical imaging,” *Nanotechnology*, vol. 23, no. 49, 2012. (Cited in page 38).
- [157] M. M. Benameur, B. Radisavljevic, J. S. Héron, S. Sahoo, H. Berger, and A. Kis, “Visibility of dichalcogenide nanolayers,” *Nanotechnology*, vol. 22, no. 12, 2011. (Cited in page 38).
- [158] H. Li, J. Wu, X. Huang, G. Lu, J. Yang, X. Lu, Q. Xiong, and H. Zhang, “Rapid and reliable thickness identification of two-dimensional nanosheets using optical microscopy,” *ACS Nano*, vol. 7, no. 11, pp. 10344–10353, 2013. (Cited in pages 38, 47).
- [159] Y. Lu, X. L. Li, X. Zhang, J. B. Wu, and P. H. Tan, “Optical contrast determination of the thickness of SiO₂ film on Si substrate partially covered by two-dimensional crystal flakes,” *Sci. Bull.*, vol. 60, no. 8, pp. 806–811, 2015. (Cited in page 38).
- [160] A. Castellanos-Gomez, M. Buscema, R. Molenaar, V. Singh, L. Janssen, H. S. Van Der Zant, and G. A. Steele, “Deterministic transfer of two-dimensional materials by all-dry viscoelastic stamping,” *2D Materials*, vol. 1, no. 1, p. 011002, 2014. (Cited in pages 39, 40).

- [161] M. A. Meitl, Z. T. Zhu, V. Kumar, K. J. Lee, X. Feng, Y. Y. Huang, I. Adesida, R. G. Nuzzo, and J. A. Rogers, “Transfer printing by kinetic control of adhesion to an elastomeric stamp,” *Nat. Mater.*, vol. 5, no. 1, pp. 33–38, 2006. (Cited in page 39).
- [162] A. V. Kretinin, Y. Cao, J. S. Tu, G. L. Yu, R. Jalil, K. S. Novoselov, S. J. Haigh, A. Gholinia, A. Mishchenko, M. Lozada, T. Georgiou, C. R. Woods, F. Withers, P. Blake, G. Eda, A. Wirsig, C. Hucho, K. Watanabe, T. Taniguchi, A. K. Geim, and R. V. Gorbachev, “Electronic properties of graphene encapsulated with different two-dimensional atomic crystals,” *Nano Lett.*, vol. 14, no. 6, pp. 3270–3276, 2014. (Cited in pages 43, 44).
- [163] S. J. Haigh, A. Gholinia, R. Jalil, S. Romani, L. Britnell, D. C. Elias, K. S. Novoselov, L. A. Ponomarenko, A. K. Geim, and R. Gorbachev, “Cross-sectional imaging of individual layers and buried interfaces of graphene-based heterostructures and superlattices,” *Nature materials*, vol. 11, no. 9, pp. 764–767, 2012. (Cited in pages 43, 44).
- [164] D. A. Sanchez, Z. Dai, and N. Lu, “2d material bubbles: Fabrication, characterization, and applications,” *Trends in Chemistry*, vol. 3, no. 3, pp. 204–217, 2021. (Cited in page 45).
- [165] E. Khestanova, F. Guinea, L. Fumagalli, A. Geim, and I. Grigorieva, “Universal shape and pressure inside bubbles appearing in van der waals heterostructures,” *Nature communications*, vol. 7, no. 1, p. 12587, 2016. (Cited in page 45).
- [166] S. J. Haigh, A. Gholinia, R. Jalil, S. Romani, L. Britnell, D. C. Elias, K. S. Novoselov, L. A. Ponomarenko, A. K. Geim, and R. Gorbachev, “Cross-sectional imaging of individual layers and buried interfaces of graphene-based heterostructures and superlattices,” *Nature materials*, vol. 11, no. 9, pp. 764–767, 2012. (Cited in page 45).
- [167] I. Gasparutti, S. H. Song, M. Neumann, X. Wei, K. Watanabe, T. Taniguchi, and Y. H. Lee, “How clean is clean? recipes for van der waals heterostructure cleanliness assessment,” *ACS applied materials & interfaces*, vol. 12, no. 6, pp. 7701–7709, 2020. (Cited in page 45).
- [168] K. Xu, P. Cao, and J. R. Heath, “Graphene visualizes the first water adlayers on mica at ambient conditions,” *Science*, vol. 329, no. 5996, pp. 1188–1191, 2010. (Cited in page 45).

- [169] A. V. Tyurnina, D. A. Bandurin, E. Khestanova, V. G. Kravets, M. Koperski, F. Guinea, A. N. Grigorenko, A. K. Geim, and I. V. Grigorieva, “Strained Bubbles in van der Waals Heterostructures as Local Emitters of Photoluminescence with Adjustable Wavelength,” *ACS Photonics*, vol. 6, no. 2, pp. 516–524, 2019. (Cited in page 45).
- [170] S. Goler, V. Piazza, S. Roddaro, V. Pellegrini, F. Beltram, and P. Pingue, “Self-assembly and electron-beam-induced direct etching of suspended graphene nanostructures,” *J. Appl. Phys.*, vol. 110, no. 6, 2011. (Cited in page 45).
- [171] A. Alruqi, “2D materials based heterostructures: a lithography free method.” 2019. (Cited in page 47).
- [172] M. Escher, N. Weber, M. Merkel, C. Zietzen, P. Bernhard, G. Schönhense, S. Schmidt, F. Forster, F. Reinert, B. Krömker, and D. Funnemann, “NanoESCA: A novel energy filter for imaging x-ray photoemission spectroscopy,” *J. Phys. Condens. Matter*, vol. 17, no. 16, 2005. (Cited in page 47).
- [173] C. Tusche, A. Krasnyuk, and J. Kirschner, “Spin resolved bandstructure imaging with a high resolution momentum microscope,” *Ultramicroscopy*, vol. 159, pp. 520–529, 2015. (Cited in pages 47, 80, 83).
- [174] J. Avila, I. Razado-Colambo, S. Lorcy, B. Lagarde, J. L. Giorgetta, F. Polack, and M. C. Asensio, “ANTARES, a scanning photoemission microscopy beamline at SOLEIL,” *J. Phys. Conf. Ser.*, vol. 425, no. PART 19, 2013. (Cited in pages 50, 51).
- [175] J. Avila and M. C. Asensio, “First NanoARPES user facility available at SOLEIL: An innovative and powerful tool for studying advanced materials,” *Synchrotron Radiat. News*, vol. 27, no. 2, pp. 24–30, 2014. (Cited in page 50).
- [176] J. Avila, I. Razado-Colambo, S. Lorcy, J.-L. Giorgetta, F. Polack, and M. C. Asensio, “Interferometer-controlled soft x-ray scanning photoemission microscope at soleil,” in *Journal of Physics: Conference Series*, vol. 425, no. 13. IOP Publishing, 2013, p. 132013. (Cited in page 52).
- [177] D. Attwood, *Soft X-rays and Extreme Ultraviolet Radiation: Principles and Applications*. Cambridge University Press, 2001. (Cited in page 53).

- [178] A. Bostwick, E. Rotenberg, J. Avila, and M. C. Asensio, “Zooming in on Electronic Structure: NanoARPES at SOLEIL and ALS,” *Synchrotron Radiat. News*, vol. 25, no. 5, pp. 19–25, 2012. (Cited in page 54).
- [179] A. L. D. Kilcoyne, T. Tyliczszak, W. F. Steele, S. Fakra, P. Hitchcock, K. D. Franck, E. H. Anderson, B. D. Harteneck, E. G. Rightor, G. E. Mitchell, A. P. Hitchcock, L. Yang, T. Warwick, and H. W. Ade, “Interferometer-controlled scanning transmission x-ray microscopes at the advanced light source.” *Journal of synchrotron radiation*, vol. 10 Pt 2, pp. 125–36, 2003. (Cited in page 54).
- [180] E. Rotenberg, *A Practical Guide to Photoemission*, 2018. (Cited in pages 54, 56).
- [181] S. Moser, D. Kilcoyne, J. D. Denlinger, R. J. Koch, C. Jozwiak, A. Bostwick, and E. Rotenberg, “Polarization control at the microscopic and electronic structure observatory,” *Nucl. Instruments Methods Phys. Res. Sect. A Accel. Spectrometers, Detect. Assoc. Equip.*, vol. 914, pp. 156–164, 2019. (Cited in page 54).
- [182] microARPES- MAESTRO, <https://sites.google.com/a/lbl.gov/maestro/instrumentation/microarpes>, accessed: 2022-05-01. [Online]. Available: <https://sites.google.com/a/lbl.gov/maestro/instrumentation/microarpes> (Cited in page 55).
- [183] E. Rotenberg, “The Art of Photoelectron Spectroscopy, from Micro to Nano,” in *APS March Meeting Abstracts*, ser. APS Meeting Abstracts, vol. 2017, 2017, p. F23.004. (Cited in page 55).
- [184] R. Koch, S. Moser, S. Ulstrup, L. Moreschini, C. Jozwiak, A. Bostwick, and E. Rotenberg, “The new nanoARPES at MAESTRO of the ALS,” in *APS March Meeting Abstracts*, ser. APS Meeting Abstracts, vol. 2017, 2017, p. L36.007. (Cited in page 55).
- [185] C. Kastl, R. Koch, C. Chen, B. Schuler, J. Eichhorn, S. Moser, S. Ulstrup, T. Kuykendall, A. Bostwick, C. Jozwiak, E. Rotenberg, A. Weber-Bargioni, S. Aloni, and A. Schwartzberg, “2D materials under the microscope(s),” in *APS March Meeting Abstracts*, ser. APS Meeting Abstracts, vol. 2018, 2018, p. R40.003. (Cited in page 55).
- [186] C. Kastl, C. T. Chen, R. J. Koch, B. Schuler, T. R. Kuykendall, A. Bostwick, C. Jozwiak, T. Seyller, E. Rotenberg, A. Weber-Bargioni, S. Aloni,

- and A. M. Schwartzberg, “Multimodal spectromicroscopy of monolayer WS_2 enabled by ultra-clean van der Waals epitaxy,” *2D Mater.*, vol. 5, no. 4, p. 045010, jul 2018. (Cited in page 55).
- [187] R. J. Koch, C. Jozwiak, A. Bostwick, B. Stripe, M. Cordier, Z. Hussain, W. Yun, and E. Rotenberg, “Nano focusing of soft x-rays by a new capillary mirror optic,” *Synchrotron Radiat. News*, vol. 31, no. 4, pp. 50–52, 2018. (Cited in pages 55, 56, 67).
- [188] Endstation Tables- MAESTRO, <https://sites.google.com/a/lbl.gov/maestro/instrumentation/endstation-tables>, accessed: 2021-10-12. [Online]. Available: <https://sites.google.com/a/lbl.gov/maestro/instrumentation/endstation-tables> (Cited in page 55).
- [189] Sigray, Inc., <https://sigray.com/x-ray-optics/>, accessed: 2023-26-03. [Online]. Available: <https://sigray.com/x-ray-optics/> (Cited in page 55).
- [190] C. Wiemann, M. Patt, I. Krug, N. B. Weber, M. Escher, M. Merkel, and C. M. Schneider, “A new nanospectroscopy tool with synchrotron radiation: Nanoesca@elettra,” *E-journal of Surface Science and Nanotechnology*, vol. 9, pp. 395–399, 2011. (Cited in page 57).
- [191] M. C. Patt, *Bulk and surface sensitive energy-filtered photoemission microscopy using synchrotron radiation for the study of resistive switching memories*, dissertation, Universität Duisburg-Essen, 2016. (Cited in pages 57, 58, 59).
- [192] H. Yuan, Z. Liu, G. Xu, B. Zhou, S. Wu, D. Dumcenco, K. Yan, Y. Zhang, S. K. Mo, P. Dudin, V. Kandyba, M. Yablonskikh, A. Barinov, Z. Shen, S. Zhang, Y. Huang, X. Xu, Z. Hussain, H. Y. Hwang, Y. Cui, and Y. Chen, “Evolution of the valley position in bulk transition-metal chalcogenides and their monolayer limit,” *Nano Lett.*, vol. 16, no. 8, pp. 4738–4745, 2016. (Cited in page 61).
- [193] W. Jin, P. C. Yeh, N. Zaki, D. Zhang, J. T. Sadowski, A. Al-Mahboob, A. M. Van Der Zande, D. A. Chenet, J. I. Dadap, I. P. Herman, P. Sutter, J. Hone, and R. M. Osgood, “Direct measurement of the thickness-dependent electronic band structure of MoS_2 using angle-resolved photoemission spectroscopy,” *Phys. Rev. Lett.*, vol. 111, no. 10, pp. 1–5, 2013. (Cited in page 61).
- [194] N. R. Wilson, P. V. Nguyen, K. Seyler, P. Rivera, A. J. Marsden, Z. P. Laker, G. C. Constantinescu, V. Kandyba, A. Barinov, N. D. Hine, X. Xu,

- and D. H. Cobden, “Determination of band offsets, hybridization, and exciton binding in 2D semiconductor heterostructures,” *Sci. Adv.*, vol. 3, no. 2, pp. 1–8, 2017. (Cited in pages 61, 113).
- [195] F. H. L. Koppens, T. Mueller, P. Avouris, A. C. Ferrari, M. S. Vitiello, and M. Polini, “Photodetectors based on graphene, other two-dimensional materials and hybrid systems,” *Nat. Nanotechnol.*, vol. 9, no. 10, pp. 780–793, 2014. (Cited in pages 61, 113).
- [196] G. R. Bhimanapati, Z. Lin, V. Meunier, Y. Jung, J. Cha, S. Das, D. Xiao, Y. Son, M. S. Strano, V. R. Cooper, L. Liang, S. G. Louie, E. Ringe, W. Zhou, S. S. Kim, R. R. Naik, B. G. Sumpter, H. Terrones, F. Xia, Y. Wang, J. Zhu, D. Akinwande, N. Alem, J. A. Schuller, R. E. Schaak, M. Terrones, and J. A. Robinson, “Recent Advances in Two-Dimensional Materials beyond Graphene,” *ACS Nano*, vol. 9, no. 12, pp. 11 509–11 539, 2015. (Cited in pages 61, 113).
- [197] E. Y. Andrei, D. K. Efetov, P. Jarillo-Herrero, A. H. MacDonald, K. F. Mak, T. Senthil, E. Tutuc, A. Yazdani, and A. F. Young, “The marvels of moiré materials,” *Nature Reviews Materials*, vol. 6, no. 3, pp. 201–206, 2021. (Cited in pages 61, 113).
- [198] L. Britnell, R. V. Gorbachev, R. Jalil, B. D. Belle, F. Schedin, A. Mishchenko, T. Georgiou, M. I. Katsnelson, L. Eaves, S. V. Morozov, N. M. R. Peres, J. Leist, A. K. Geim, K. S. Novoselov, and L. A. Ponomarenko, “Field-effect tunneling transistor based on vertical graphene heterostructures,” *Science*, vol. 335, no. 6071, pp. 947–950, 2012. (Cited in pages 62, 113).
- [199] Y. Liu, N. O. Weiss, X. Duan, H. C. Cheng, Y. Huang, and X. Duan, “Van der Waals heterostructures and devices,” *Nat. Rev. Mater.*, vol. 1, no. 9, 2016. (Cited in pages 62, 113).
- [200] M. H. Doan, Y. Jin, S. Adhikari, S. Lee, J. Zhao, S. C. Lim, and Y. H. Lee, “Charge Transport in MoS₂/WSe₂ van der Waals Heterostructure with Tunable Inversion Layer,” *ACS Nano*, vol. 11, no. 4, pp. 3832–3840, 2017. (Cited in pages 62, 113).
- [201] R. Frisenda, E. Navarro-Moratalla, P. Gant, D. Pérez De Lara, P. Jarillo-Herrero, R. V. Gorbachev, and A. Castellanos-Gomez, “Recent progress in the assembly of nanodevices and van der Waals heterostructures by

- deterministic placement of 2D materials,” *Chem. Soc. Rev.*, vol. 47, no. 1, pp. 53–68, 2018. (Cited in pages 62, 113).
- [202] N. Huo, J. Kang, Z. Wei, S. S. Li, J. Li, and S. H. Wei, “Novel and enhanced optoelectronic performances of multilayer MoS₂-WS₂ heterostructure transistors,” *Adv. Funct. Mater.*, vol. 24, no. 44, pp. 7025–7031, 2014. (Cited in pages 62, 113).
- [203] F. H. Koppens, T. Mueller, P. Avouris, A. C. Ferrari, M. S. Vitiello, and M. Polini, “Photodetectors based on graphene, other two-dimensional materials and hybrid systems,” *Nat. Nanotechnol.*, vol. 9, no. 10, pp. 780–793, 2014. (Cited in pages 62, 113).
- [204] S. Mashhadi, D. L. Duong, M. Burghard, and K. Kern, “Efficient photothermoelectric conversion in lateral topological insulator heterojunctions,” *Nano Lett.*, vol. 17, no. 1, pp. 214–219, 2017. (Cited in pages 62, 113).
- [205] T. Roy, M. Tosun, X. Cao, H. Fang, D. H. Lien, P. Zhao, Y. Z. Chen, Y. L. Chueh, J. Guo, and A. Javey, “Dual-gated MoS₂/WSe₂ van der Waals tunnel diodes and transistors,” *ACS Nano*, vol. 9, no. 2, pp. 2071–2079, 2015. (Cited in pages 62, 113).
- [206] M. Sup Choi, G. H. Lee, Y. J. Yu, D. Y. Lee, S. Hwan Lee, P. Kim, J. Hone, and W. J. Yoo, “Controlled charge trapping by molybdenum disulphide and graphene in ultrathin heterostructured memory devices,” *Nat. Commun.*, vol. 4, pp. 1624–1627, 2013. (Cited in pages 62, 113).
- [207] M. Zhao, Y. Ye, Y. Han, Y. Xia, H. Zhu, S. Wang, Y. Wang, D. A. Muller, and X. Zhang, “Large-scale chemical assembly of atomically thin transistors and circuits,” *Nat. Nanotechnol.*, vol. 11, no. 11, pp. 954–959, 2016.
- [208] H. Li, Y. Li, A. Aljarb, Y. Shi, and L. J. Li, “Epitaxial growth of two-dimensional layered transition-metal dichalcogenides: growth mechanism, controllability, and scalability,” *Chem. Rev.*, vol. 118, no. 13, pp. 6134–6150, 2018. (Cited in pages 62, 113).
- [209] C. Tan, X. Cao, X. J. Wu, Q. He, J. Yang, X. Zhang, J. Chen, W. Zhao, S. Han, G. H. Nam, M. Sindoro, and H. Zhang, “Recent advances in ultrathin two-dimensional nanomaterials,” *Chem. Rev.*, vol. 117, no. 9, pp. 6225–6331, 2017. (Cited in pages 62, 113).

- [210] S. Z. Butler, S. M. Hollen, L. Cao, Y. Cui, J. A. Gupta, H. R. Gutiérrez, T. F. Heinz, S. S. Hong, J. Huang, A. F. Ismach, E. Johnston-Halperin, M. Kuno, V. V. Plashnitsa, R. D. Robinson, R. S. Ruoff, S. Salahuddin, J. Shan, L. Shi, M. G. Spencer, M. Terrones, W. Windl, and J. E. Goldberger, “Progress, challenges, and opportunities in two-dimensional materials beyond graphene,” *ACS Nano*, vol. 7, no. 4, pp. 2898–2926, 2013. (Cited in pages 62, 113).
- [211] Y. C. Lin, R. K. Ghosh, R. Addou, N. Lu, S. M. Eichfeld, H. Zhu, M. Y. Li, X. Peng, M. J. Kim, L. J. Li, R. M. Wallace, S. Datta, and J. A. Robinson, “Atomically thin resonant tunnel diodes built from synthetic van der Waals heterostructures,” *Nat. Commun.*, vol. 6, pp. 1–6, 2015. (Cited in page 63).
- [212] H. Zeng, G. B. Liu, J. Dai, Y. Yan, B. Zhu, R. He, L. Xie, S. Xu, X. Chen, W. Yao, and X. Cui, “Optical signature of symmetry variations and spin-valley coupling in atomically thin tungsten dichalcogenides,” *Sci. Rep.*, vol. 3, pp. 2–6, 2013. (Cited in page 63).
- [213] S. Borghardt, J. Sonntag, J.-S. Tu, T. Taniguchi, K. Watanabe, B. Beschoten, C. Stampfer, and B. Ewa Kardynał, “Radially polarized light beams from spin-forbidden dark excitons and trions in monolayer WSe₂,” *Opt. Mater. Express*, vol. 10, no. 5, p. 1273, 2020. (Cited in page 63).
- [214] R. Zhang, V. Koutsos, and R. Cheung, “Elastic properties of suspended multilayer WSe₂,” *Appl. Phys. Lett.*, vol. 108, no. 4, 2016. (Cited in page 64).
- [215] M. R. Müller, A. Gumprich, E. Ecik, K. T. Kallis, F. Winkler, B. Kardynał, I. Petrov, U. Kunze, and J. Knoch, “Visibility of two-dimensional layered materials on various substrates,” *J. Appl. Phys.*, vol. 118, no. 14, 2015. (Cited in page 64).
- [216] Y. Zhang, M. M. Ugeda, C. Jin, S. F. Shi, A. J. Bradley, A. Martín-Recio, H. Ryu, J. Kim, S. Tang, Y. Kim, B. Zhou, C. Hwang, Y. Chen, F. Wang, M. F. Crommie, Z. Hussain, Z. X. Shen, and S. K. Mo, “Electronic Structure, Surface Doping, and Optical Response in Epitaxial WSe₂ Thin Films,” *Nano Lett.*, vol. 16, no. 4, pp. 2485–2491, 2016. (Cited in page 71).

- [217] P. V. Nguyen, N. C. Teutsch, N. P. Wilson, J. Kahn, X. Xia, A. J. Graham, V. Kandyba, A. Giampietri, A. Barinov, G. C. Constantinescu, N. Yeung, N. D. Hine, X. Xu, D. H. Cobden, and N. R. Wilson, “Visualizing electrostatic gating effects in two-dimensional heterostructures,” *Nature*, vol. 572, no. 7768, pp. 220–223, 2019. (Cited in page 71).
- [218] J. Braun, J. Minár, and H. Ebert, “Correlation, temperature and disorder: Recent developments in the one-step description of angle-resolved photoemission,” *Phys. Rep.*, vol. 740, pp. 1–34, 2018. (Cited in pages 72, 106).
- [219] S. Ulstrup, R. J. Koch, S. Singh, K. M. McCreary, B. T. Jonker, J. T. Robinson, C. Jozwiak, E. Rotenberg, A. Bostwick, J. Katoch, and J. A. Miwa, “Direct observation of minibands in a twisted graphene/WS₂ bilayer,” *Sci. Adv.*, vol. 6, no. 14, 2020. (Cited in pages 77, 81, 105).
- [220] S. Kundu, M. H. Naik, H. Krishnamurthy, and M. Jain, “Moiré induced topology and flat bands in twisted bilayer WSe₂: A first-principles study,” *Physical Review B*, vol. 105, no. 8, p. L081108, 2022. (Cited in pages 85, 89, 90, 91, 94).
- [221] H. Yuan, Z. Liu, G. Xu, B. Zhou, S. Wu, D. Dumcenco, K. Yan, Y. Zhang, S. K. Mo, P. Dudin, V. Kandyba, M. Yablonskikh, A. Barinov, Z. Shen, S. Zhang, Y. Huang, X. Xu, Z. Hussain, H. Y. Hwang, Y. Cui, and Y. Chen, “Evolution of the valley position in bulk transition-metal chalcogenides and their monolayer limit,” *Nano Lett.*, vol. 16, no. 8, pp. 4738–4745, 2016. (Cited in page 85).
- [222] J. He, K. Hummer, and C. Franchini, “Stacking effects on the electronic and optical properties of bilayer transition metal dichalcogenides MoS₂, MoSe₂, WS₂, and WSe₂,” *Physical Review B*, vol. 89, no. 7, p. 075409, 2014. (Cited in pages 85, 89).
- [223] H. Nakamura, A. Mohammed, P. Rosenzweig, K. Matsuda, K. Nowakowski, K. Küster, P. Wochner, S. Ibrahimkutty, U. Wedig, H. Hussain, J. Rawle, C. Nicklin, B. Stuhlhofer, G. Cristiani, G. Logvenov, H. Takagi, and U. Starke, “Spin splitting and strain in epitaxial monolayer WSe₂ on graphene,” *Phys. Rev. B*, vol. 101, no. 16, apr 2020. (Cited in page 86).
- [224] H. Coy Diaz, J. Avila, C. Chen, R. Addou, M. C. Asensio, and M. Batzill, “Direct observation of interlayer hybridization and dirac relativistic carri-

- ers in Graphene/MoS₂ van der waals heterostructures,” *Nano Lett.*, vol. 15, no. 2, pp. 1135–1140, feb 2015. (Cited in page 88).
- [225] D. Pierucci, H. Henck, J. Avila, A. Balan, C. H. Naylor, G. Patriarche, Y. J. Dappe, M. G. Silly, F. Sirotti, A. T. Johnson, M. C. Asensio, and A. Ouerghi, “Band alignment and minigaps in monolayer MoS₂-graphene van der Waals heterostructures,” *Nano Lett.*, vol. 16, no. 7, pp. 4054–4061, 2016. (Cited in page 88).
- [226] I. Gierz, J. Henk, H. Höchst, C. R. Ast, and K. Kern, “Illuminating the dark corridor in graphene: Polarization dependence of angle-resolved photoemission spectroscopy on graphene,” *Physical Review B*, vol. 83, no. 12, p. 121408, 2011. (Cited in page 88).
- [227] H. Henck, J. Avila, Z. Ben Aziza, D. Pierucci, J. Baima, B. Pamuk, J. Chaste, D. Utt, M. Bartos, K. Nogajewski, B. A. Piot, M. Orlita, M. Potemski, M. Calandra, M. C. Asensio, F. Mauri, C. Faugeras, and A. Ouerghi, “Flat electronic bands in long sequences of rhombohedral-stacked graphene,” *Phys. Rev. B*, vol. 97, p. 245421, Jun 2018. (Cited in page 88).
- [228] C. Coletti, S. Forti, A. Principi, K. V. Emtsev, A. A. Zakharov, K. M. Daniels, B. K. Daas, M. V. Chandrashekar, T. Ouisse, D. Chaussende, A. H. MacDonald, M. Polini, and U. Starke, “Revealing the electronic band structure of trilayer graphene on SiC: An angle-resolved photoemission study,” *Phys. Rev. B - Condens. Matter Mater. Phys.*, vol. 88, no. 15, p. 155439, 2013. (Cited in page 88).
- [229] M. Gmitra, D. Kochan, P. Högl, and J. Fabian, “Trivial and inverted Dirac bands and the emergence of quantum spin Hall states in graphene on transition-metal dichalcogenides,” *Phys. Rev. B*, vol. 93, no. 15, pp. 1–10, 2016. (Cited in page 89).
- [230] “We note that the nomenclature used to date might be confusing, because when think of the in-plane polarity of each layer, the 2H stacking is considered AB and 3R stacking is considered AA.” (Cited in page 91).
- [231] R. Bistritzer and A. H. MacDonald, “Moiré bands in twisted double-layer graphene,” *Proceedings of the National Academy of Sciences*, vol. 108, no. 30, pp. 12 233–12 237, 2011. (Cited in page 93).

- [232] S. Xie, B. D. Faeth, Y. Tang, L. Li, E. Gerber, C. T. Parzyck, D. Chowdhury, Y.-H. Zhang, C. Jozwiak, A. Bostwick *et al.*, “Strong interlayer interactions in bilayer and trilayer moiré superlattices,” *Science advances*, vol. 8, no. 12, p. eabk1911, 2022. (Cited in page 94).
- [233] Y. Zhang, J. R. Rouxel, J. Autschbach, N. Govind, and S. Mukamel, “X-ray circular dichroism signals: A unique probe of local molecular chirality,” *Chem. Sci.*, vol. 8, no. 9, pp. 5969–5978, 2017. (Cited in page 97).
- [234] L. Baumgarten, C. Schneider, H. Petersen, F. Schäfers, and J. Kirschner, “Magnetic x-ray dichroism in core-level photoemission from ferromagnets,” *Physical review letters*, vol. 65, no. 4, p. 492, 1990. (Cited in pages 97, 98).
- [235] B. Thole, P. Carra, F. Sette, and G. van der Laan, “X-ray circular dichroism as a probe of orbital magnetization,” *Physical review letters*, vol. 68, no. 12, p. 1943, 1992. (Cited in page 98).
- [236] W. Kuch, R. Schäfer, P. Fischer, and F. U. Hillebrecht, *Magnetic microscopy of layered structures*. Springer, 2015, vol. 57. (Cited in page 98).
- [237] P. S. Bechthold, *X-ray absorption spectroscopy. in: Probing the Nanoworld*. Chapter E9, Forschungszentrum Jülich GmbH, 38th IFF Spring School, 2007. (Cited in page 98).
- [238] H. Ebert, L. Baumgarten, C. Schneider, and J. Kirschner, “Polarization dependence of the 2p-core-level photoemission spectra of Fe,” *Physical Review B*, vol. 44, no. 9, p. 4406, 1991. (Cited in page 98).
- [239] H. Ebert, P. Strange, and B. L. Gyorffy, “Theory of circularly polarized x-ray absorption by ferromagnetic Fe,” *Journal of applied physics*, vol. 63, no. 8, pp. 3055–3057, 1988. (Cited in page 98).
- [240] G. Schönhense and G. Schönhense, “Circular Dichroism and Spin Polarization in Photoemission from Adsorbates and Non-Magnetic Solids,” *Phys. Scr.*, vol. 1990, no. T31, pp. 255–275, 1990. (Cited in pages 98, 99).
- [241] C.-H. Min, H. Bentmann, J. N. Neu, P. Eck, S. Moser, T. Figgemeier, M. Ünzelmann, K. Kissner, P. Lutz, R. J. Koch *et al.*, “Orbital fingerprint of topological fermi arcs in the weyl semimetal tap,” *Physical Review Letters*, vol. 122, no. 11, p. 116402, 2019. (Cited in page 98).

- [242] B. Kim, C. H. Kim, P. Kim, W. Jung, Y. Kim, Y. Koh, M. Arita, K. Shimada, H. Namatame, M. Taniguchi, J. Yu, and C. Kim, "Spin and orbital angular momentum structure of Cu(111) and Au(111) surface states," *Phys. Rev. B - Condens. Matter Mater. Phys.*, vol. 85, no. 19, pp. 1–6, 2012. (Cited in page 98).
- [243] S. R. Park, J. Han, C. Kim, Y. Y. Koh, C. Kim, H. Lee, H. J. Choi, J. H. Han, K. D. Lee, N. J. Hur, M. Arita, K. Shimada, H. Namatame, and M. Taniguchi, "Chiral orbital-angular momentum in the surface states of Bi₂Se₃," *Phys. Rev. Lett.*, vol. 108, no. 4, pp. 1–5, 2012. (Cited in page 98).
- [244] M. Schüler, U. de Giovannini, H. Hübener, A. Rubio, M. A. Sentef, and P. Werner, "Local Berry curvature signatures in dichroic angle-resolved photoelectron spectroscopy from two-dimensional materials," *Sci. Adv.*, vol. 6, no. 9, 2020. (Cited in page 98).
- [245] H. Ryu, I. Song, B. Kim, S. Cho, S. Soltani, T. Kim, M. Hoesch, C. H. Kim, and C. Kim, "Photon energy dependent circular dichroism in angle-resolved photoemission from Au(111) surface states," *Phys. Rev. B*, vol. 95, no. 11, pp. 1–6, 2017. (Cited in page 99).
- [246] S. R. Park, C. H. Kim, J. Yu, J. H. Han, and C. Kim, "Orbital-angular-momentum based origin of rashba-type surface band splitting," *Phys. Rev. Lett.*, vol. 107, no. 15, pp. 1–5, 2011. (Cited in page 99).
- [247] J. H. Park, C. H. Kim, H. W. Lee, and J. H. Han, "Orbital chirality and Rashba interaction in magnetic bands," *Phys. Rev. B - Condens. Matter Mater. Phys.*, vol. 87, no. 4, pp. 1–4, 2013. (Cited in page 99).
- [248] D. Go, J.-P. Hanke, P. M. Buhl, F. Freimuth, G. Bihlmayer, H.-W. Lee, Y. Mokrousov, and S. Blügel, "Toward surface orbitronics: giant orbital magnetism from the orbital rashba effect at the surface of sp-metals," *Scientific reports*, vol. 7, no. 1, pp. 1–10, 2017. (Cited in page 99).
- [249] V. Sunko, H. Rosner, P. Kushwaha, S. Khim, F. Mazzola, L. Bawden, O. J. Clark, J. M. Riley, D. Kasinathan, M. W. Haverkort, T. K. Kim, M. Hoesch, J. Fujii, I. Vobornik, A. P. Mackenzie, and P. D. King, "Maximal Rashba-like spin splitting via kinetic-energy-coupled inversion-symmetry breaking," *Nature*, vol. 549, no. 7673, pp. 492–496, 2017. (Cited in page 99).

- [250] D. Xiao, G.-B. Liu, W. Feng, X. Xu, and W. Yao, "Coupled spin and valley physics in monolayers of MoS₂ and other group-VI dichalcogenides," *Phys. Rev. Lett.*, vol. 108, no. 19, p. 196802, 2012. (Cited in page 99).
- [251] E. Cappelluti, R. Roldán, J. A. Silva-Guillén, P. Ordejón, and F. Guinea, "Tight-binding model and direct-gap/indirect-gap transition in single-layer and multilayer MoS₂," *Phys. Rev. B - Condens. Matter Mater. Phys.*, vol. 88, no. 7, pp. 1–18, 2013. (Cited in pages 99, 103).
- [252] G. B. Liu, W. Y. Shan, Y. Yao, W. Yao, and D. Xiao, "Three-band tight-binding model for monolayers of group-VIB transition metal dichalcogenides," *Phys. Rev. B - Condens. Matter Mater. Phys.*, vol. 88, no. 8, pp. 1–10, 2013. (Cited in page 99).
- [253] Y. Xu, C. Liu, D. Khim, and Y. Y. Noh, "Development of high-performance printed organic field-effect transistors and integrated circuits," *Phys. Chem. Chem. Phys.*, vol. 17, no. 40, pp. 26 553–26 574, 2014. (Cited in page 99).
- [254] T. Cao, G. Wang, W. Han, H. Ye, C. Zhu, J. Shi, Q. Niu, P. Tan, E. Wang, B. Liu, and J. Feng, "Valley-selective circular dichroism of monolayer molybdenum disulphide," *Nat. Commun.*, vol. 3, no. May, 2012. (Cited in page 99).
- [255] W. Yao, D. Xiao, and Q. Niu, "Valley-dependent optoelectronics from inversion symmetry breaking," *Physical Review B*, vol. 77, no. 23, p. 235406, 2008. (Cited in page 99).
- [256] D. Xiao, W. Yao, and Q. Niu, "Valley-contrasting physics in graphene: magnetic moment and topological transport," *Physical review letters*, vol. 99, no. 23, p. 236809, 2007. (Cited in page 99).
- [257] D. Xiao, M.-C. Chang, and Q. Niu, "Berry phase effects on electronic properties," *Reviews of modern physics*, vol. 82, no. 3, p. 1959, 2010. (Cited in page 99).
- [258] Z. Gong, G.-B. Liu, H. Yu, D. Xiao, X. Cui, X. Xu, and W. Yao, "Magnetoelectric effects and valley-controlled spin quantum gates in transition metal dichalcogenide bilayers," *Nature communications*, vol. 4, no. 1, pp. 1–6, 2013. (Cited in page 99).
- [259] W. Feng, Y. Yao, W. Zhu, J. Zhou, W. Yao, and D. Xiao, "Intrinsic spin Hall effect in monolayers of group-VI dichalcogenides: A first-principles

- study,” *Phys. Rev. B - Condens. Matter Mater. Phys.*, vol. 86, no. 16, pp. 1–6, 2012. (Cited in page 99).
- [260] T. Olsen and I. Souza, “Valley Hall effect in disordered monolayer MoS₂ from first principles,” *Phys. Rev. B - Condens. Matter Mater. Phys.*, vol. 92, no. 12, pp. 1–12, 2015. (Cited in page 99).
- [261] J. Minar, “13 theoretical description of arpes: The one-step model,” *DMFT at 25: Infinite Dimensions*, 2014. (Cited in page 99).
- [262] I. Gierz, M. Lindroos, H. Höchst, C. R. Ast, and K. Kern, “Graphene sublattice symmetry and isospin determined by circular dichroism in angle-resolved photoemission spectroscopy,” *Nano Lett.*, vol. 12, no. 8, pp. 3900–3904, 2012. (Cited in page 99).
- [263] P. Krüger and F. Matsui, “Observation and theory of strong circular dichroism in angle-revolved photoemission from graphite,” *Journal of Electron Spectroscopy and Related Phenomena*, vol. 258, p. 147219, 2022. (Cited in page 99).
- [264] M. R. Scholz, J. Sánchez-Barriga, J. Braun, D. Marchenko, A. Varykhalov, M. Lindroos, Y. J. Wang, H. Lin, A. Bansil, J. Minár, H. Ebert, A. Volykhov, L. V. Yashina, and O. Rader, “Reversal of the circular dichroism in angle-resolved photoemission from Bi₂Te₃,” *Phys. Rev. Lett.*, vol. 110, no. 21, pp. 1–5, 2013. (Cited in page 99).
- [265] R. P. Walker, B. Diviacco, L. Tosi, R. Roux, D. Zangrando, and F. Iazzourene, “Commissioning of elliptical undulators in elettra,” 2000. (Cited in page 99).
- [266] B. Diviacco, R. Bracco, D. Millo, R. Walker, M. Zalateu, and D. Zangrando, “Development of elliptical undulators for elettra,” in *Proceedings of the 1999 Particle Accelerator Conference (Cat. No.99CH36366)*, vol. 4, 1999, pp. 2680–2682 vol.4. (Cited in page 99).
- [267] W. Kuch and C. M. Schneider, “Magnetic dichroism in valence band photoemission,” *Reports Prog. Phys.*, vol. 64, no. 2, pp. 147–204, 2001. (Cited in page 101).
- [268] C. M. Schneider, M. S. Hammond, P. Schuster, A. Cebollada, R. Miranda, and J. Kirschner, “Observation of magnetic circular dichroism in UV photoemission from ferromagnetic fcc cobalt films,” *Phys. Rev. B*, vol. 44, no. 21, pp. 12066–12069, 1991. (Cited in page 101).

- [269] D. Venus, “Magnetic dichroism in uv photoemission from valence bands: Geometries where the three-step model of photoemission predicts null results,” *Physical Review B*, vol. 56, no. 5, p. 2661, 1997. (Cited in page 101).
- [270] C. Roth, F. U. Hillebrecht, H. Rose, and E. Kisker, “Linear magnetic dichroism in angular resolved Fe 3p core level photoemission,” *Phys. Rev. Lett.*, vol. 70, no. 22, pp. 3479–3482, 1993. (Cited in page 101).
- [271] M. Schüler, U. de Giovannini, H. Hübener, A. Rubio, M. A. Sentef, and P. Werner, “Local Berry curvature signatures in dichroic angle-resolved photoelectron spectroscopy from two-dimensional materials,” *Sci. Adv.*, vol. 6, no. 9, 2020. (Cited in pages 101, 104, 112, 115).
- [272] Z. Gong, G. B. Liu, H. Yu, D. Xiao, X. Cui, X. Xu, and W. Yao, “Magnetoelectric effects and valley-controlled spin quantum gates in transition metal dichalcogenide bilayers,” *Nat. Commun.*, vol. 4, no. May, pp. 1–6, 2013. (Cited in page 103).
- [273] H. Zeng, J. Dai, W. Yao, D. Xiao, and X. Cui, “Valley polarization in MoS₂ monolayers by optical pumping,” *Nat. Nanotechnol.*, vol. 7, no. 8, pp. 490–493, 2012. (Cited in page 103).
- [274] H. Zeng, G.-B. Liu, J. Dai, Y. Yan, B. Zhu, R. He, L. Xie, S. Xu, X. Chen, W. Yao *et al.*, “Optical signature of symmetry variations and spin-valley coupling in atomically thin tungsten dichalcogenides,” *Scientific reports*, vol. 3, no. 1, pp. 1–5, 2013. (Cited in page 103).
- [275] X. Zhang, Q. Liu, J.-W. Luo, A. J. Freeman, and A. Zunger, “Hidden spin polarization in inversion-symmetric bulk crystals,” *Nature Physics*, vol. 10, no. 5, pp. 387–393, 2014. (Cited in page 103).
- [276] S. Oh and H. J. Choi, “Orbital angular momentum analysis for giant spin splitting in solids and nanostructures,” *Scientific reports*, vol. 7, no. 1, 2017. (Cited in page 103).
- [277] M. Schüler, T. Pincelli, S. Dong, T. P. Devereaux, M. Wolf, L. Rettig, R. Ernstorfer, and S. Beaulieu, “Polarization-modulated angle-resolved photoemission spectroscopy: Towards circular dichroism without circular photons and Bloch wavefunction reconstruction,” *Phys. Rev. X*, vol. 12, no. 1, p. 11019, 2021. (Cited in page 104).

- [278] M. Schüler and S. Beaulieu, “Probing topological floquet states in WSe₂ using circular dichroism in time- and angle-resolved photoemission spectroscopy,” *arXiv:2201.10476*, 2022. (Cited in page 104).
- [279] S. Cho, J. H. Park, J. Hong, J. Jung, B. S. Kim, G. Han, W. Kyung, Y. Kim, S. K. Mo, J. D. Denlinger, J. H. Shim, J. H. Han, C. Kim, and S. R. Park, “Experimental Observation of Hidden Berry Curvature in Inversion-Symmetric Bulk 2H-WSe₂,” *Phys. Rev. Lett.*, vol. 121, no. 18, pp. 1–6, 2018. (Cited in pages 104, 112, 115).
- [280] S. Cho, J.-H. Park, S. Huh, J. Hong, W. Kyung, B.-G. Park, J. D. Denlinger, J. H. Shim, C. Kim, and S. R. Park, “Studying local Berry curvature in 2H-WSe₂ by circular dichroism photoemission utilizing crystal mirror plane,” *Scientific reports*, vol. 11, no. 1, pp. 1–9, 2021. (Cited in pages 104, 112, 115).
- [281] H. Rostami, K. Volckaert, N. Lanata, S. K. Mahatha, C. E. Sanders, M. Bianchi, D. Lizzit, L. Bignardi, S. Lizzit, J. A. Miwa, A. V. Balatsky, P. Hofmann, and S. Ulstrup, “Layer and orbital interference effects in photoemission from transition metal dichalcogenides,” *Phys. Rev. B*, vol. 100, no. 23, p. 235423, 2019. (Cited in page 105).
- [282] H. Ebert, D. Ködderitzsch, and J. Minár, “Calculating condensed matter properties using the KKR-Green’s function method - Recent developments and applications,” *Reports Prog. Phys.*, vol. 74, no. 9, 2011. (Cited in page 106).
- [283] H. Henck, Z. Ben Aziza, D. Pierucci, F. Laourine, F. Reale, P. Palczynski, J. Chaste, M. G. Silly, F. Bertran, P. Le Fèvre, E. Lhuillier, T. Wakamura, C. Mattevi, J. E. Rault, M. Calandra, and A. Ouerghi, “Electronic band structure of Two-Dimensional WS₂/Graphene van der Waals Heterostructures,” *Phys. Rev. B*, vol. 97, no. 15, pp. 1–8, 2018. (Cited in page 106).
- [284] J. P. Carbone, D. Go, Y. Mokrousov, G. Bihlmayer, and S. Blügel, “Engineering spin-orbit effects and berry curvature by deposition of a monolayer of eu on wse 2,” *Physical Review B*, vol. 106, no. 6, p. 064401, 2022. (Cited in page 111).
- [285] S. Oh and H. J. Choi, “Orbital angular momentum analysis for giant spin splitting in solids and nanostructures,” *Scientific reports*, vol. 7, no. 1, p. 2024, 2017. (Cited in page 111).

-
- [286] S. Bhowal and S. Satpathy, “Intrinsic orbital moment and prediction of a large orbital hall effect in two-dimensional transition metal dichalcogenides,” *Physical Review B*, vol. 101, no. 12, p. 121112, 2020. (Cited in page 111).
- [287] P. E. F. Junior, K. Zollner, T. Woźniak, M. Kurpas, M. Gmitra, and J. Fabian, “First-principles insights into the spin-valley physics of strained transition metal dichalcogenides monolayers,” *New Journal of Physics*, vol. 24, no. 8, p. 083004, 2022. (Cited in page 111).
- [288] O. J. Clark, O. Dowinton, M. S. Bahramy, and J. Sánchez-Barriga, “Hidden spin-orbital texture at the γ -located valence band maximum of a transition metal dichalcogenide semiconductor,” *Nature Communications*, vol. 13, no. 1, p. 4147, 2022. (Cited in page 111).
- [289] T. P. Cysne, M. Costa, L. M. Canonico, M. B. Nardelli, R. Muniz, and T. G. Rappoport, “Disentangling orbital and valley hall effects in bilayers of transition metal dichalcogenides,” *Physical review letters*, vol. 126, no. 5, p. 056601, 2021. (Cited in page 111).
- [290] F. Wu, T. Lovorn, E. Tutuc, I. Martin, and A. MacDonald, “Topological insulators in twisted transition metal dichalcogenide homobilayers,” *Physical review letters*, vol. 122, no. 8, p. 086402, 2019. (Cited in page 115).

Publications and conference contributions

Articles

A1 “Photoemission study of twisted monolayers and bilayers of WSe₂ on graphite substrates”

B. Parashar, L. Rathmann, H.J. Kim, I. Cojocariu, A. Bostwick, C. Jozwiak, E. Rotenberg, J. Avila, P. Dudin, V. Feyer, C. Stampfer, B. Beschoten, G. Bihlmayer, C.M. Schneider, and L. Plucinski
Phys. Rev. Materials, **7(4)**, 044004(2023)

A2 “Twist angle dependent interlayer transfer of valley polarization from excitons to free charge carriers in WSe₂/MoSe₂ heterobilayers”

F. Volmer, M. Ersfeld, P.E.F. Junior, L. Waldecker, **B. Parashar**, L. Rathmann, S. Dubey, I. Cojocariu, V. Feyer, K. Watanabe, T. Taniguchi, C.M. Schneider, L. Plucinski, C. Stampfer, J. Fabian, B. Beschoten
npj 2D Materials and Applications, **7(1)**, 58(2023)

Conference contributions (related to this work)

Talk “Photoemission study of twisted monolayers and bilayers of WSe₂ on graphite substrates”

B. Parashar, L. Rathmann, H.J. Kim, I. Cojocariu, A. Bostwick, C. Jozwiak, E. Rotenberg, J. Avila, P. Dudin, V. Feyer, C. Stampfer, B. Beschoten, G. Bihlmayer, C.M. Schneider, and L. Plucinski
ICES-15, Oulu, Finland (2023)

Poster “Investigation of two-dimensional materials via photoemission and microscopy”

B. Parashar, S. Borghardt, M. Jugovac, V. Feyer, B. Kardynal, L. Plucinski, and C.M. Schneider
Science Days JARA-FIT, Schleiden, Germany (2019)

Poster “Photoemission electron microscopy study of MXene microflakes”

B. Parashar, P.Gospodarič, K. Hantanasirisakul, S. Nemsak, T. Duchon,

J. Hackl, L. Plucinski, S. May, Y. Gogotsi, and C.M. Schneider
DPG Spring Meeting, Berlin, Germany (2018)

Curriculum vitae

Personal Data

Name	Bharti Parashar
Address	Eichendorffstrasse 6, 97218 Gerbrunn
Date of birth	16 th March 1993
Place of birth	Delhi, India
Nationality	Indian

Professional Experience

06/2022 - Present	Postdoc researcher at Würzburg University (TEP)
10/2017 - 03/2021	Ph.D. researcher at Forschungszentrum Jülich (PGI-6)
01/2017 - 07/2017	Student Assistant at Laboratory of Biophysics and Pharmacology, UMR 7213 CNRS– Strasbourg University
01/2016 - 06/2016	Student Assistant at National Physical Laboratory (NPL), CSIR-New Delhi, India

Education

Ph.D. in Physics (2017 - 2022)	Duisburg-Essen University (DE)
M.Sc. in Nanoscience+ M.tech in Nanotechnology (2011 - 2014)	Amity University (IN)
B.Sc. in Physics (2011-2014)	Delhi University (IN)

Acknowledgments

I am deeply honoured to express my most profound appreciation to all the people who contributed to the successful completion of this thesis.

First and foremost, I extend my sincere gratitude to my supervisor, Prof. Dr. Claus M. Schneider, for allowing me to be a part of PGI-6, his invaluable guidance and support throughout my research journey. I have inculcated imperative skills as a researcher while working with him, allowing me to build strong collaborations and perform high-impact research.

I would also like to express my heartfelt thanks to Dr. Lukasz Plucinski for his unwavering support, constant encouragement, and insightful ideas, which were instrumental in shaping my research work. His ability to ask striking and exciting questions and his willingness to lend a helping hand during critical moments were truly invaluable.

Working at different beamlines at various synchrotron facilities worldwide was integral to my thesis. I would therefore like to extend my sincere thanks to the team, especially to Dr. Vitaliy Feyer, Dr. Jose Avila, Dr. Pavel Dudin, Dr. Aaron Bostwick, Dr. Eli Rotenberg, and Dr. Chris Jozwiak for their support, valuable inputs, and discussions to successfully achieve expected results at Elettra, ALS, and Soleil.

A token of appreciation to the technical group, including Heinz Pfeiffer, Norbert Schnitzler, Arnd Bremen, and Bernd Küpper, for their expertise and technical support throughout my Ph.D. in FZ Jülich. They were behind-the-scenes champions who contributed immensely during my experimental work to generate successful outcomes.

I am also grateful to Dr. Gustav Bihlmayer, Dr. Hyun-Jung Kim, and Dr. Bernd Beschoten for their insightful contributions to the theoretical calculations and support in preparing my samples.

Last, I would like to thank all present and former members of PGI-6, including Dr. Umut Parlak, Dr. Matteo Jugovac, Dr. Anna Hutzen, Sarah Heitfeld, Christian Greb, Tristan Heider, Fangzhou Wang, and Xin Liang

Tan. Our time together has been more than just colleagues but also friends. In particular, I built a stronger connection with Sarah while sharing an office space that I would gladly cherish for life. Engaging in scientific, social and fun-loving discussions with Christian, Fangzhou, and Tristan were indeed a stress buster and significantly eased my PhD journey. I would also like to thank Dr. Pika Gospodaric for her willingness to help nature despite spending a brief time together.

My achievements wouldn't have been possible without the love and support of my amazing parents, Ms. Shakuntala Parashar and Mr. Suresh Parashar, and my lovely siblings, Rajni and Kapil. They have been my pillars of strength and have always been there for me. Their invaluable guidance is in the rhythm not just during this journey but in every aspect of my life.

I want to give a special mention to Dr. Aviraj Ingle, Dr. Paula Medeiros do Valle, and Ms. Gurpreet Sethi for their unyielding encouragement, support, and affection throughout this experience when I needed the most.

Band / Volume 263

**9th Georgian-German School and Workshop in Basic Science
September 12 – 16, 2022 | Kutaisi, Tbilisi | Georgia**

A. Kacharava, E. Portius, N. J. Shah, H. Ströher (2022)

ISBN: 978-3-95806-664-9

Band / Volume 264

Self-assembly of Au-Fe₃O₄ dumbbell nanoparticles

N. Nandakumaran (2022), xiv, 234 pp

ISBN: 978-3-95806-666-3

Band / Volume 265

**Time-resolved and three-dimensional characterisation of magnetic states
in nanoscale materials in the transmission electron microscope**

T. Weßels (2023), xx, 211 pp

ISBN: 978-3-95806-685-4

Band / Volume 266

**Dissecting iron and heme regulatory networks and adaptation
to heme stress in *Corynebacterium glutamicum***

A. Krüger (2023), IV, 274 pp

ISBN: 978-3-95806-686-1

Band / Volume 267

**Morphological and functional characterization of layer 5 neurons in rat
medial prefrontal cortex, their synaptic microcircuitry and serotonin
modulation**

R. Rama (2023), 116 pp

ISBN: 978-3-95806-688-5

Band / Volume 268

**Magnetic and transport studies of the parent and
Fe doped Hexagonal-Mn₃Ge Weyl semimetal**

V. Rai (2023), xviii, 156 pp

ISBN: 978-3-95806-695-3

Band / Volume 269

**The complex inositol metabolism of *Corynebacterium glutamicum* and its
application for the production of rare inositols**

P. Ramp (2023), VI, 161 pp

ISBN: 978-3-95806-699-1

Band / Volume 270

**Spin- and orbital-dependent band structure of
unconventional topological semimetals**

K. Hagiwara (2023), v, 115 pp

ISBN: 978-3-95806-701-1

Band / Volume 271

Neutron scattering

Experimental Manuals of the JCNS Laboratory Course held at
Forschungszentrum Jülich and at the Heinz-Maier-Leibnitz Zentrum Garching
edited by T. Brückel, S. Förster, K. Friese, M. Kruteva, M. Zobel and R. Zorn
(2023), ca 150 pp
ISBN: 978-3-95806-705-9

Band / Volume 272

**Ab-initio investigation of the interplay between the hyperfine
interaction and complex magnetism at the nanoscale**

S. R. S. Shehada (2023), ix, xi, 119 pp
ISBN: 978-3-95806-718-9

Band / Volume 273

**Analysis of the signal transduction cascade tuning the 2-oxoglutarate
dehydrogenase activity in *Corynebacterium glutamicum***

L. Sundermeyer (2023), VI, 119 pp
ISBN: 978-3-95806-722-6

Band / Volume 274

**Multicellular defense against phage infection in *Streptomyces* – impact of
secondary metabolites and mycelial development**

L. Kever (2023), iv, 246 pp
ISBN: 978-3-95806-724-0

Band / Volume 275

**Investigation of the electronic band structure of 2D transition metal
dichalcogenides via angle-resolved photoemission spectroscopy**

B. Parashar (2023), xvii, 156 pp
ISBN: 978-3-95806-725-7

Weitere **Schriften des Verlags im Forschungszentrum Jülich** unter
<http://www.zb1.fz-juelich.de/verlagextern1/index.asp>

Schlüsseltechnologien / Key Technologies

Band / Volume 275

ISBN 978-3-95806-725-7